REAL-TIME MONITORING BY USING KALMAN FILTER IN THE OCEAN

A Dissertation

by

HANSUNG KIM

Submitted to the Office of Graduate and Professional Studies of
Texas A&M University
in partial fulfillment of the requirements for the degree of

DOCTOR OF PHILOSOPHY

Chair of Committee,	Moo-Hyun Kim
Co-Chair of Committee,	Sharath Girimaji
Committee Members,	Robert Randall
	Raktim Bhattacharya
Head of Department,	Sharath Girimaji

May 2020

Major Subject: Ocean Engineering

ABSTRACT

The Digital Twin (DT) is cited as one of the key concepts associated with Industry 4.0 waves. DT is defined as a virtual copy-model or concept that is represented on a computer as the same with a physical thing. By building a virtual digital twin on software instead of actual physical assets and simulating them, we can get accurate information about the characteristics of the real assets, such as their current state and behavior. The DT is mainly used for monitoring, diagnostics and prediction to enhance asset performance and utilization. It aims to provide an amply integrated solution for structural health monitoring to increase the reliability of real assets. In this regard, the monitoring technology is an important part of the DT. In this study, the real-time monitoring algorithm, which estimates ocean wave directional spectrum and subsea riser's deformed shape, has been developed based on the Kalman filter.

The first application is to estimate ocean wave form vessel motion. The real-time inverse estimation of the ocean wave spectrum and elevation from a vessel-motion sensor is of significant practical importance, but it is still in the developing stage. The Kalman-filter method has the advantages of real-time estimation, cost reduction, and easy installation than other methods. Reasonable estimation of high-frequency waves is important in view of covering various sea states. However, if the vessel is less responsive for high-frequency waves, amplified noise may occur and cause overestimation problem there. In this paper, a configuration of Kalman filter with applying the principle of Wiener filter is proposed to suppress those over-estimations.

Over-estimation is significantly reduced at high frequencies when the method is applied, and reliable real-time wave spectra and elevations can be obtained. The simulated sensor data was used, but the proposed algorithm has been proved to perform well for various sea states and different vessels. In addition, the proposed Kalman-filter technique is robust when it is applied to time-varying sea states. Finally, the proposed method was also tested for the case of the directional wave spectrum and the ship's speed inclusion.

The second application is to monitor subsea riser's deformed shape in real time using Extended Kalman Filter (EKF). The real-time monitoring of underwater risers, cables, and mooring lines by multiple sensors is in great demand but still very challenging. In this study, a new real-time riser monitoring method based on an EKF is proposed. It estimates the overall shape of riser in real-time utilizing the measured signals from multiple bi-axial (inclination and heading) inclinometers along the riser. The novel EKF algorithm is shown to be robust against sensor noises and successfully reproduces the actual riser profiles at each time step, which has been verified by multiple tests through numerical simulations. For verification, a turret-moored FPSO (Floating Production Storage and Offloading) with a SCR (Steel Catenary Riser) is employed in four different random waves and currents. Subsequent algorithms are also developed so that the corresponding bending and axial stresses along the riser can also be estimated in real time from the obtained riser shape, which can further be used for the real-time estimation of fatigue-damage accumulation.

DEDICATION

This dissertation is dedicated to my brilliant, loving and supportive wife, Jungkyung Min, our sweet, and kind-hearted girl, Grace Kim, exuberant and cute little boy Sean Kim, and to my always encouraging, ever faithful parents, Guibo Bae and MoonJa Song.

ACKNOWLEDGEMENTS

First and foremost, I would like to express my sincere appreciation to my advisor, Professor Moo-Hyun Kim, for his generous support of my Ph.D. research, for his great guidance and motivation.

I would like to appreciate Professor Sharath Girimaji and Prof. Robert Randall, for their continuous guidance and support throughout my Ph.D. research. Also, I would like to thank my committee members, Prof. Raktim Bhattacharya, for their valuable guidance thought my Ph.D. research. I also thank my colleagues in the Smart Ocean Systems Laboratory, Dr. Chung-Kuk Jin, WooChul Chung and JeongYong Park for sharing research ideas and their encouragement. In particular, I appreciate many colleagues, Dylan Blakeslee, Jaewon Kim, Lance Lane, Nabil Moosajee, Jonathan Beechner and Sophia Eli Esteban, for their much and continuous help with TAMU XPRIZE team.

Last but not least, I really thank my family and family-in-law for their love and continuous encouragement, and my wife Jungkyung Min for her love, support and greatest sacrifice so that I can complete my degree successfully.

CONTRIBUTORS AND FUNDING SOURCES

Contributors

This work was supervised by a dissertation committee consisting of Professors Moo-Hyun Kim, Sharath Girimaji and Robert Randall of the Department of Ocean Engineering and Professor Raktim Bhattacharya of the Department of Aerospace. All work conducted for the dissertation was completed by the student independently.

Funding Sources

This work regarding wave estimation was a part of the project titled 'Real-time Sea State Estimates and Applications' funded by the Daewoo Shipbuilding & Marine Engineering (DSME) under Grant Number TEES 410200.

And for the riser monitoring, there are no outside funding contributions to acknowledge related to the research and compilation of this document.

TABLE OF CONTENTS

Page

LIST OF FIGURES

Page

LIST OF TABLES

Page

CHAPTER I

INTRODUCTION*

The major topics in this dissertation is the development of ocean wave estimation algorithm using the adaptive Kalman filter in CHAPTER II and riser deformed shape monitoring algorithm using extended Kalman filter presented in CHAPTER III.

The work presented in this dissertation is based on the paper 'Real-time inverse estimation of ocean wave spectra from vessel-motion sensors using adaptive Kalman filter' published in Applied Sciences (Kim et al., 2019). The copyright of the published journal paper is retained by authors.

Introduction for Chapter II

An autonomous ship or unmanned ship is one of the promising technologies in the field of shipbuilding and shipping. It can reduce the ship operating cost, ship accidents, and attacks by pirates (Minter, 2017). In order for an unmanned ship to become a reality, efficient real-time estimation of incoming wave can play a vital role. For instance, unmanned vessels need to navigate the designated route automatically, while avoiding the path of collision-risk or storms. Another mission for route optimization (Jokioinen, 2015) is to minimize fuel consumption or navigation time when

* Parts of this chapter have been reprinted from [Kim, HanSung, HeonYong Kang, and Moo-Hyun Kim. "Real-time inverse estimation of ocean wave spectra from vessel-motion sensors using adaptive kalman filter." Applied Sciences 9, no. 14 (2019): 2797. Copyright 2019 by the authors]

considering wave added resistance. In this regard, the real-time inverse estimation of incoming waves from vessel-motion sensors is very essential.

The e-Navigation strategy, which is defined as “the harmonized collection, integration, exchange, presentation, and analysis of marine information on board and ashore by electronic means to enhance berth to berth navigation and related services for safety and security at sea and the protection of marine environment” was proposed at the 81st meeting of the Maritime Safety Committee (MSC) in 2005 by the United Kingdom, United States, and other countries. The e-navigation Strategy Implementation Plan (SIP) was approved by MSC 94 in 2014. The initial tasks that were included in the SIP are expected to be completed by 2019 (International Maritime Organization, 2019). The on-board real-time estimate of the wave spectrum is a key element in unlocking in-situ offshore sea state information.

Although multiple methods exist for wave-spectrum estimation, such as radar (Al-Habashneh et al., 2018), satellite (Jackson et al., 1985), or buoy (Gorman, 2018), they require expensive equipment or time-consuming post-processing. As an alternative, one can consider a method of estimating incoming ocean waves from motion sensors on board.

The responses occur when wave loads act on a vessel. Conversely, the method of estimating the ocean wave by measuring the vessel motion is a kind of ‘inverse problem’ i.e., estimating the input from the response output. The procedure for estimating wave spectra in this way can be classified into ‘parametric’ and ‘non-parametric’. The non-parametric method is general. The Kalman filter can be regarded as a non-parametric

method that can be applied to any sea states. The conventional methods for solving the inverse problem involve substantially heavy computations, such as the Monte-Carlo method, for resolving the uniqueness problem, which means that multiple different inputs can result from a single output. When compared to those costly and time-consuming methods, the use of Kalman filter can be an alternative inexpensive solution to achieve the real-time on-board estimation of incoming waves. The Kalman filter is fast enough to measure in real time, easy to include the forward speed of the ship, and capable of compensating sensor noises and model errors.

The research using the Kalman filter for the inverse estimation of ocean waves is very rare until recently despite the powerful advantages of the Kalman filter. Two papers (Pascoal et al., 2017; Pascoal and Soares, 2009) are representative. The Kalman filter in Pascoal and Soares (2009) was applied to ocean wave estimation while using synthesized motion data. In Pascoal et al. (2017), the motion data of the actual field from a real ship was used. Nevertheless, this research is still in the development phase and it needs to be elaborated (Nielsen and Stredulinsky, 2011). Figure 1 demonstrates the overall process of the wave spectrum estimation process while using the Kalman filter.

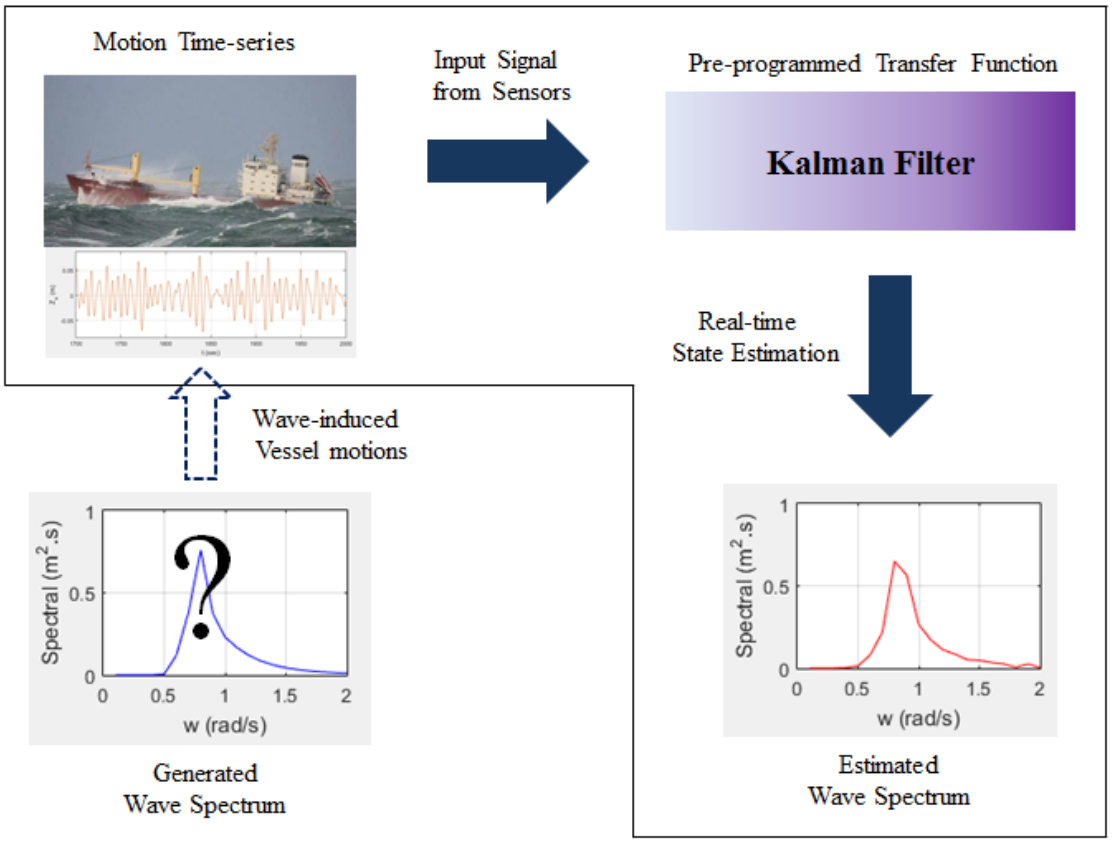

Figure 1 Wave Spectrum Estimation Process Using Kalman Filter.

The Kalman filter is difficult to estimate high-frequency waves where the vessel's response is weak. Thus, in the case of large vessels, additional high-accuracy sensors may be utilized or other responses sensitive to high frequencies may be used. More research is needed on this issue and the Kalman filter setting alone may be the solution (Pascoal et al., 2017).

NOAA Forecast Snapshot for North West Atlantic of 'NMWW3 20181008 t18z 60h forecast' (Svašek Hydraulics, 2018) shows the actual sea conditions at North West Atlantic. They represent significant wave height, Hs and spectral peak period, Tp at the

same time, respectively. It can be seen that high-frequency waves with a Tp less than 5 s (or $\omega > 1.257$ rad/s) occupy a large portion in the snapshot. Therefore, estimating those wide-spreading high-frequency waves is of importance. Accordingly, it is important to design the Kalman filter, so that the high-frequency waves can also be estimated in a robust manner.

In Pascoal and Soares (2009), the frequency range was limited up to 1.15 rad/s since higher frequencies can cause problems when using Kalman filter. However, in this paper, the estimation range was extended to 2.0 rad/s, so that those high-frequency waves can be recovered. The cause of overestimation at the high-frequency zone and its remedy are investigated and new algorithms that suppress those overestimations are proposed. The numerical test results are promising for various wave conditions, vessel types, and sensor errors. Moreover, the present Kalman filter technique applied to the inverse problem successfully reproduces, not only the real-time wave spectrum, but also the real-time wave elevation. In this paper, 'wave elevation' means the time series of irregular wave profile. The estimation of wave elevation is very important for the active control in many ocean-engineering applications. As far as the authors know, the real-time inverse estimation of wave elevation by the Kalman filter cannot be found in the open literature.

The developed technology is relatively inexpensive and it has an advantage that the wave can be continuously estimated along a ship's passage. According to recent statistics, the number of merchant ships sailing around the world in 2017 is about 50,000 (Statistica, 2018) i.e., there are already 50,000 potential sensors on those vessels over

the world, which means that a continuous build-up of big real-time ocean wave data through the inverse algorithm is possible with a robust network among ships.

Introduction for Chapter III

Service-life extension of mooring lines and risers is an important issue for many existing floating offshore platforms. The service life can be extended by verifying structural integrity from a thorough structural inspection (Keprate and Ratnayake, 2015) or by analyzing various sensor signals from the monitoring system.

In the deep water of ocean, the sensor-based structural monitoring plays a crucial role in detecting any malfunction or initial damage of riser/mooring and preventing subsequent failure. In particular, the real-time monitoring from the deeply-submerged sensors is even more challenging due to the difficulty in transmitting/receiving signals in real time and lack of real-time-analyzer algorithms. Mostly in the current state of the art, sensors are powered by the battery, and the retrieved sensor signals by ROV (Remotely Operated Vehicle) are post-processed by engineers to detect any malfunctions or initial structural problems. In this case, any serious real-time malfunctions and structural problems cannot be detected and remedied in a timely manner. The riser safety is particularly important in view of potential oil spill and risk of hosting units. If oil leakage associated with the damage happens, fatal environmental pollution is inevitable. On the other hand, continuous estimation of riser fatigue is necessary to real-time monitor the accumulated fatigue damage, which is also important for the extension of service life.

The best way to monitor the underwater riser and check its structural robustness and fatigue life is to analyze the time-history of elastic responses and stresses. The use of a numerical simulation tool is limited since the real-time measurement of the wind-wave-current of the spot is rarely available or used (Bitner-Gregersen et al., 2013). In this regard, the acquisition and analysis of elastic responses from sensor signals are more practical and beneficial. As one of the methods, Choi and Kim (2018) recently proposed a Multi-Sensor Fusion (MSF) system, which uses the GPS of the platform and multiple inclinometers along the riser. They showed that the use of angle sensors is more effective and robust in tracing riser profile in real time than using accelerometers since dual-time integration is not necessary hence the result is less influenced by sensor noises. Their estimation method was for two-dimensional (2D) plane and based on FE (finite-element) formulations.

In this study, a totally new, novel approach, i.e., the Extended-Kalman-Filter (EKF)-based real-time riser-monitoring system, is suggested with the floater-GPS and multiple-inclinometer signals. As a significant extension of the Choi and Kim (2018)'s approach, arbitrarily-shaped risers in the 3D space are considered. Figure 2 presents the overall process of the riser-shape estimation using the EKF. The detailed methodology and algorithm are explained in the ensuing sections. It is of critical importance to validate the developed theory. In this regard, first, the platform-mooring-riser coupled-dynamics time-domain simulation was performed with a series of bi-axial (inclination and heading) numerical inclinometers along the riser. Second, after sensor noise was artificially added to the acquired signals, the EKF was applied for the real-time

estimation of the instantaneous riser profile. Third, the EKF-estimated profile was directly compared with the actual riser profile for all time steps. Last, the time-histories of axial and bending stresses were also real-time estimated from the traced riser motions based on author-developed FE formulations so that it can be used for the assessment of fatigue-damage accumulation.

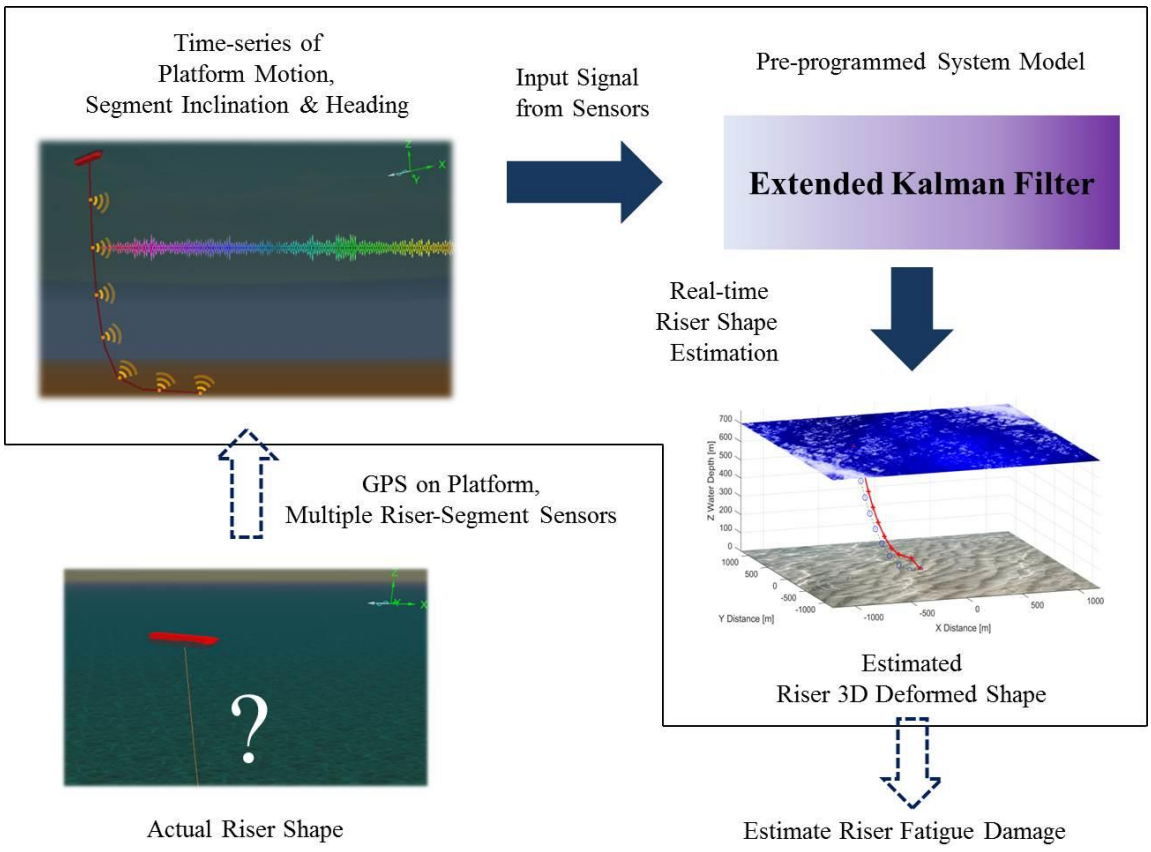

Figure 2 Process of Real-Time Riser-Shape Estimation Using the Extended Kalman Filter.

CHAPTER II

REAL-TIME INVERSE ESTIMATION OF OCEAN WAVE DIRECTIONAL SPECTRA FROM VESSEL-MOTION SENSORS USING KALMAN FILTER*

Formulation for Modeling

Conventional Kalman Filter

The Kalman filter is an algorithm that estimates the state based on the statistical properties with the measurement while using sensors. The sensor contains sensor errors and the modeled governing equation does not perfectly match the system. Kalman filtering is applied to the system model of Equations (1) and (2) in the state space. It assumes that there exists a model error w in the state x and a sensor error v in the measurement z during the transition to the next time step.

$$x_{k+1} = \phi_k x_k + w_k \tag{1}$$

$$z_k = H_k x_k + v_k \tag{2}$$

where

* Parts of this chapter have been reprinted from [Kim, HanSung, HeonYong Kang, and Moo-Hyun Kim. "Real-time inverse estimation of ocean wave spectra from vessel-motion sensors using adaptive kalman filter." Applied Sciences 9, no. 14 (2019): 2797. Copyright 2019 by the authors]

x_k = process state vector
ϕ_k = state transition matrix
w_k = model error vector
z_k = measurement vector
H_k = output matrix
v_k = sensor error vector

The covariance for each of the two errors is given by;

$$Q = E[w_k w_k^T] \tag{3}$$

$$R = E[v_k v_k^T] \tag{4}$$

The Kalman filter keeps reducing the prediction error of the state x through the recursive calculating process. The process is made up of four steps, as described in Figure 3. The superscript '-' means a predicted value for the next time step. Otherwise, it means a calculated (or estimated) value from measurement at the current step.

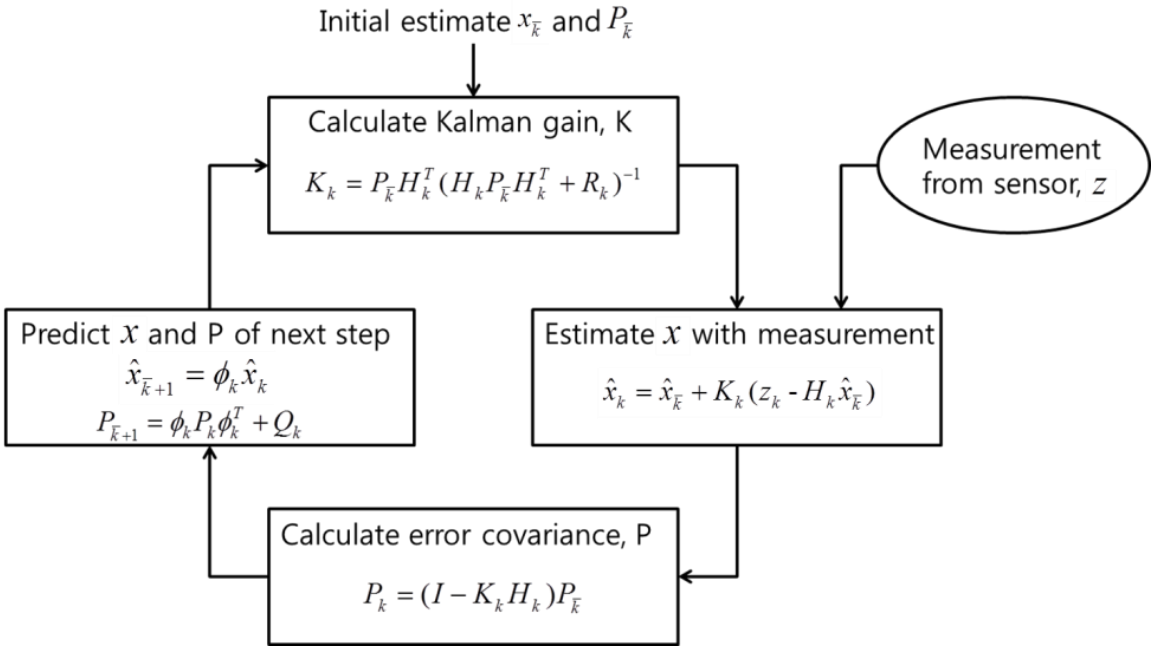

Figure 3 Kalman Filter Loop. Adapted from Brown and Hwang (1992).

where,

$x_{\bar{k}}$ = predicted state vector

x_k = estimated state vector

$P_{\bar{k}}$ = predicted error covariance matrix

P_k = estimated error covariance matrix

K_k = Kalman gain

Q_k = model error covariance matrix

R_k = measurement (sensor) error covariance matrix

The initial state $x_{\bar{1}}$ is to be estimated and the initial error covariance, $P_{\bar{1}}$ should be determined by the designer. If initial P ($P_{\bar{1}}$) is too small, then it will result in small Kalman gain, K by Equation (5) in the beginning of calculation. A small K means giving more weight to sensor measurement than prediction. Subsequently, at the beginning of

the filtering, the measurement is relatively neglected and the prediction is overly counted. In other words, the $P_{\bar{1}}$ determines the initial convergence rate of the state x. Small P delays the initial convergence rate. Therefore, when the designer does not have prior knowledge of x, reasonably large initial error covariance, $P_{\bar{1}}$ should be set (Simon, 2006).

R is measurement error covariance that is generally determined from the error performance of the given sensor. An adaptive *R* may be applied when the sensor error is not statistically constant in the actual filtering process. *H* is the matrix that defines the relationship between state, *x* and measurement, *z*. In the estimation step, optimum *x* is calculated by using the weight factor, *K* in the Equation (6).

$$K_k = P_{\bar{k}} H_k^T (H_k P_{\bar{k}} H_k^T + R_k)^{-1} \tag{5}$$

$$\hat{x}_k = \hat{x}_{\bar{k}} + K_k (z_k - H_k \hat{x}_{\bar{k}}) \tag{6}$$

$$P_k = (I - K_k H_k) P_{\bar{k}} \tag{7}$$

In the prediction step, *P* is increased by model error covariance, *Q*. *Q* is a design parameter that can be adjusted by the designer. This process is repeated:

$$\hat{x}_{\bar{k}+1} = \phi_k \hat{x}_k \tag{8}$$

$$P_{\bar{k}+1} = \phi_k P_k \phi_k^T + Q_k \tag{9}$$

The conventional Kalman filter is not directly suitable for practical applications. Therefore, the research that is related to using Kalman filter mainly focuses on the design of an adaptive type to fit a specific model, including the optimization of the design factors, R and Q. The optimized Q and R lead to the improvement of estimation performance of the filter. In the following, we explain how the algorithm can be utilized for the real-time inverse estimation of ocean wave spectra and elevation from vessel-motion sensors.

Main Formulas for Inverse Wave Estimation

References (Pascoal et al., 2017; Pascoal and Soares, 2009) presented the essential formulas, including the output matrix as Equation (11) i.e., the use of vessel's hydrodynamics for wave spectrum estimation by utilizing the Kalman filter. Equations (1) and (2) are used as the system model equations. The state transitional matrix ϕ_k is identity and X is the complex wave amplitude in this case.

As in Equation (10), this model has an important premise. It assumes that the measured vessel motion is the result of incoming waves that were weighted by a transfer function (Pascoal et al., 2017). The vessel's transfer functions are complex, which means that they have amplitude and phase. The amplitude of transfer function is called response amplitude operator (RAO).

$$z(t) \cong \mathrm{Re}\left(\sum_{j=1}^{n_f} TF_j \times (x_{2j-1} + i x_{2j})(\cos(\omega_j t) + i \sin(\omega_j t))\right) \tag{10}$$

where

z: vessel motion

x_{2j-1}: real part of complex wave amplitude

x_{2j}: imaginary part of complex wave amplitude

ω: intrinsic frequency of harmonic

n_f: number of harmonics to estimate

TF_j: complex-valued transfer function for frequency j

The matrix type of H becomes

$$H_{jkl} = \begin{bmatrix} \mathrm{Re}(TF_{jl})\cos(\omega_j k\triangle t) - \mathrm{Im}(TF_{jl})\sin(\omega_j k\triangle t) \\ -\mathrm{Im}(TF_{jl})\cos(\omega_j k\triangle t) - \mathrm{Re}(TF_{jl})\sin(\omega_j k\triangle t) \end{bmatrix}' \tag{11}$$

where

j: jth frequency

k: kth time instant

l: lth response

H_{jkl}: output matrix

$\triangle t$: time step interval

In Pascoal and Soares (2009), the conventional Equations (5), (6), and (9) were used for prediction and estimation. However, in the prediction of x, Equation (13) was used instead of Equation (8) i.e., the average value for three-time instants is applied as the state prediction value, $\hat{x}_{\bar{k}+1}$. In addition, P was computed by Equation (12) instead of Equation (7). Equation (12) was used for stability reasons and it is called the 'Joseph Form' (Ladetto, 2000). In fact, Equation (7) is derived from Equation (12). Accordingly, either can be used to calculate P.

$$P_k = (I - K_k H_k)P_{\bar{k}}(I - K_k H_k)' + KRK' \tag{12}$$

$$\hat{x}_{\bar{k}+1} = 1/3 \cdot (\hat{x}_k + \hat{x}_{k-1} + \hat{x}_{k-2}) \tag{13}$$

According to Pascoal and Soares (2009), the adaptive approach has been considered, because it cannot be assured that the process is completely known and that the steady state is reached due to the change of sea condition and ship's heading. Equation (14) is the Adaptive R equation. The 'diag' means taking the diagonal from a matrix into a vector form and vice-versa.

$$R = diag^2(E[z_k - H_k \hat{x}_{\bar{k}},\ \ (z_k - H_k \hat{x}_{\bar{k}})^{'}]) + H_k P_{\bar{k}} H_k^{'} \tag{14}$$

The initial value of the state is as follows:

$$\hat{x}_{\bar{1}} = 0 \tag{15}$$

In the present paper, the above Equations (1), (2), (5) –(11), and (15) are applied. The rest of the equations and other conditions are set to suit the vessel that is considered and computer specifications.

Using the state, *x*, which is an estimated value from the filter, the wave spectrum and wave elevation can be calculated from the following equations. The reconstruction of both wave spectra and wave elevation is possible since the state variable *x* and motion transfer function TF are complex variables:

$$S_{\varsigma}(\omega_i) = 0.5 \times \frac{1}{\Delta\omega_i} \times (\hat{x}_{2i-1}^2 + \hat{x}_{2i}^2) \tag{16}$$

$$\varsigma(t) = [\cos(\omega_1 \cdot t),\ -\sin(\omega_1 \cdot t) \ldots \cos(\omega_n \cdot t),\ -\sin(\omega_n \cdot t)][\hat{x}_1\ \hat{x}_2 \ldots \hat{x}_{2n-1}\ \hat{x}_{2n}]' \tag{17}$$

where

$S_{\varsigma}(\omega)$: wave spectrum

$\Delta\omega$: frequency interval

ς : wave elevation

Regarding the determination of *R* and *Q* values, *R* can be determined based on the real sensor's performance before or while operating the filter. Thus, it is practical to specify *R*. On the other hand, *Q* is generally more difficult to determine, because *Q* is sometimes dynamically varying during filtering and it cannot be directly observed in the process of estimation. In a simple process, satisfactory estimation can sometimes be obtained by setting the appropriate *Q*. The tuning of *Q* and *R* can provide excellent filter performance, regardless of whether there is a reasonable basis for choosing the parameters (Bishop and Welch, 2001). Thus, Holzhuter (1997) described *R* and *Q* as model-specific "tuning knobs" that determine filter performance and expressed choosing them as "spirit of observer design".

First, $P_{\bar{1}}$ was set large enough to make the initial convergence fast, as Equation (18). This is because the initial state is uncertain. In the long run, this initial value does not make much difference in the filter performance (Simon, 2006). Subsequently, to design the proper fixed value of *Q*, it is assumed that there is no measurement error,

which means that R is 0. From a number of tests, the appropriate Q value was set as Equation (19), so that the estimation is good enough and P does not diverge.

$$P_{\overline{1}} = \begin{bmatrix} 50_{i\times i} & 0 \\ 0 & 50_{i\times i} \end{bmatrix} \tag{18}$$

$$Q = \begin{bmatrix} 10^{-5}{}_{i\times i} & 0 \\ 0 & 10^{-5}{}_{i\times i} \end{bmatrix} \tag{19}$$

where

i: half the length of x

Only heave motion is considered to simplify the case. R was calculated by Equation (20) and it remains as the fixed value while the filter is running. The standard deviation of heave motion sensor error is set to be 2.3 cm, referring to the test result of a commercial product (SBG Systems, 2018). Thus, when only heave is considered, R is 5.29×10^{-4}, which is the square of 0.023 m.

$$R = diag\begin{pmatrix} \sigma_1{}^2 \\ \sigma_2{}^2 \\ \vdots \\ \sigma_{l-1}{}^2 \\ \sigma_l{}^2 \end{pmatrix} \tag{20}$$

where

σ : sensor noise (error) standard deviation

l: *l*th response or mode

A freely floating FPSO (Floating Production Storage and Offloading) in Figure 4 was selected as the vessel. The total number of 1831 quadrilateral panels was used after the convergence test. The details of the vessel are given in Kim and Kim (2015a). Figure 5 is the RAO of the FPSO. The vessel's transfer function (or RAO) was numerically computed while using a three-dimensional (3D) diffraction/radiation panel program, WAMIT software.

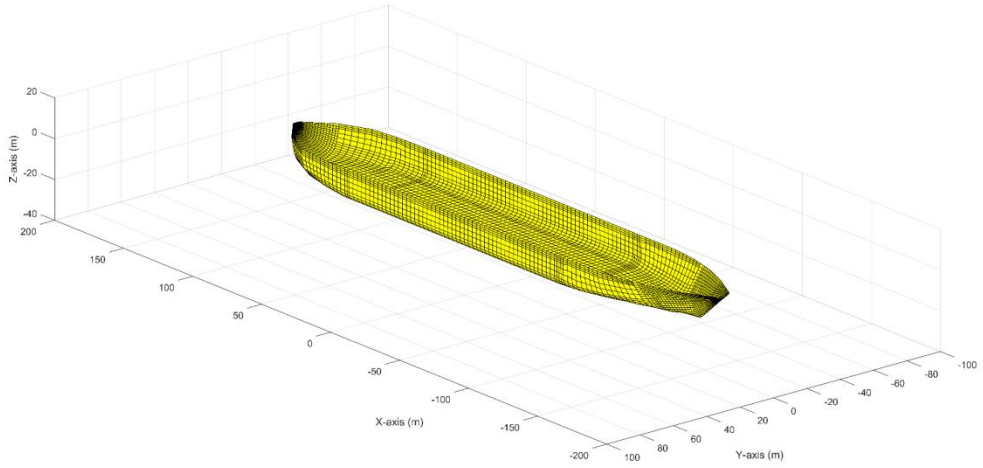

Figure 4 Floating Production Storage and Offloading (FPSO) Mesh (LPP (length between perpendiculars): 310 m, B: 47 m, Draft: 15 m).

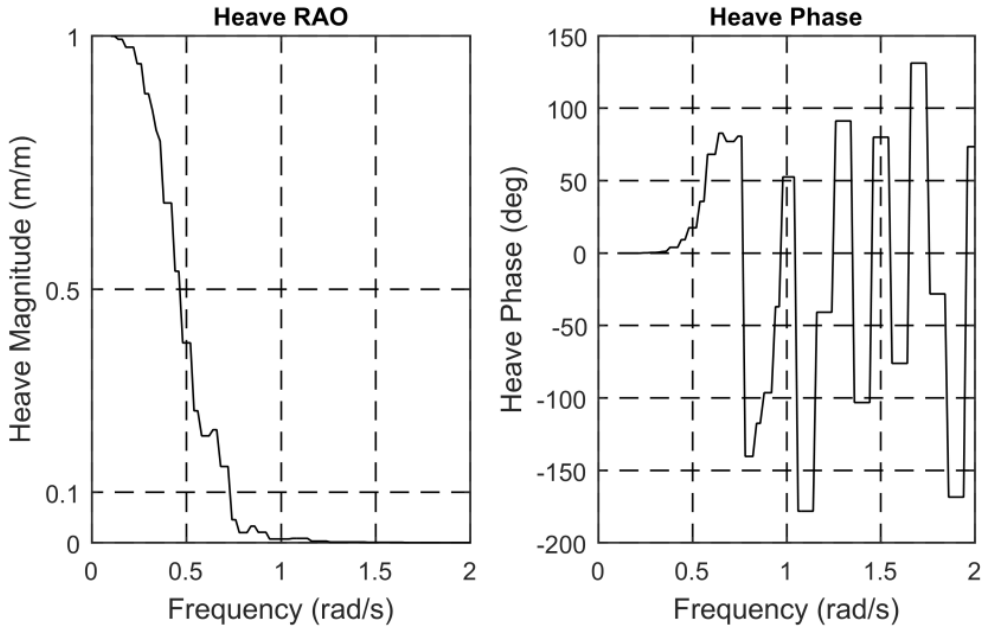

(a) RAO (b) Phase

Figure 5 Heave Transfer Function of FPSO.

A uni-directional JONSWAP wave spectrum with Hs = 2 m, Tp = 7 s, and enhancement parameter = 2.2 is considered. The significant wave height, Hs is defined as the average of the 1/3 largest waves. It can be calculated from either wave spectrum or wave time series. Tp is the spectral peak period. Hs and Tp are used as key index parameters since the purpose of the Kalman filtering is to inversely estimate the overall shape of the spectrum. Subsequently, the corresponding heave motion spectrum was calculated while using the calculated RAO. Afterwards, the corresponding irregular-motion time series were generated by Equation (29). Subsequently, a white noise that was equivalent to the standard deviation of sensor error 2.3 cm was artificially added (Figure 6). Afterwards, the motion-time-series data, including the sensor error, was

inputted to the present Kalman filter process. The frequency range of the white noise is set to be the same as that of input wave spectrum.

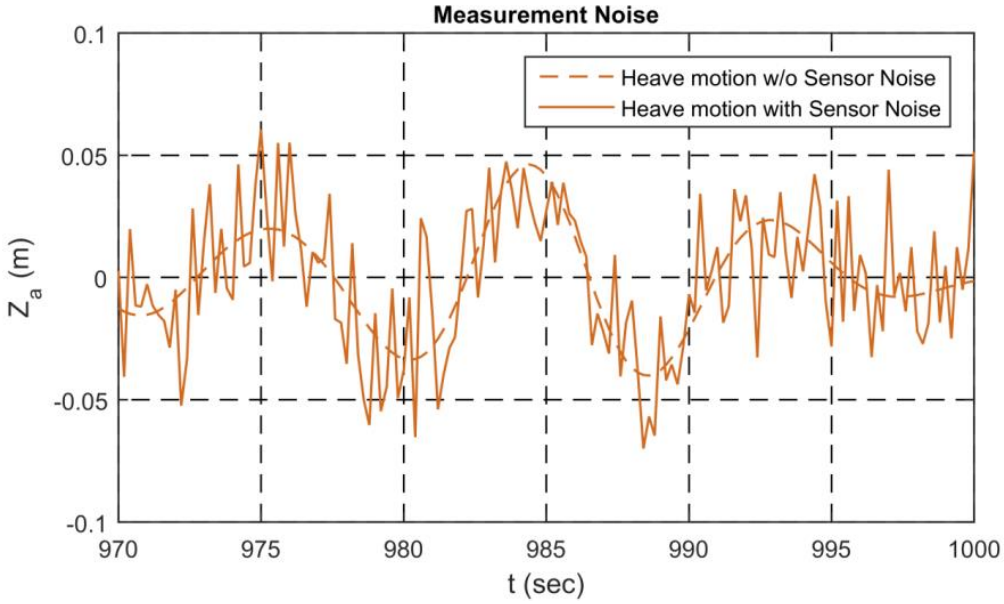

Figure 6 Time Series of Heave Motion with Sensor Noise.

The previous equations and conditions were applied. First, the frequency range was limited to 0.1~1.15 rad/s, as in Pascoal and Soares (2009). The Kalman filter was run for 1000 s. The real-time spectra were calculated during that time. The spectral estimation was good after the initial transient stage, as indicated in Figure 7. This shows that the Kalman filter is well designed up to this point. However, we found some problem when the frequency range is extended to higher-frequency regions, as shown in the next example.

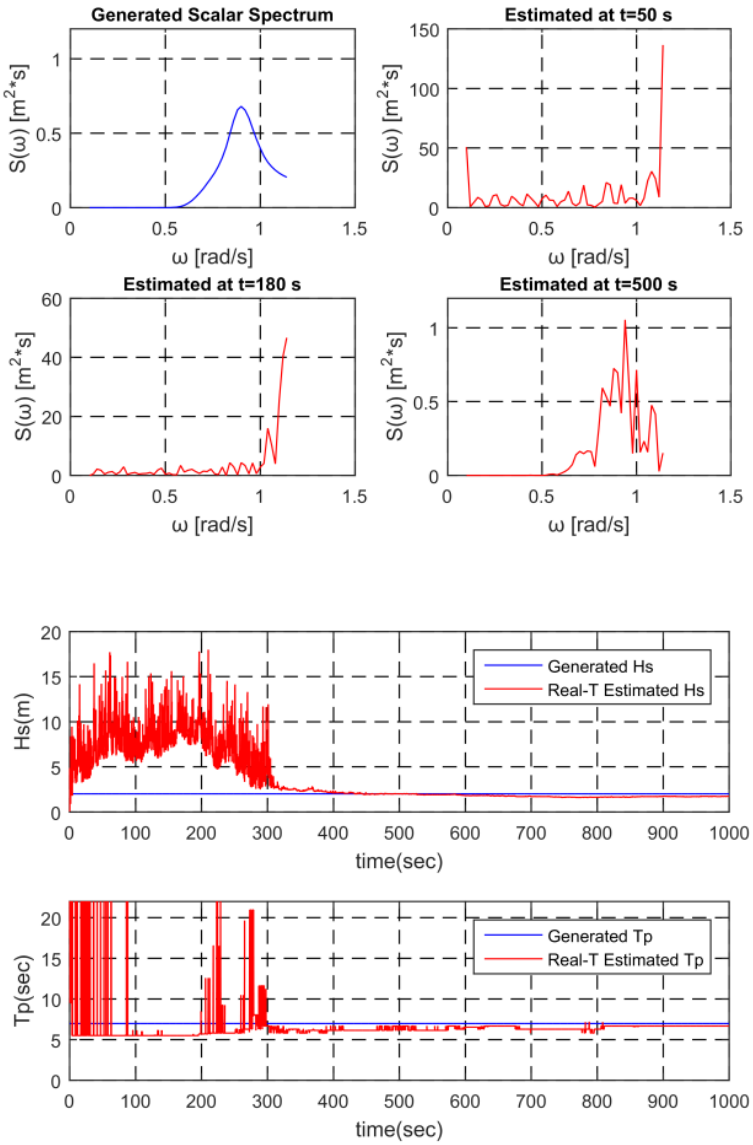

Figure 7 Generated and Estimated Spectrum / Evolution of Parameters (Hs = 2 m, Tp = 7 s, Frequency: 0.1~1.15 rad/s).

Design of Modified TF to Suppress Overestimation in High-Frequencies

The performance of the designed Kalman filter was examined when the frequency range is extended to 2.0 rad/s. In Figure 8, we start to see some problem i.e., excessive estimation of spectral amplitude in the high frequency region.

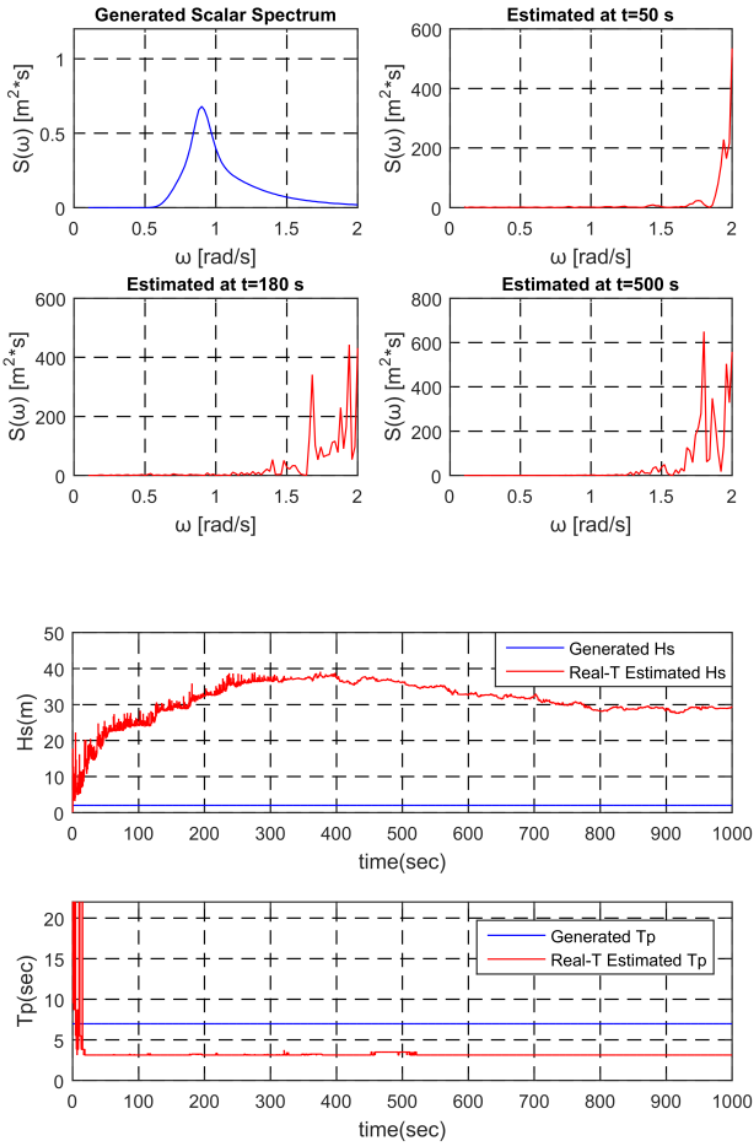

Figure 8 Generated and Estimated Spectrum / Evolution of Parameters (Hs = 2 m, Tp = 7 s, Frequency: 0.1~2.0 rad/s).

No overestimation occurred when the sensor error was removed. In case there is sensor error and RAO is intentionally amplified, so that its magnitude is more than 1 in all frequency region, overestimation did not occur. Therefore, it is expected that the cause of the overestimation at the high frequency region is the combination of sensor errors and small values of RAO. In order to better understand the phenomenon, the internal variables, P and K for every frequency component during the operation of the filter were analyzed.

Figure 9 shows a comparison of the changes of the internal variables P and the absolute value of K in the frequency domain during the Kalman filter operation for both cases i.e., (a) and (b) when the maximum frequency is 1.15 rad/s and (c) and (d) when the maximum frequency is changed to 2.0 rad/s. In the case of (a) and (b), the P and K values converge to proper values after initial transient stage. However, in the case of (c) and (d), the P and K values do not converge well and the errors in the high frequency region are particularly large. The convergence rates in the high frequency region are also very slow. This is due to Equation (7) of the 'Calculate P' step in the Kalman filter loop. P is decreasing each time step by the equation. The high-frequency region of $(I - K_k H_k)$ is close to 1, the element of an identity matrix, since the H is small in the high-frequency zone due to the motion characteristics (RAO) of the vessel. Therefore, the high-frequency region of P, which is multiplied by $(I - K_k H_k)$ every time step, slowly decreases.

P is a variable that determines K in Equation (5) of the 'Calculate K' step. The slow decreasing of P also slows down the convergence rate of K. Therefore, in Figure

9(d), the convergence speed of K also becomes slow. K is gain between the measured value and the predicted value in Equation (6) of ‘Estimate x with measurement’ step. The overestimated K in the high frequency range gives an excessive value of x, which is the estimated result. Essentially, the small response in the high frequency region of RAO with respect to the given sensor error causes an overestimation problem.

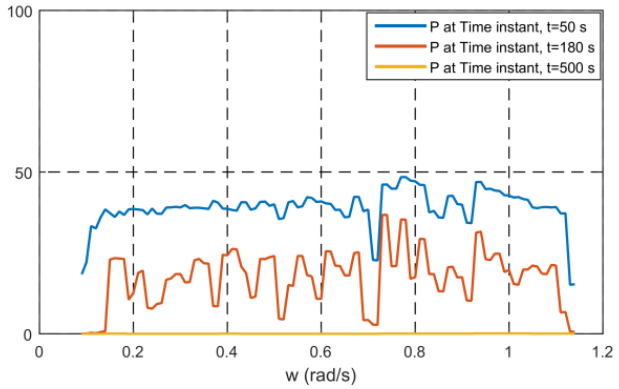

(a) P (to 1.15 rad/s)

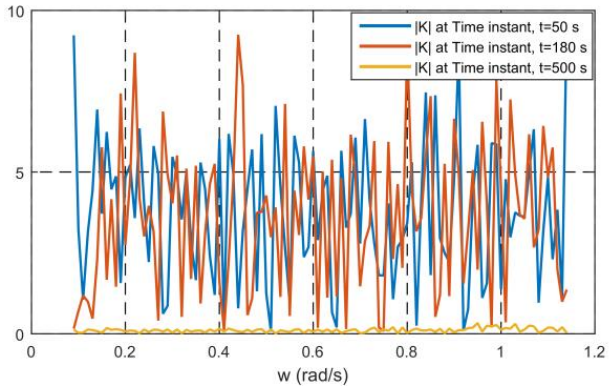

(b) K (to 1.15 rad/s)

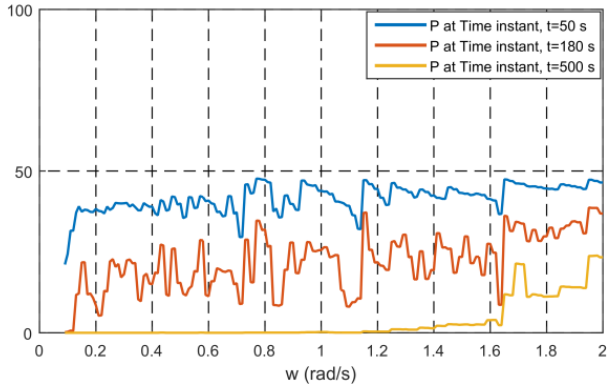

(c) P (to 2.0 rad/s)

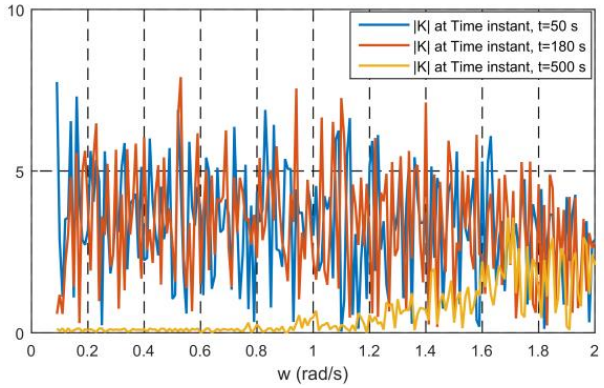

(d) K (to 2.0 rad/s)

Figure 9 Comparison of Error Covariance and Kalman Gain for Frequency Extension.

First, as a potential solution to overcome the phenomenon of overestimation in the high frequency region, while using multi-motion signals was attempted i.e., Surge, Sway, Roll, Pitch, and Yaw were added so that a total of six motions can be used. It may be possible that the ill behavior of heave in the high frequency region can be compensated by sensor fusion. The test results (Figure 10) show that the unfavorable behavior is improved when compared to the heave only case, but overestimation still occurs i.e., the generalization of Kalman filter technique to include all 6DOF motions helps the problem, but is not highly effective.

Meanwhile, the phenomenon of excessively amplified noise is mentioned as a problem of the inverse filter that is used in the image restoration field (Sundararajan, 2017). This problem can occur when the transfer function is zero or very small. If the measured signal has sensor error, it is more amplified at high frequencies. In the image restoration, the Wiener filter is used to solve this problem. In this regard, we applied the principle of the Wiener filter to the present the Kalman-filter technique, as described in the following.

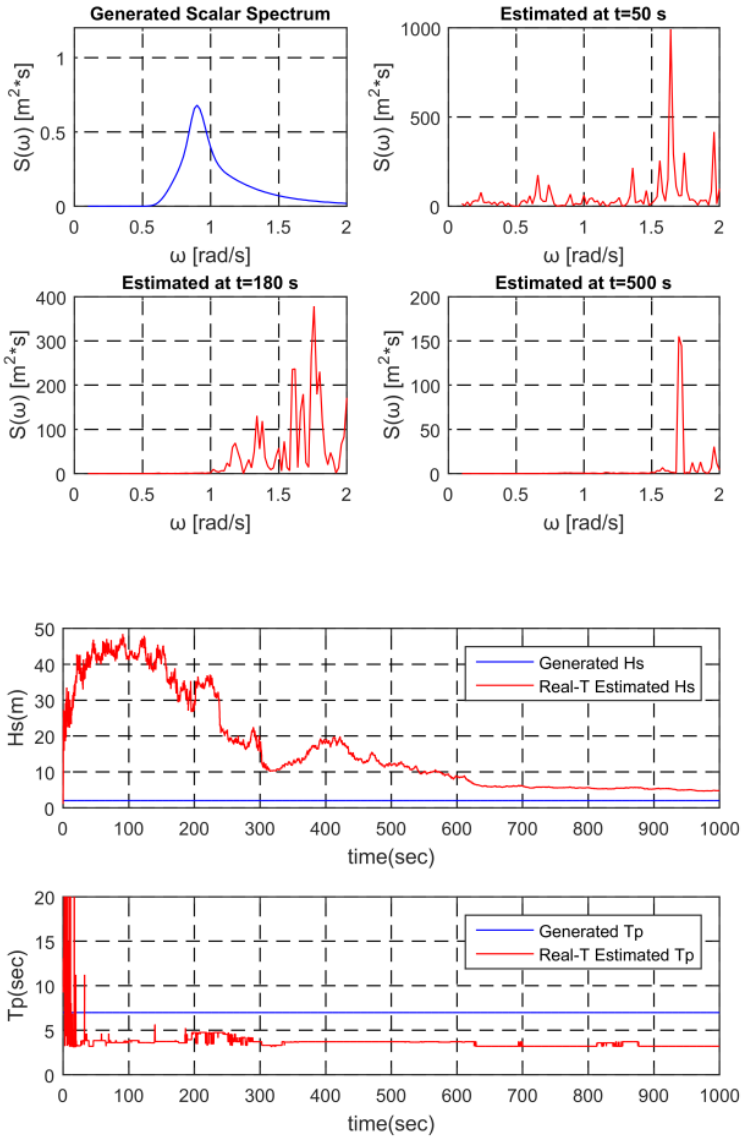

Figure 10 Generated and Estimated Spectrum / Evolution of Parameters Using Six Motion (Hs = 2 m, Tp = 7 s, Frequency: 0.1~2.0 rad/s).

Reference (Lagendijk and Biemond, 2009) explains some filters for original-image-restoration from blurred images. First, the Inverse filter is introduced. Assuming that the blurring function D, which is a sort of transfer function, is known, the inverse

filter can be directly used in the frequency domain to recover the original image. The observation equation can be expressed in the frequency domain, as;

$$G(u,v) = F(u,v)\, D(u,v) \tag{21}$$

where

G: observed image

F: original image

D: blurring function

The original image F(u,v) can be restored by filtering the observation G(u,v). The inverse filter $\frac{1}{D(u,v)}$ provides a perfect estimate of the original image in the case of no noise as follows:

$$\hat{F} = G(u,v)\frac{1}{D(u,v)} \tag{22}$$

where

$\hat{F}$: estimated image

However, if there is sensor noise N(u,v) as Equation (23), the result will be filtered noise i.e., the second term in Equation (24) and the desired image. The term is called “Inverse Filtered Noise” (Lagendijk and Biemond, 2009). The inverse filter

typically has very high gain at certain frequencies, where D(u,v) is small. The amplified noise at those frequencies will dominate the result. Figure 11 is the schematic diagram of noise amplification. In the bottom right of the figure, $\hat{F}$ the estimated image is amplified (red solid line) in the high frequency region by the inverse filter.

$$G(u,v) = F(u,v)\,D(u,v) + N(u,v) \tag{23}$$

$$\hat{F} = G(u,v)\frac{1}{D(u,v)} = \{F(u,v)\,D(u,v) + N(u,v)\}\frac{1}{D(u,v)} = F(u,v) + \frac{N(u,v)}{D(u,v)} \tag{24}$$

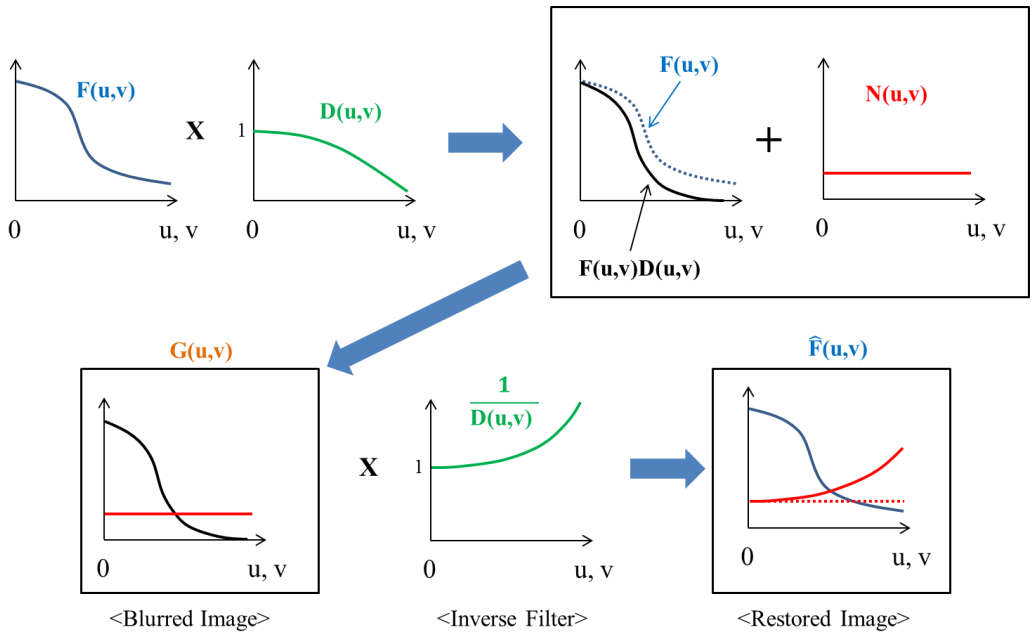

Figure 11 Schematic Diagram of Noise Amplification.

To overcome the noise sensitivity of the inverse filter, the Weiner filter can be used. It is defined in the frequency domain, as;

$$W(u,v) = \frac{D(u,v)^*}{(|D(u,v)|^2 + \frac{S_n(u,v)}{S_f(u,v)})} \quad \text{(When } S_n(u,v) \text{ or } S_f(u,v) \text{ is unknown, } \frac{S_n(u,v)}{S_f(u,v)} \to C) \tag{25}$$

where

$D(u,v)^*$: complex conjugate of D(u, v)

$S_n(u,v)$: power spectrum of the noise

$S_f(u,v)$: power spectrum of the ideal image

C: constant

In fact, the Wiener filter is used to minimize the mean square error between the estimated signal and the desired signal. It produces an estimate of the desired signal of a measured noisy signal, in principle, while assuming that original signal and noise are known (Wikipedia, 2019). However, it is common to use an approximation when the power spectra are not known. It means that the ratio $S_n(u,v)/S_f(u,v)$ can be substituted by a constant C. The C can be chosen by logistic trial and error (McAndrew, 2015; Sundararajan, 2017) as Equation (25). In this paper, the original signal i.e., wave spectrum is assumed to be unknown. Accordingly, C can be determined by trial and error.

In Figure 12, through comparison with inverse filter (1/D), we see the effect of Wiener filter W(u, v). The Wiener filter suppresses the gain by a certain amount to suppress amplified noise in the frequency region where the magnitude of Inverse filter is too large. To see the effect of Wiener filter with respect to transfer function D, the

inverses of both Inverse filter and Wiener filter are plotted in Figure 13; 1/W(u, v) increases the very small gain of D in the high-frequency region.

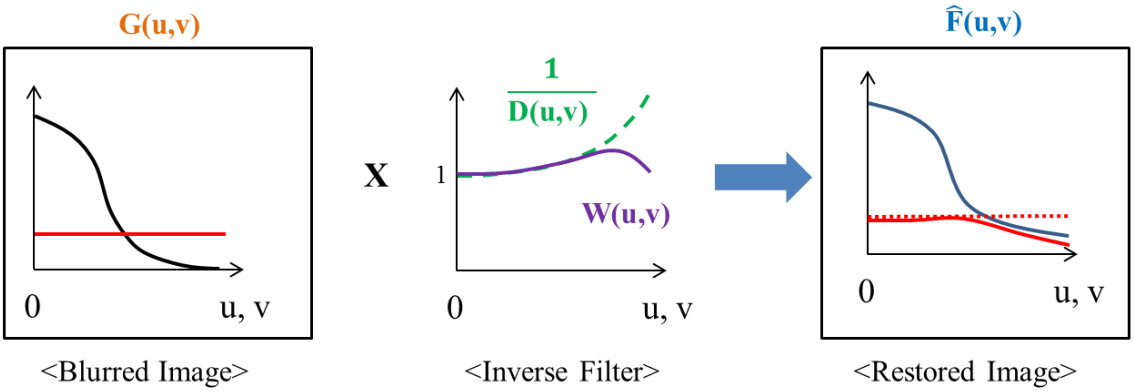

Figure 12 Effect of Wiener filter.

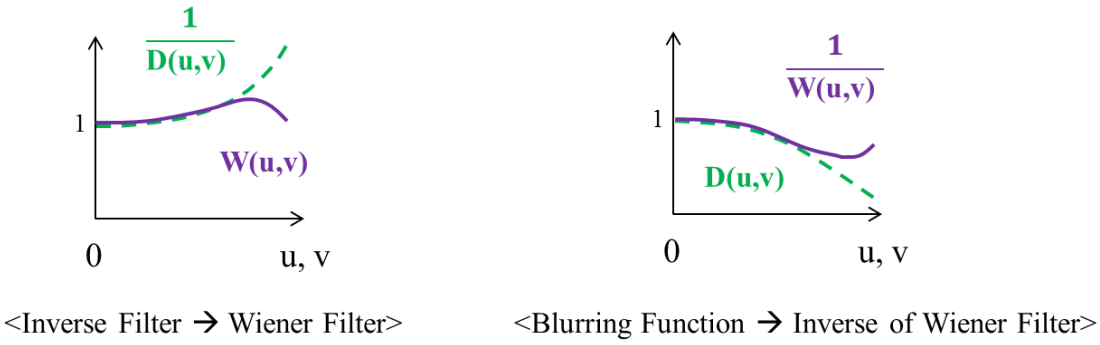

Figure 13 Effect of Inverse of Wiener filter to Compare to D(u,v).

When comparing the wave estimation with the image restoration, F corresponds to wave, G to ship motion, and D to motion TF or H, respectively. Unlike the Inverse filter, the Kalman filter is the recursive filtering algorithm finding more accurate state with more measurements. However, at a particular time step, the Kalman filter also

computes the original signal in the inverse direction from the measurement with sensor noise, while using the pre-programmed output equation between the state and measurement.

We applied the principle of Wiener filter to the present Kalman-filter technique for the inverse wave estimation in the frequency region where the magnitude of Inverse filter is too large. The issue is that the inverse form of transfer function like (1/D) cannot directly be applied to the Kalman filter. Rather, it is not in inverse form, but TF is included in H as equation (11). Therefore, we had to devise a way to modify the TF while keeping the Wiener's effect the same. As mentioned earlier, the effect of the Wiener filter is to increase the gain of D by a certain amount in the frequency region where the magnitude is 0 or too small.

If Wiener filter W is used instead of Inverse filter (1/D) in Equation (24), noise term N/D is eliminated, and $G \times W = F$ is established. Subsequently, $G/F = 1/W$. Let us put this as Equation (a). Meanwhile, in the Equation (6) in the Kalman filter, it is used as Z-HX. If we change these as variables of image restoration, it is G-DF. Assuming that there is noise, it is not 0 but G-DF = N. Afterwards, $D = G/F - N/F$ and let us put this as Equation (b). When we input 1/W to D in the Equation (b), the Equation (b) becomes $G/F = G/F - N/F$ by the Equation (a) and N/F becomes 0. That is, if we use 1/W instead of D in Kalman filter, we can obtain the effect of Wiener filter and eliminate the noise. In conclusion, the modified TF as Equation (26) was applied to the Kalman filter in the inverse form of Wiener filter. For easy comparison, Figure 14 is given.

$$\frac{(|\,TF\,|^2 + C)}{TF^*} \tag{26}$$

where

TF^* : complex conjugate of TF

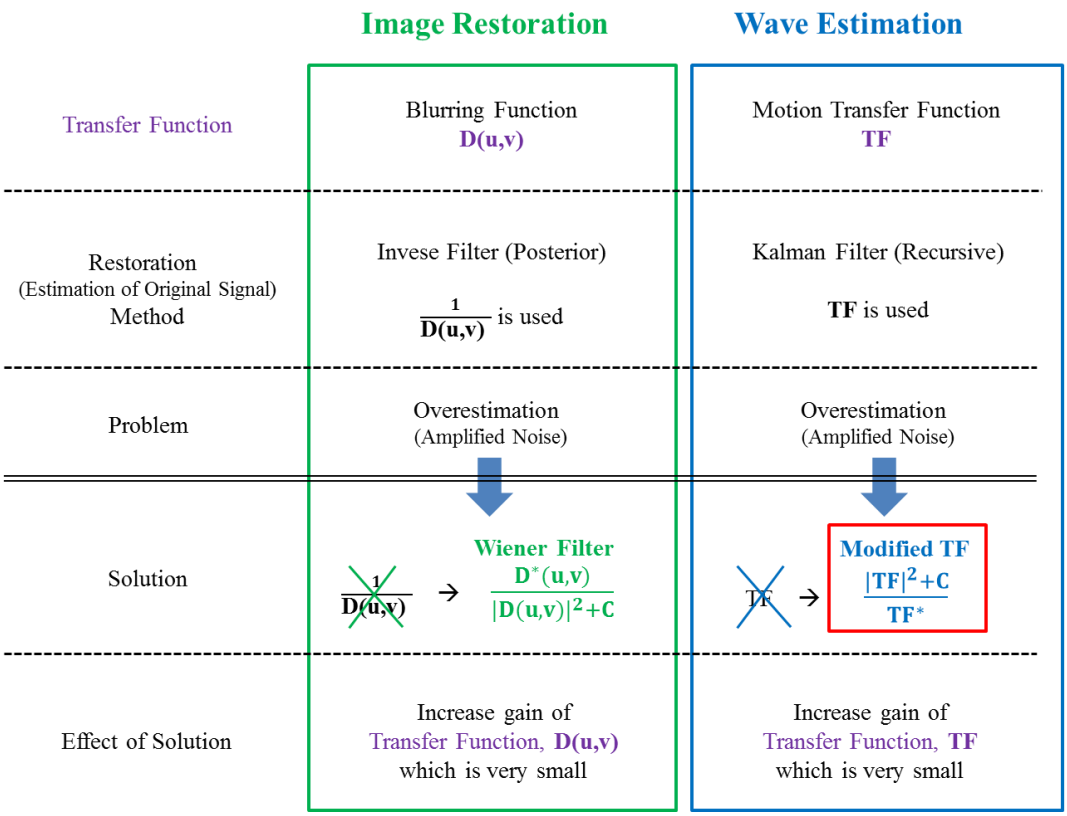

Figure 14 Comparison of Image Restoration and Wave Estimation.

Through trials and errors, C was found to be 2.5×10^{-5}, when the sensor noise (error) standard deviation is 0.023 m. Figure 15 shows the Modified RAO (TF) when Equation (26) is applied. We aslo tested the formula for various wave conditions and two

different floating platforms, such as FPSO and semi-submersible case, and the results are equally satisfactory. This is covered in detail in the later section,

Results and Discussion. The results show substantial improvement (overestimation does not occur) when the proposed modified motion TF is applied to the FPSO, as shown in Figure 16.

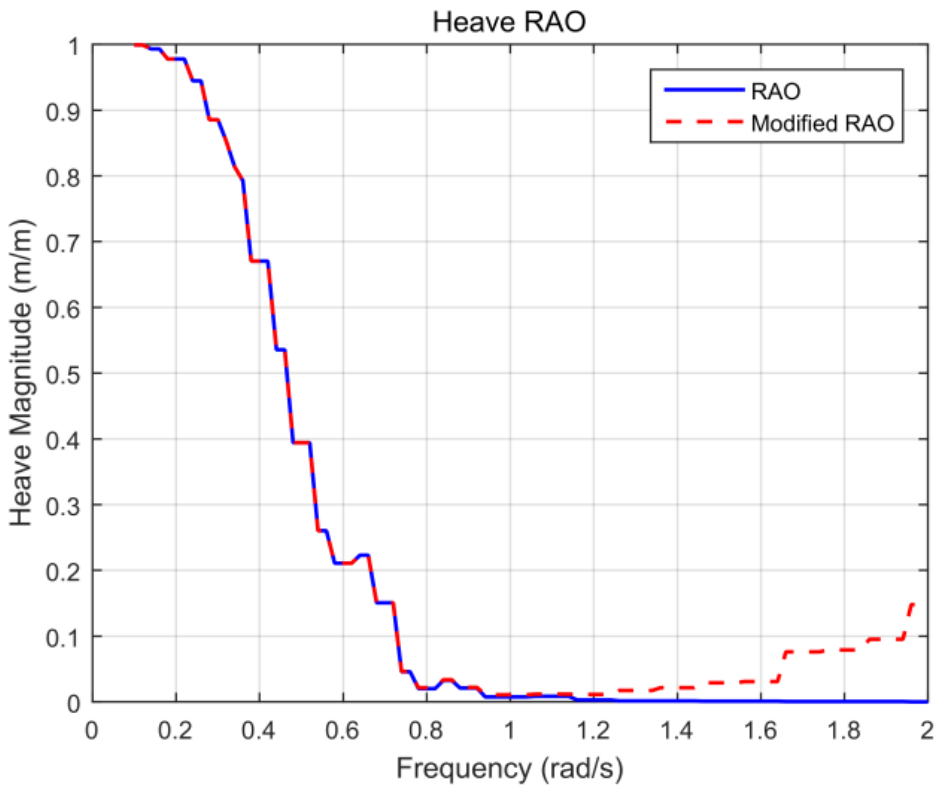

Figure 15 Modified Heave Response Amplitude Operator (RAO) (Red Dotted Line) of FPSO.

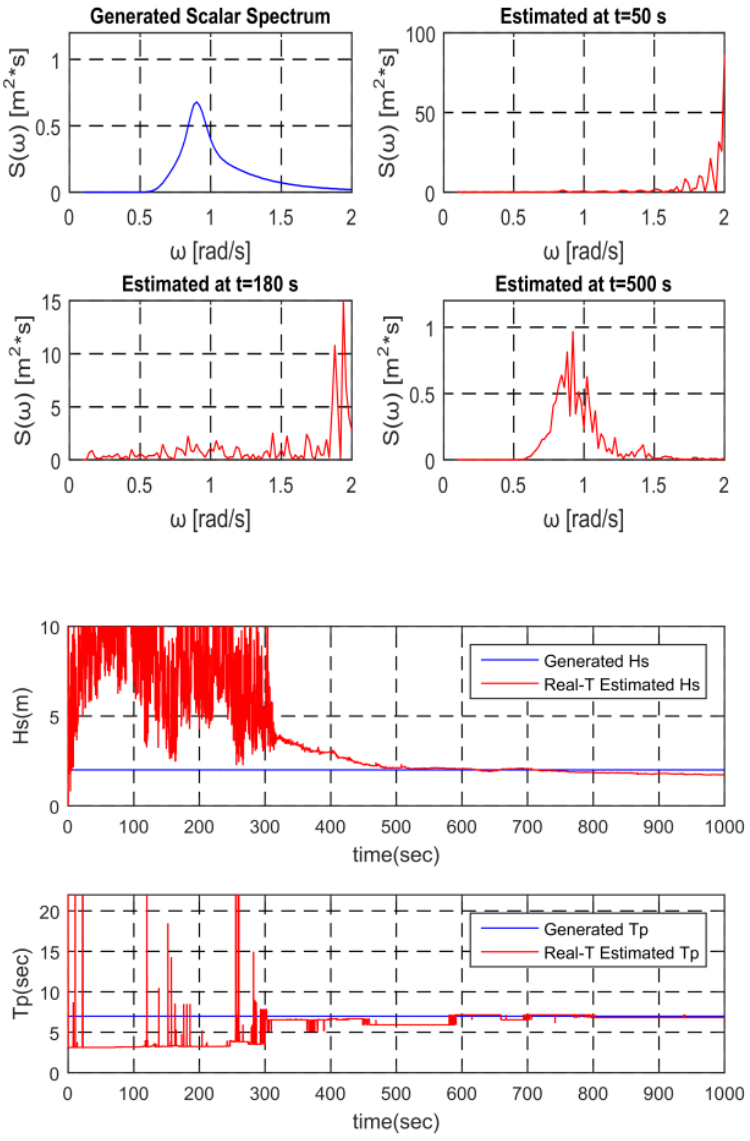

Figure 16 Generated and Estimated Spectrum / Evolution of Parameters Using Modified TF (Hs = 2 m, Tp = 7 s, Frequency: 0.1~2.0 rad/s).

$(x_{2j-1} + ix_{2j})$ is an incoming wave of a complex number in Equation (10). For the two states x_{2j-1}, x_{2j} estimated by the Kalman filter, if Equation (17) is used, the real-time estimation of the corresponding wave elevation (actual wave profile) at each time is

conducted (Figure 17) and Figure 18 shows the results. The real-time wave profile that was estimated by the Kalman filter is compared to the theoretically reconstructed wave profile by using the random phase and the relation between the wave and motion via the phase of transfer function.

Figure 17 describes the estimation process for wave elevation. In the case of the wave spectrum estimation, only the motion time series of the ship needs to be generated through the process of ①, ② in the figure. In the case of the wave elevation estimation, we need to additionally generate the original wave elevation through the ③ calculation. This becomes the target for comparison with the estimated one. It should be noted that the motion and wave random pahses differ by the TF phase φ, so that the random phases of incident wave can be assigned.

In Figure 18, the original and inversely estimated wave profile agree very well. This means the the present Kalman filter technique applied to the inverse problem successfully reproduces not only the real-time wave spectrum, but also the real-time wave elevation. The latter is very important for the active control in many ocean-engineering applications. To the best knowledge of authors, the real-time inverse estimation of wave elevation by the Kalman filter cannot be found in the open literature. In (Pascoal et al., 2017; Pascoal and Soares, 2008; Pascoal and Soares, 2009; Pascoal et al., 2007), no time series of wave elevation was obtained although wave spectra were inversely estimated.

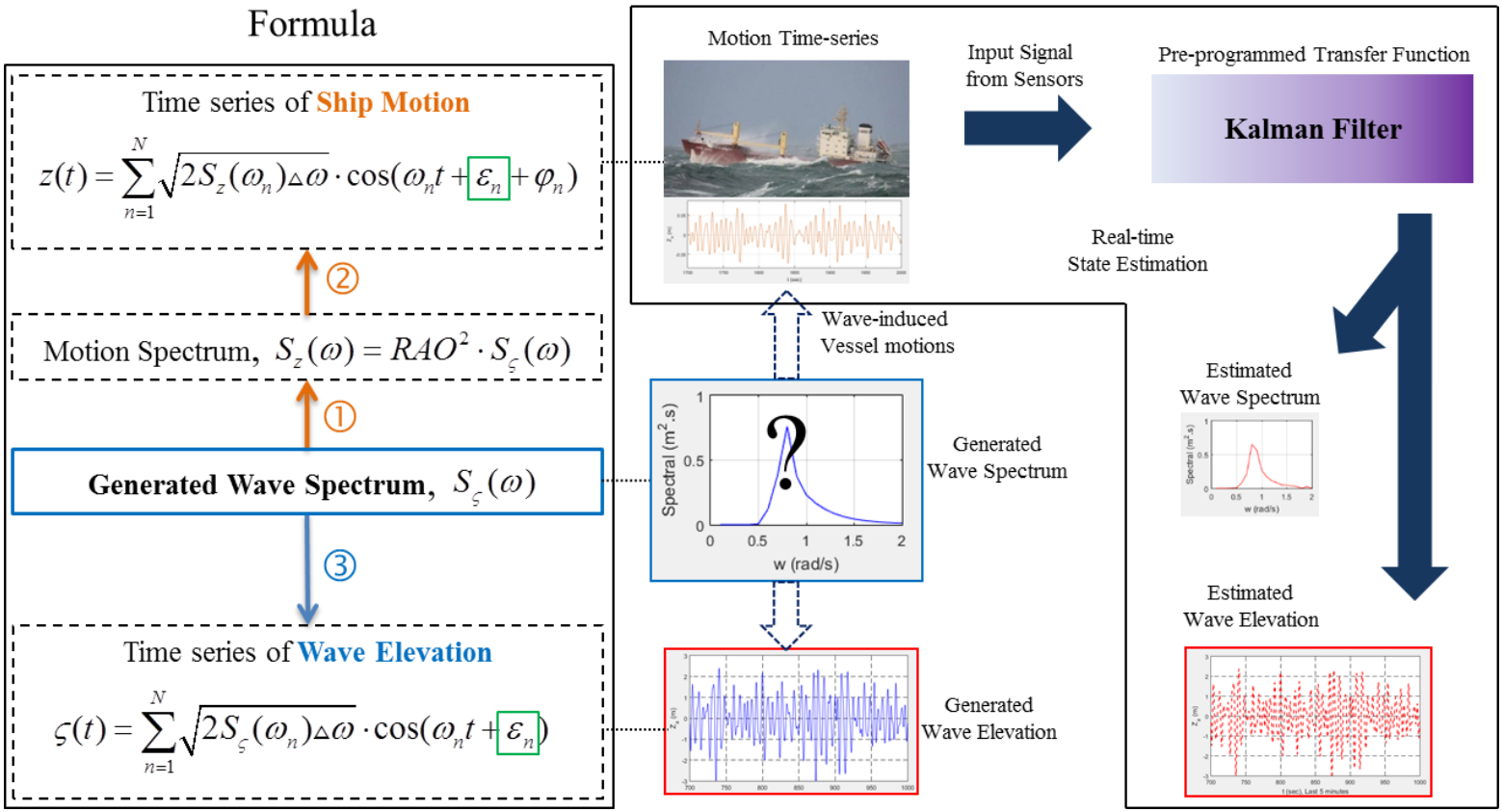

Figure 17 Wave Elevation Estimation Process Using Kalman Filter and Formula.

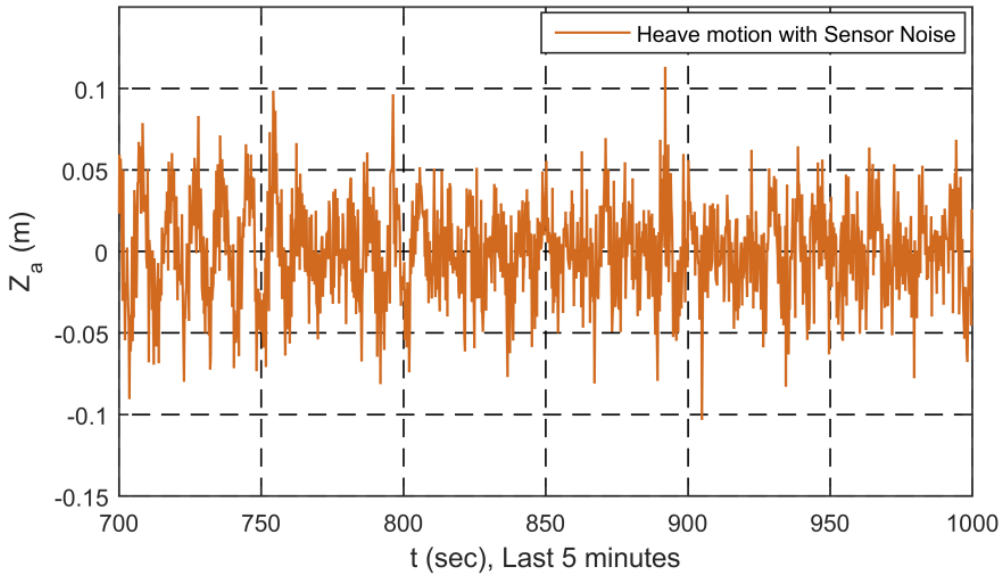

(**a**) Input heave motion.

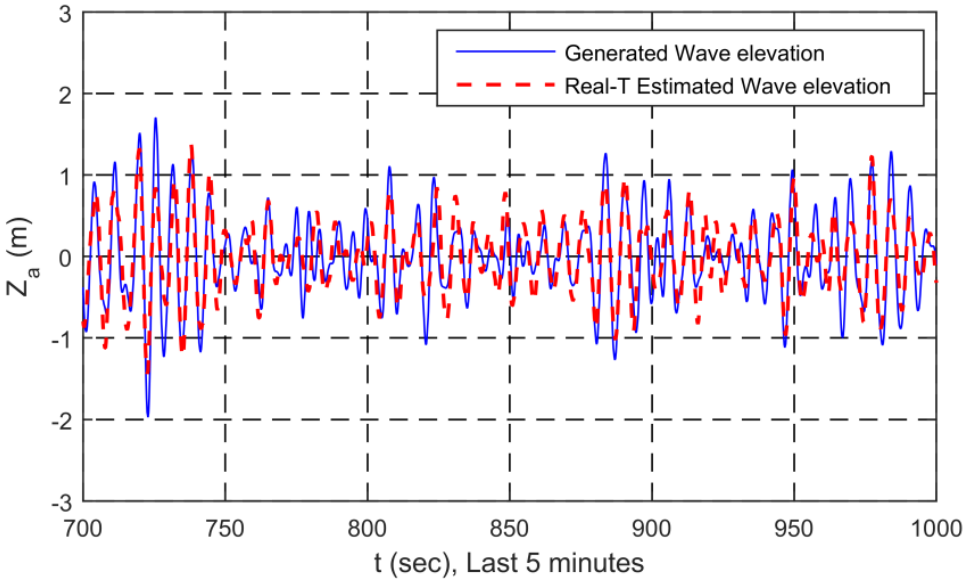

(**b**) Estimated wave elevation.

Figure 18 Input Heave Motion & Estimated Wave Elevation Using Modified TF (Hs = 2 m, Tp = 7 s, Frequency: 0.1~2.0 rad/s).

For further checking of convergence, RMSE of P is represented from Equation (27). The ‘trace’ means sum of diagonal elements. Figure 19 confirms that P does not diverge.

$$RMSE\ of\ \ P = \sqrt{trace(P)} \tag{27}$$

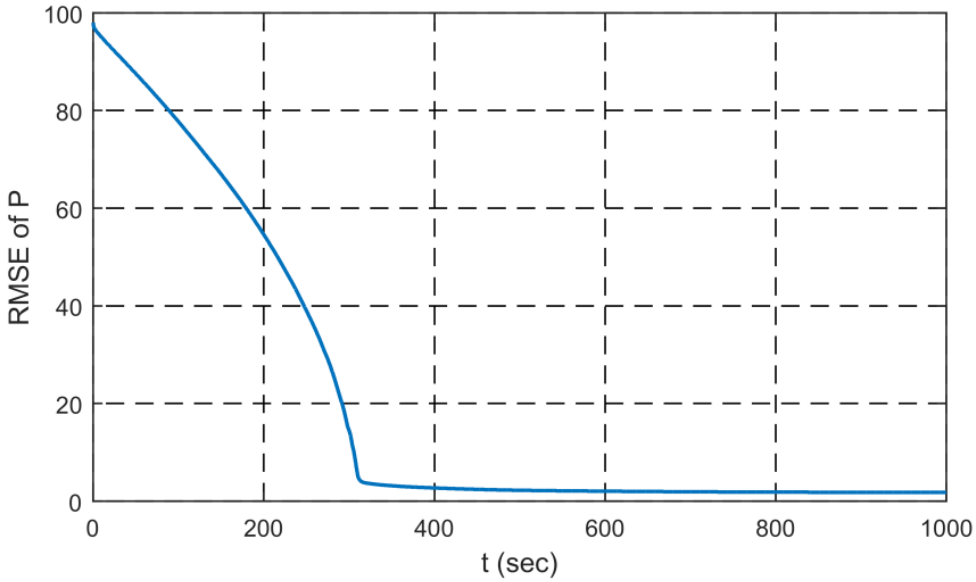

Figure 19 Evolution of P.

The variations of the internal variables P and K in the frequency domain were examined as well in Figure 20. When compared with the ‘~2.0 rad/s’ case of Figure 9(c) and (d), it can be seen that both P and K converge near zero in the high frequency range at 500 s. The application of Modified TF suppresses K in the high frequency.

Consequently, the overestimation of x does not occur in the high-frequency region when it is calculated by Equation (6).

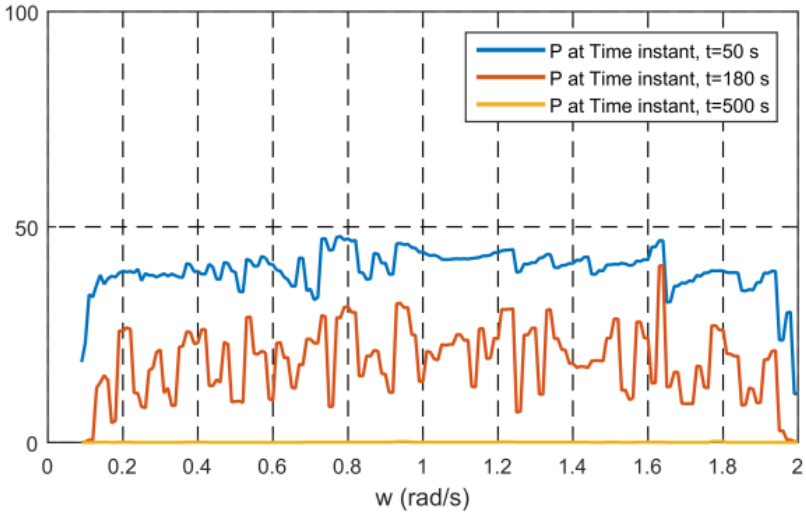

(a) P (to 2.0 rad/s)

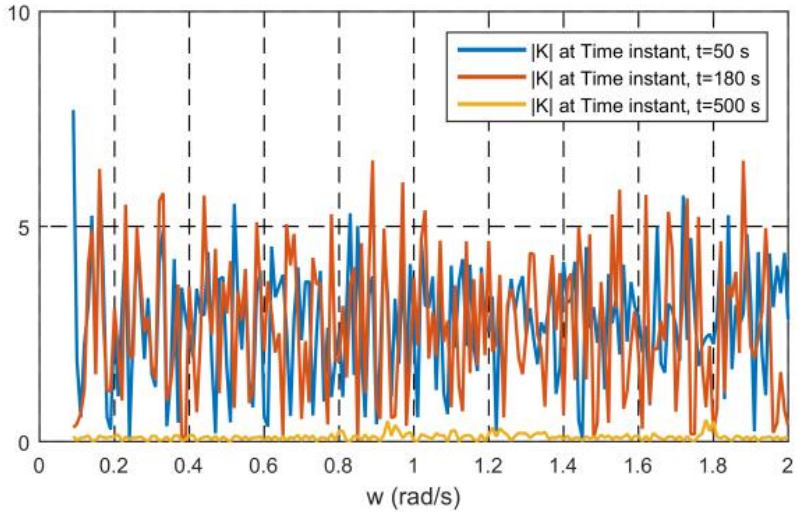

(b) K (to 2.0 rad/s)

Figure 20 Error Covariance and Kalman Gain when Using Modified TF.

The measurements from a sensor include sensor error. When the sensor maker provides sensor error information, we can set a reference value for R according to the information. However, a potential problem is that the statistical properties of sensor errors are not the same during actual measurements. Accordingly, Liu (1998) proposed an adaptive Kalman filter for harmonic signals. Therefore, to take advantage of the adaptive R, Equation (14), e.g., Pascoal and Soares (2009) is applied with the modified TF in subsequent tests. In the equation, only the diagonal component was taken from the covariance matrix for the errors. By two 'diag' processes, we can construct a diagonal matrix, so that it matches the dimensions of the $H_k P_{\bar{k}} H_k^{'}$ matrix.

To explain more about the dimensions of the $H_k P_{\bar{k}} H_k^{'}$ matrix, variable definition and dimensions are in Table 1. The number of states x and measurements z are independent. However, the dimension of matrix ϕ, H, P, R, etc. are determined by the x and z (Rhudy et al., 2017). Subsequently, the dimension of $H_k P_{\bar{k}} H_k^{'}$ in Equation (14) becomes $n_z \times n_z$. The dimension of $E[z_k - H_k \hat{x}_{\bar{k}},\ (z_k - H_k \hat{x}_{\bar{k}})^{'}]$ is also $n_z \times n_z$. Here, if we only take a 'diag' once to the matrix, it becomes a vector and it cannot be computed with $H_k P_{\bar{k}} H_k^{'}$ matrix. Accordingly, 'diag' is taken one more time to convert the vector back into a matrix, so that it can be computed.

Table 1 Dimension of Variables.

Variable	Description	Dimension
x	State Vector	$n_x \times 1$
z	Measurement Vector	$n_z \times 1$
ϕ	State Transition Matrix	$n_x \times n_x$
H	Output Matrix	$n_z \times n_x$
P	Error Covariance Matrix	$n_x \times n_x$
R	Measurement Error Covariance Matrix	$n_z \times n_z$

Applying Modified TF with Adaptive R also suppressed the overestimation, and the test results are given in the next section.

Testing

Numerical Modeling of Motion Sensor

Only heave-motion signal at the center of gravity (CG) of FPSO was used. Time domain simulation software, such as CHARM3D, can be used to get the ship's motion (Jin and Kim, 2018). However, in this paper, the motion data is generated by superposition for the testing i.e., they are generated from the motion spectrum by Equations (28) and (29). The wave spectrum was assumed to be single-peaked and narrow-banded. The data sampling frequency is 5 Hz.

$$S_z(\omega) = RAO^2 \cdot S_\varsigma(\omega) \tag{28}$$

$$Z(t) = \sum_{n=1}^{N} \sqrt{2S_z(\omega_n)\triangle\omega} \cdot \cos(\omega_n t + \varepsilon_n + \varphi_n) \tag{29}$$

where

$S_z(\omega)$: motion spectrum

$S_\varsigma(\omega)$: wave spectrum

z: vessel motion

ω: intrinsic frequency of harmonic

$\triangle\omega$: frequency interval

ε_n: random phase

φ_n: phase of TF

In this paper, the frequency range of 0.1~2.0 with 0.02 rad/s interval is used. Subsequently, the number of entry frequencies is 96 and the number of states to be obtained from the filter is 192. It was compared to the cases with different $\Delta\omega$ to investigate the relationship between frequency intervals and estimation performance. Figure 21 shows that the real-time estimated wave spectra reasonably match, regardless of the two employed frequency intervals.

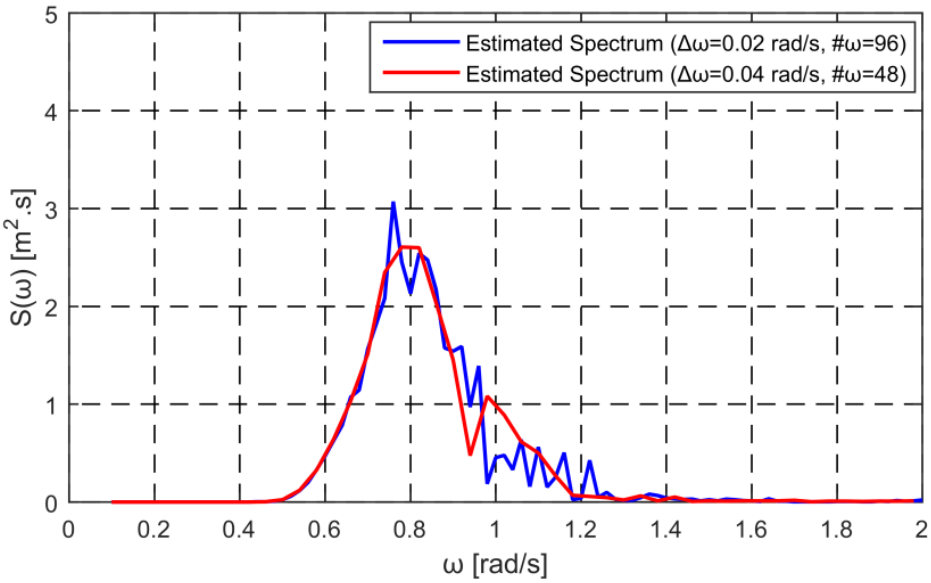

Figure 21 Comparison of Estimated Spectra Averaged over 700~1000 s for the Different Number of Frequency Components.

When superposing sinusoidal components, the randomly-perturbed frequency interval $\Delta\omega$ was used by multiplying the random value α, as shown below in order to prevent the signal repetition. The Kalman filter then ran for 1000 s.

$$\Delta\omega = 0.1 \times \alpha \text{ [rad/s]} \ (-0.5 \langle \alpha \langle 0.5) \tag{30}$$

Estimation tests were performed for various sea states to confirm whether the proposed modified TF can be applied to a wide range of applications. In the later part of this section, another vessel (OC4 semisubmersible e.g., Kim and Kim (2015a); (Kim and Kim, 2016)) with different RAO will be tested. The applied Kalman-filter technique equally worked well for the new vessel, which shows that the developed algorithm is not

sensitive to vessel type either. To observe the sensitivity against various wave conditions, a series of sea states applied are shown in Table 2, as below. In this table, No. 1 to 5 cases were selected as reasonable sea states (DNV, 2000). On the other hand, No. 6 and 7 cases are particular sea states.

Table 2 Simulated Sea States and Their Parameters.

Sea State No.	Hs (m)	Tp (s)
1	1.5	6
2	5	9
3	9	11
4	13	13
5	17	15
6	1.5	18
7	13	11

Results and Discussion

Figure 22–Figure 28 present the results of the inversely estimated real-time spectra, Hs and Tp with time for the seven sea states when applying the proposed modified TF and adaptive R (Equation (14)) of Pascoal and Soares (2009). It is seen that the developed Kalman filter technique works well for various sea states, which opens the door to a continuous inverse estimation of ocean waves from heave-motion sensor, regardless of sea states during service or voyage without adjusting the wave-frequency range and Kalman-filter parameters.

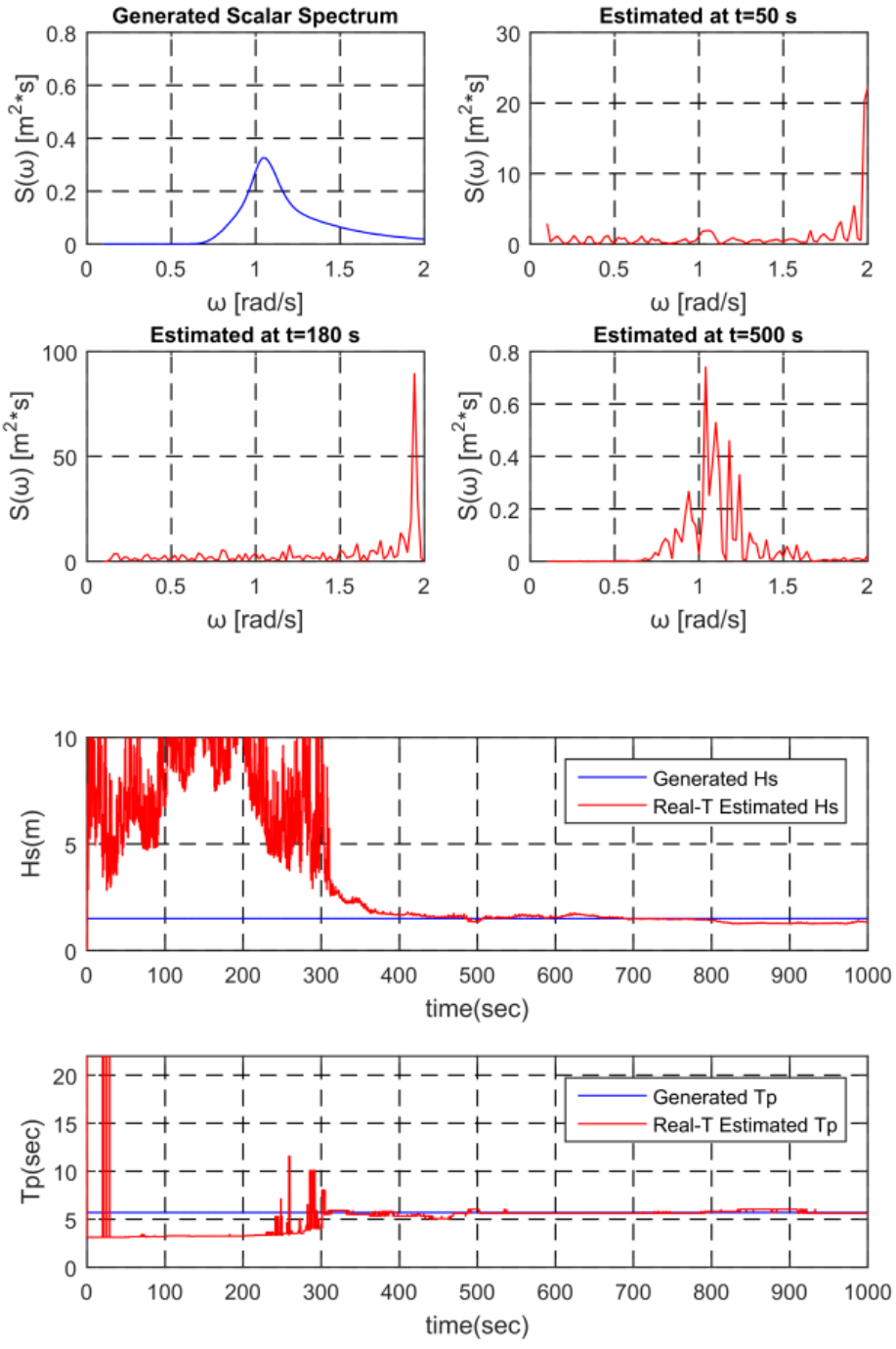

Figure 22 Generated and Estimated Spectrum / Evolution of Parameters (Sea State 1, Hs = 1.5 m, Tp = 6 s).

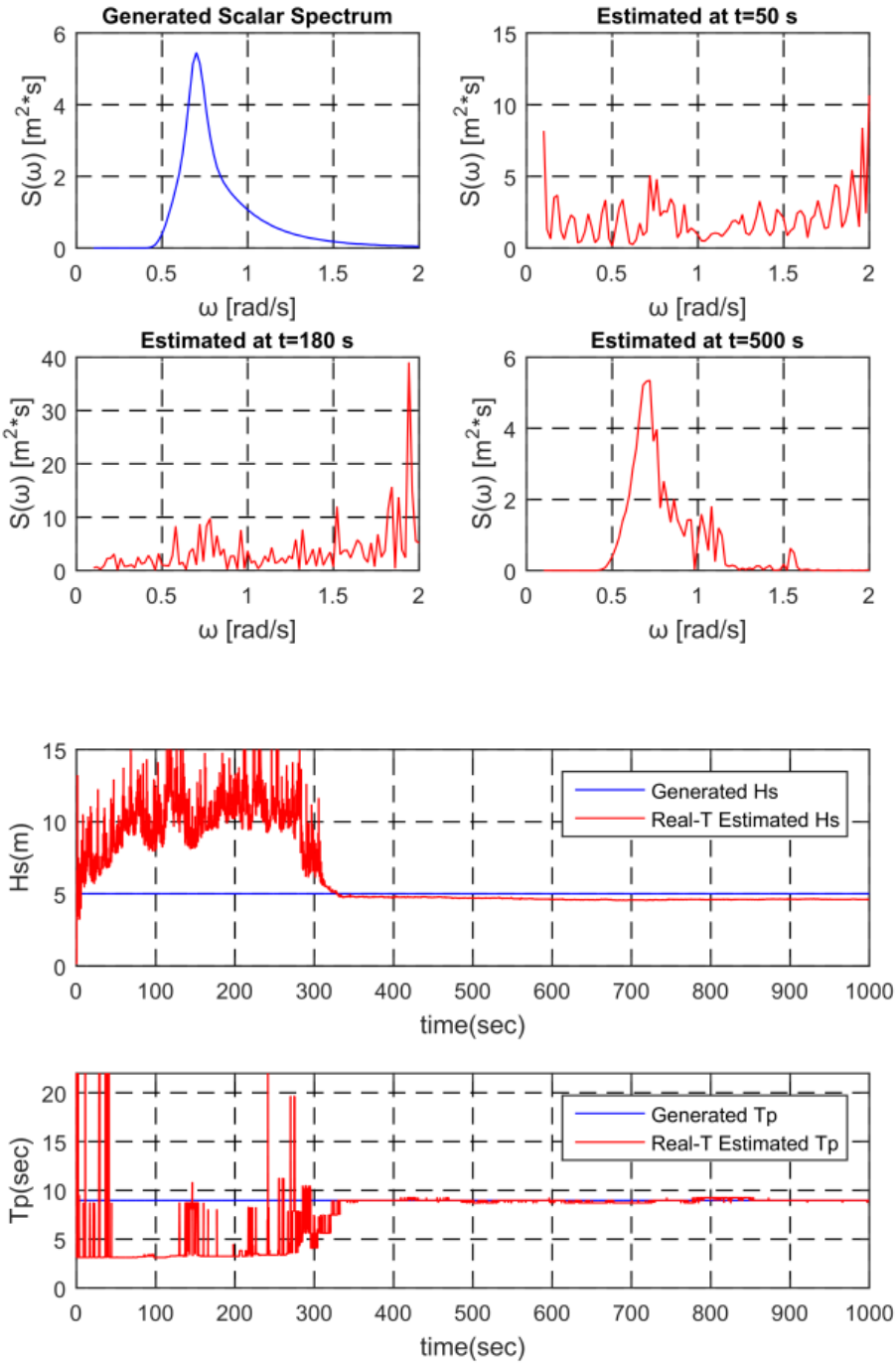

Figure 23 Generated and Estimated Spectrum / Evolution of Parameters (Sea State 2, Hs = 5 m, Tp = 9 s).

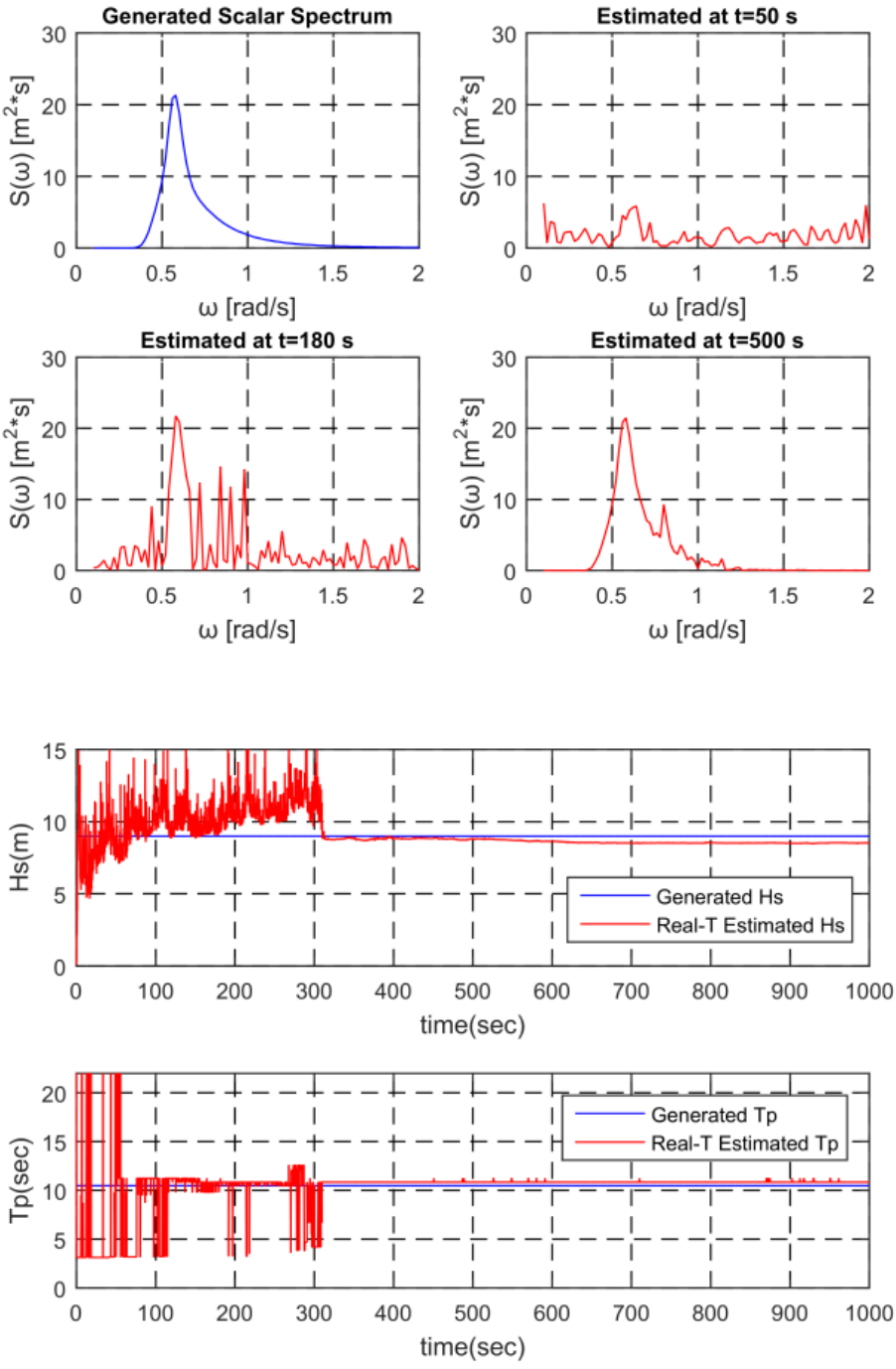

Figure 24 Generated and Estimated Spectrum / Evolution of Parameters (Sea State 3, Hs = 9 m, Tp = 11 s).

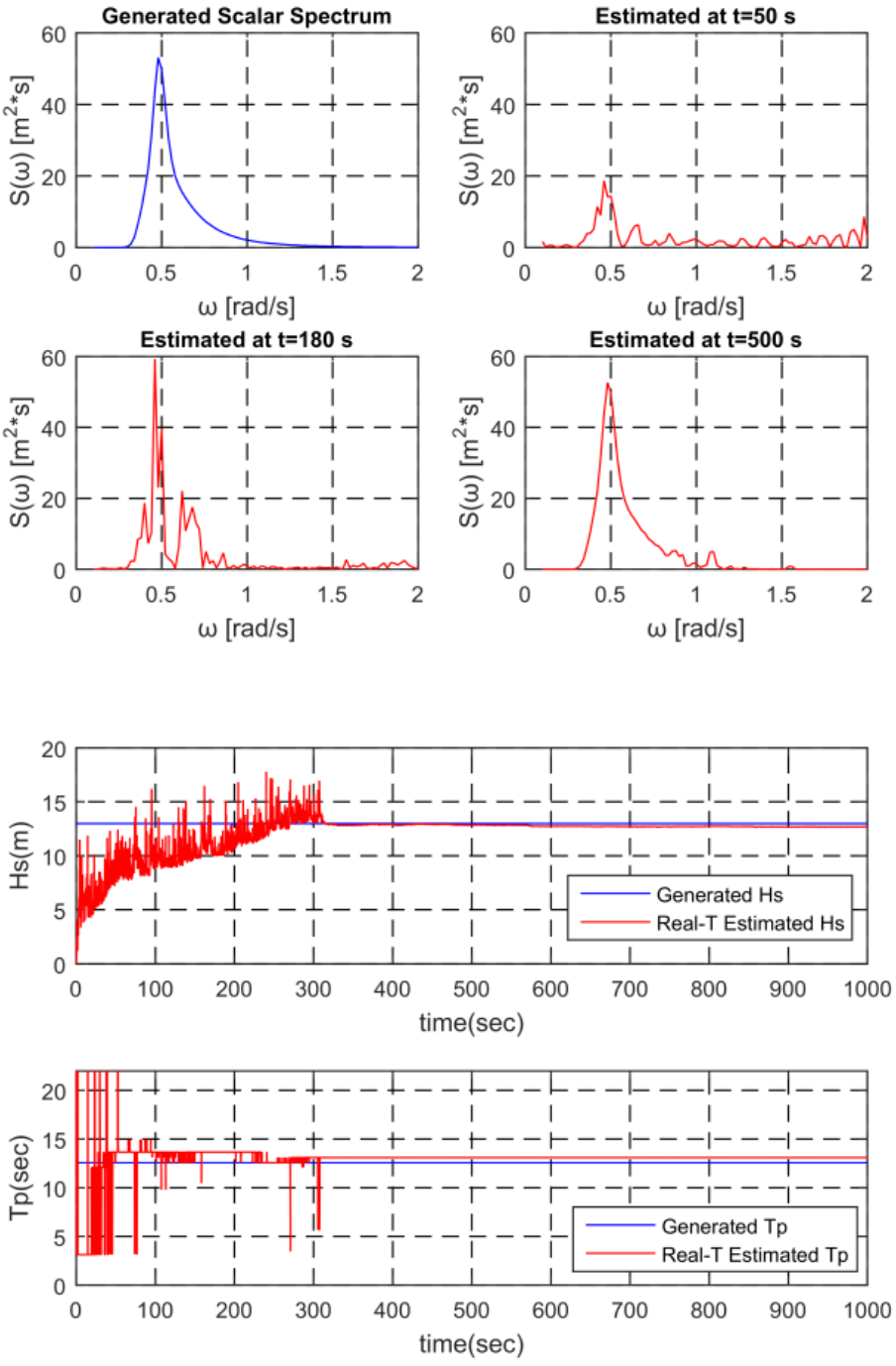

Figure 25 Generated and Estimated Spectrum / Evolution of Parameters (Sea State 4, Hs = 13 m, Tp = 13 s).

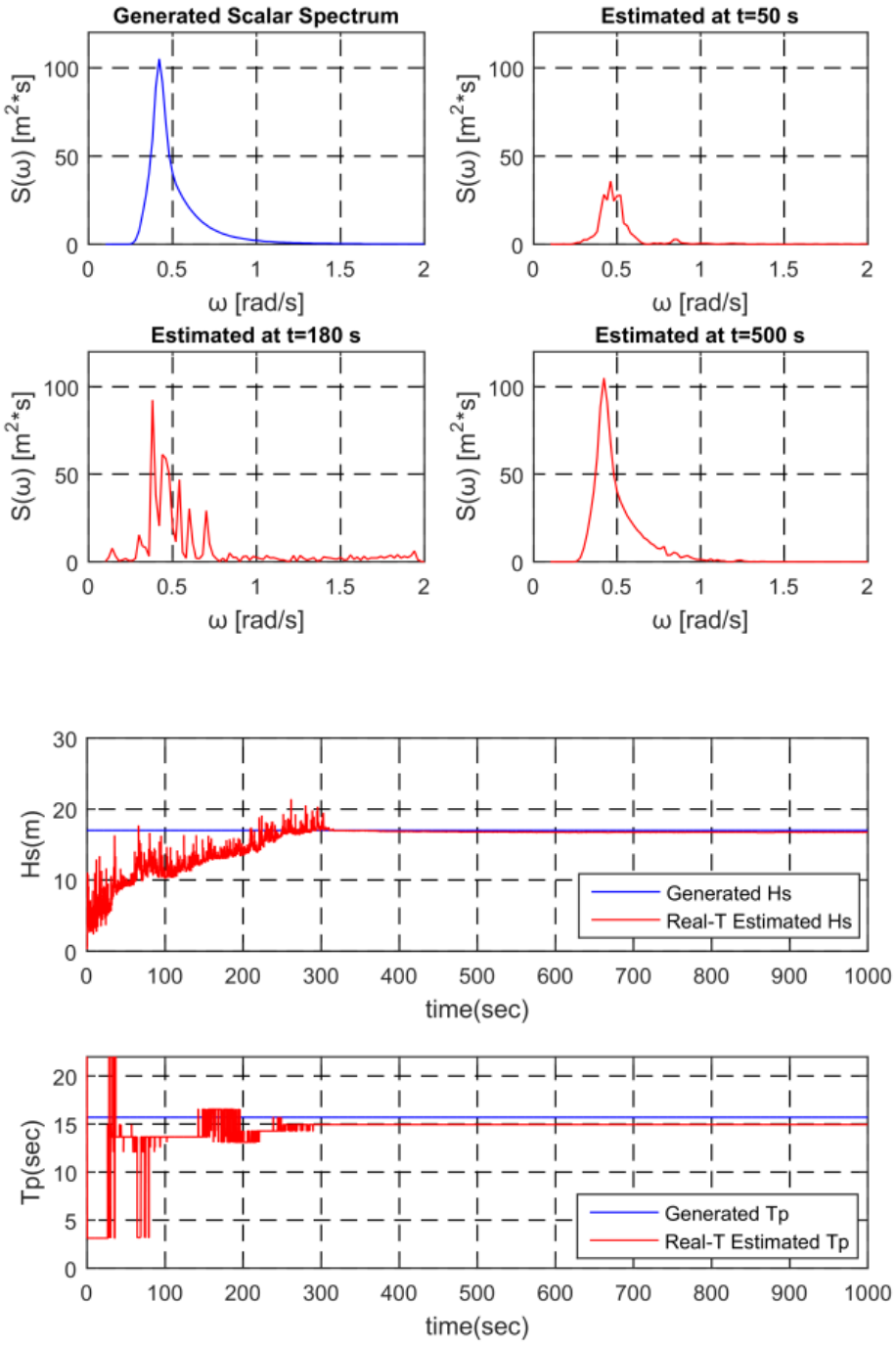

Figure 26 Generated and Estimated Spectrum / Evolution of Parameters (Sea State 5, Hs = 17 m, Tp = 15 s).

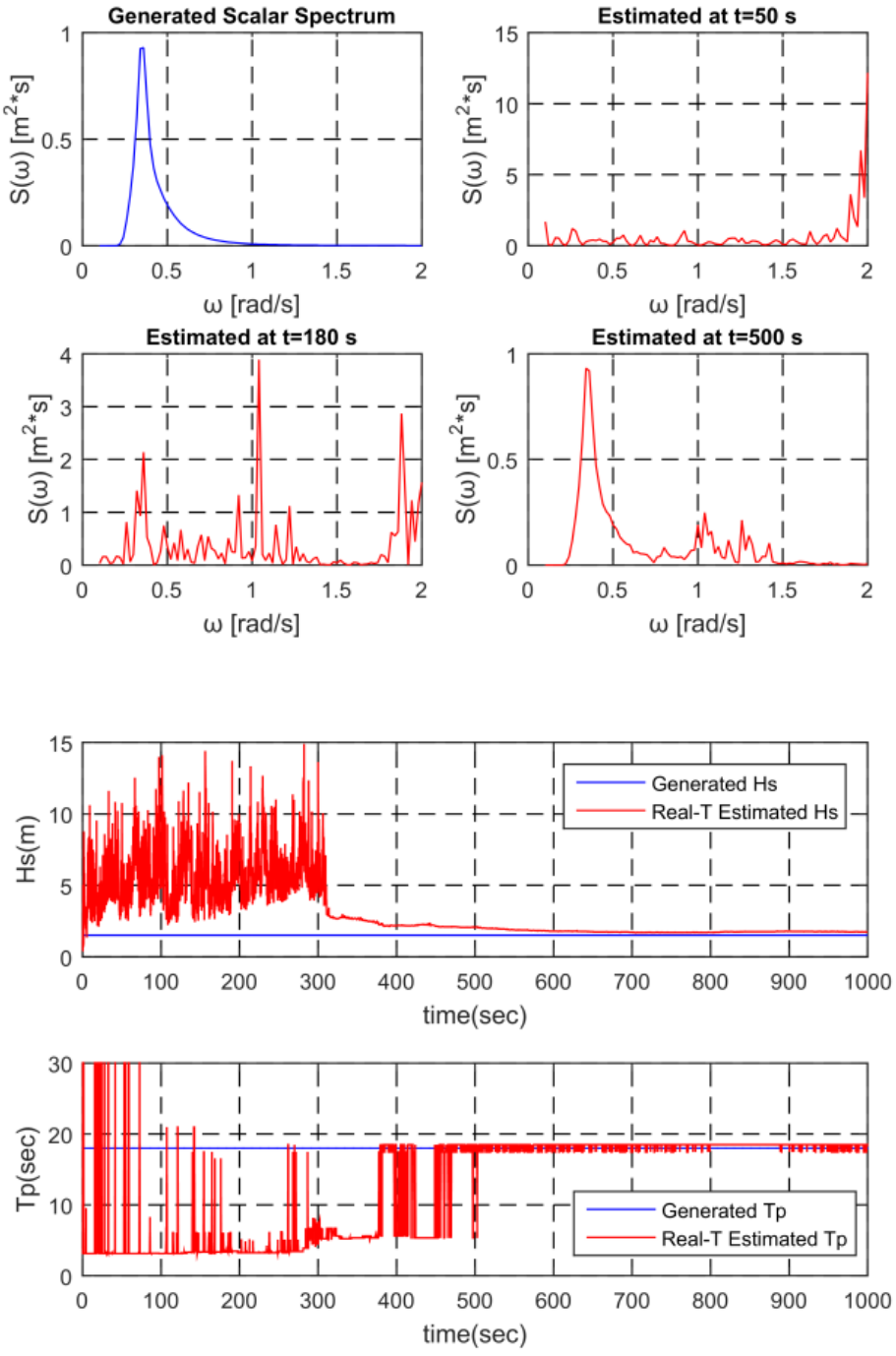

Figure 27 Generated and Estimated Spectrum / Evolution of Parameters (Sea State 6, Hs = 1.5 m, Tp = 18 s).

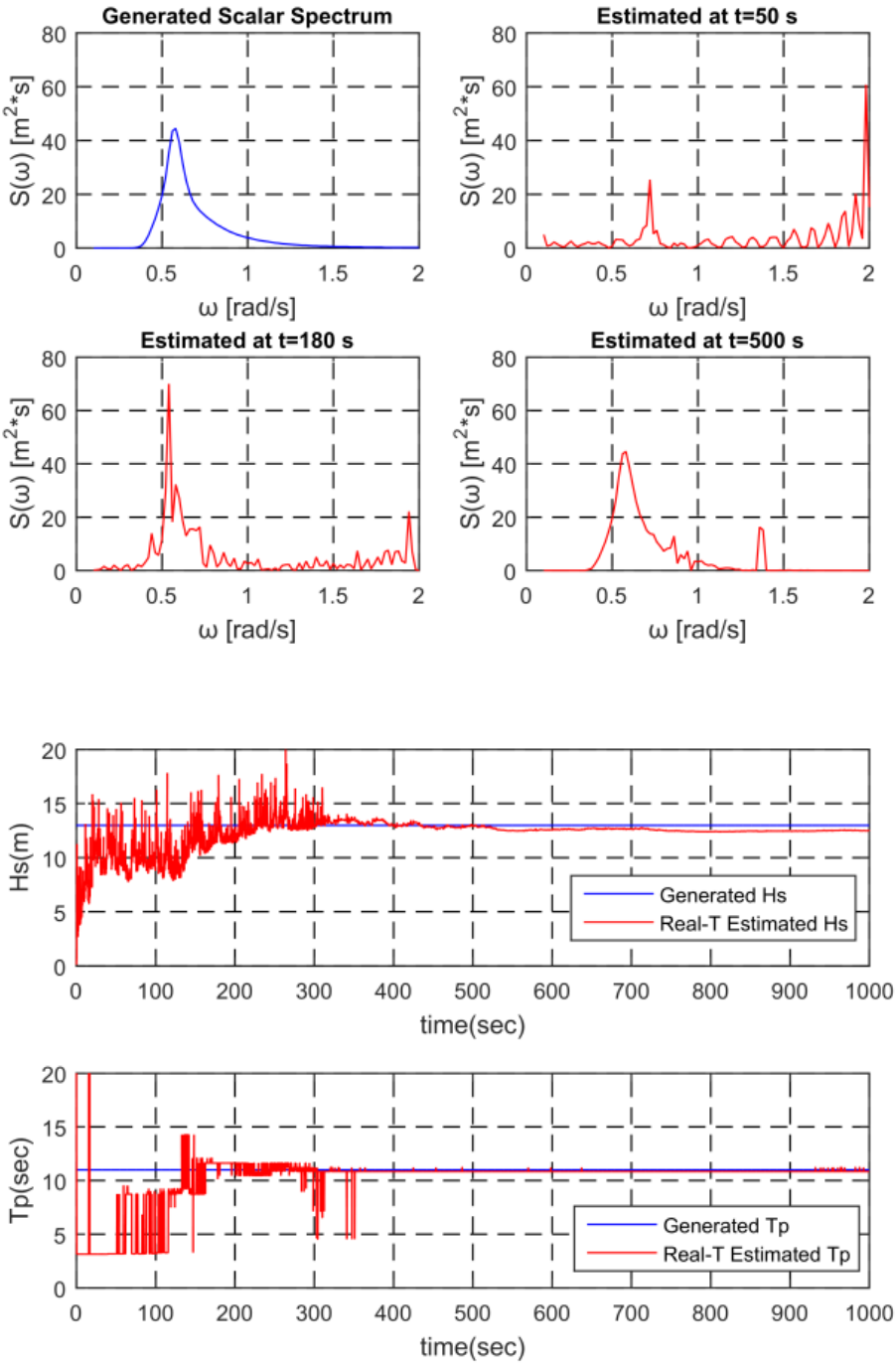

Figure 28 Generated and Estimated Spectrum / Evolution of Parameters (Sea State 7, Hs = 13 m, Tp = 11 s).

Next, we tested the developed modified Kalman-filter algorithm for another vessel (OC4 semisubmersible) to see whether the developed algorithms are sensitive to vessel types. In this regard, Figure 29 provide the motion TF of OC4 semisubmersible (Kim and Kim, 2015a, 2016). Sea state No. 1, 3, and 5 were tested (Figure 30–Figure 32) for the OC4. The estimation of real-time wave spectra, Hs, and Tp was good.

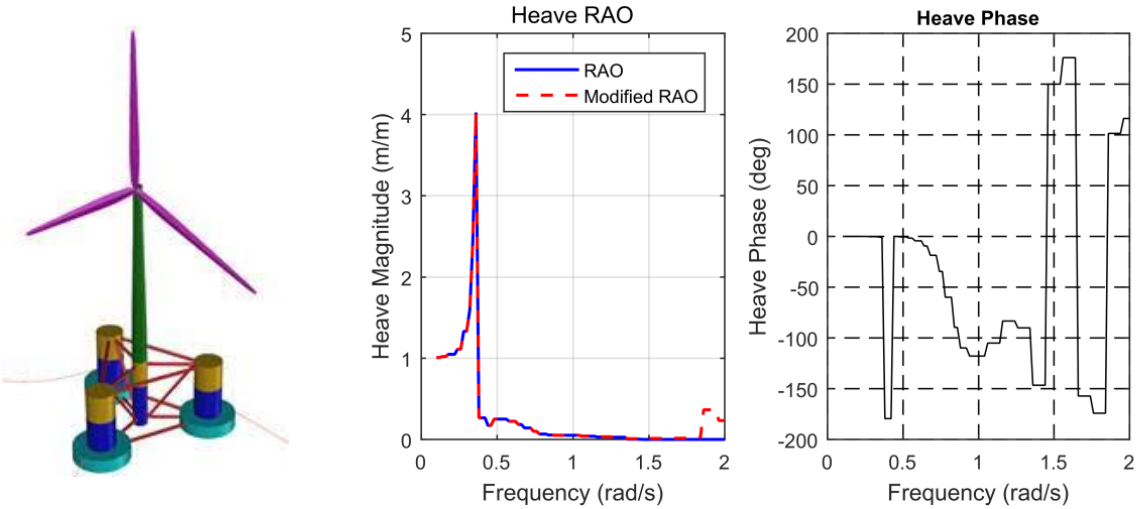

Figure 29 Model and Modified Transfer Function of OC4.

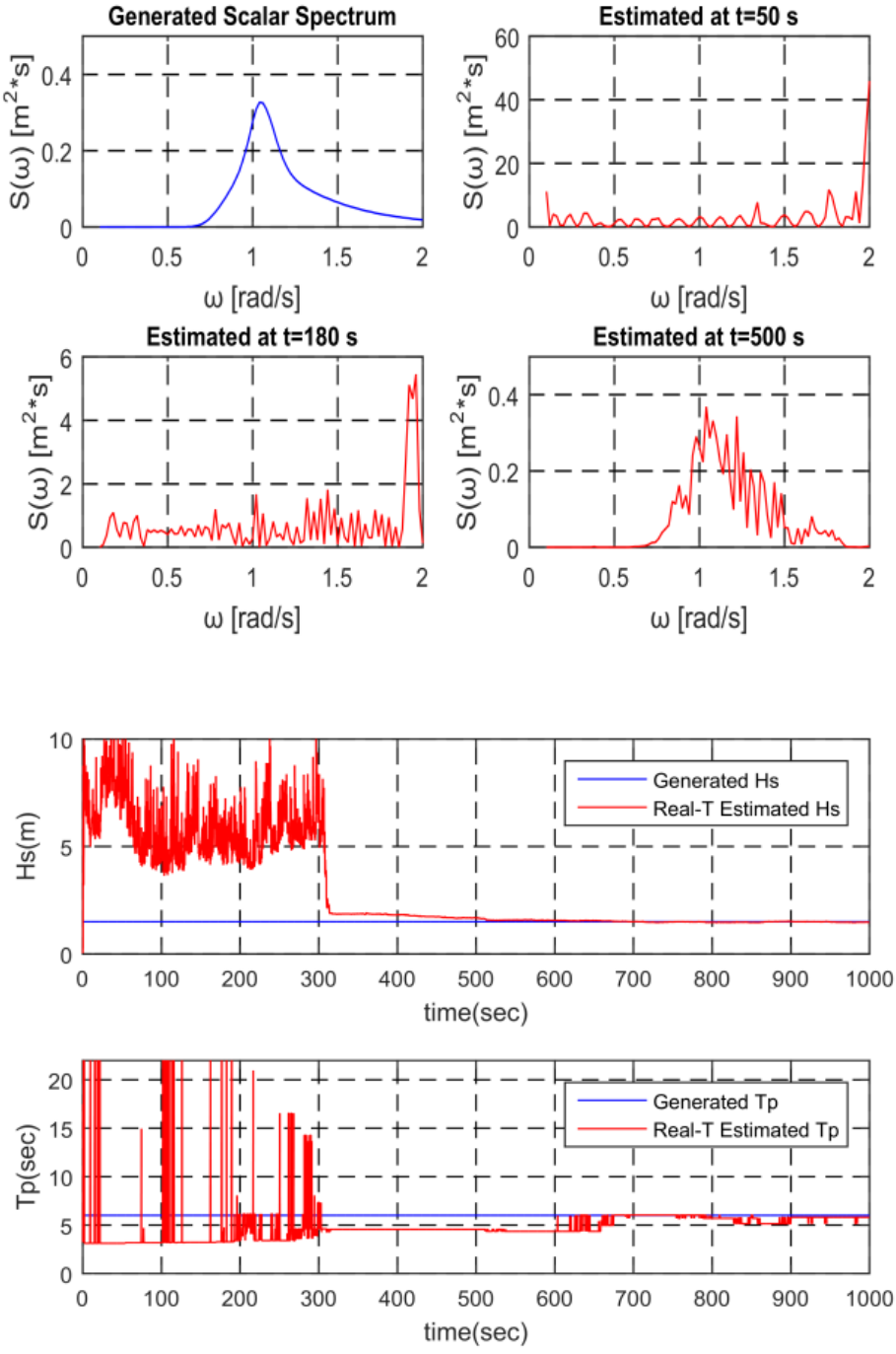

Figure 30 Generated and Estimated Spectrum / Evolution of Parameters (Sea State 1, Hs = 1.5 m, Tp = 6 s).

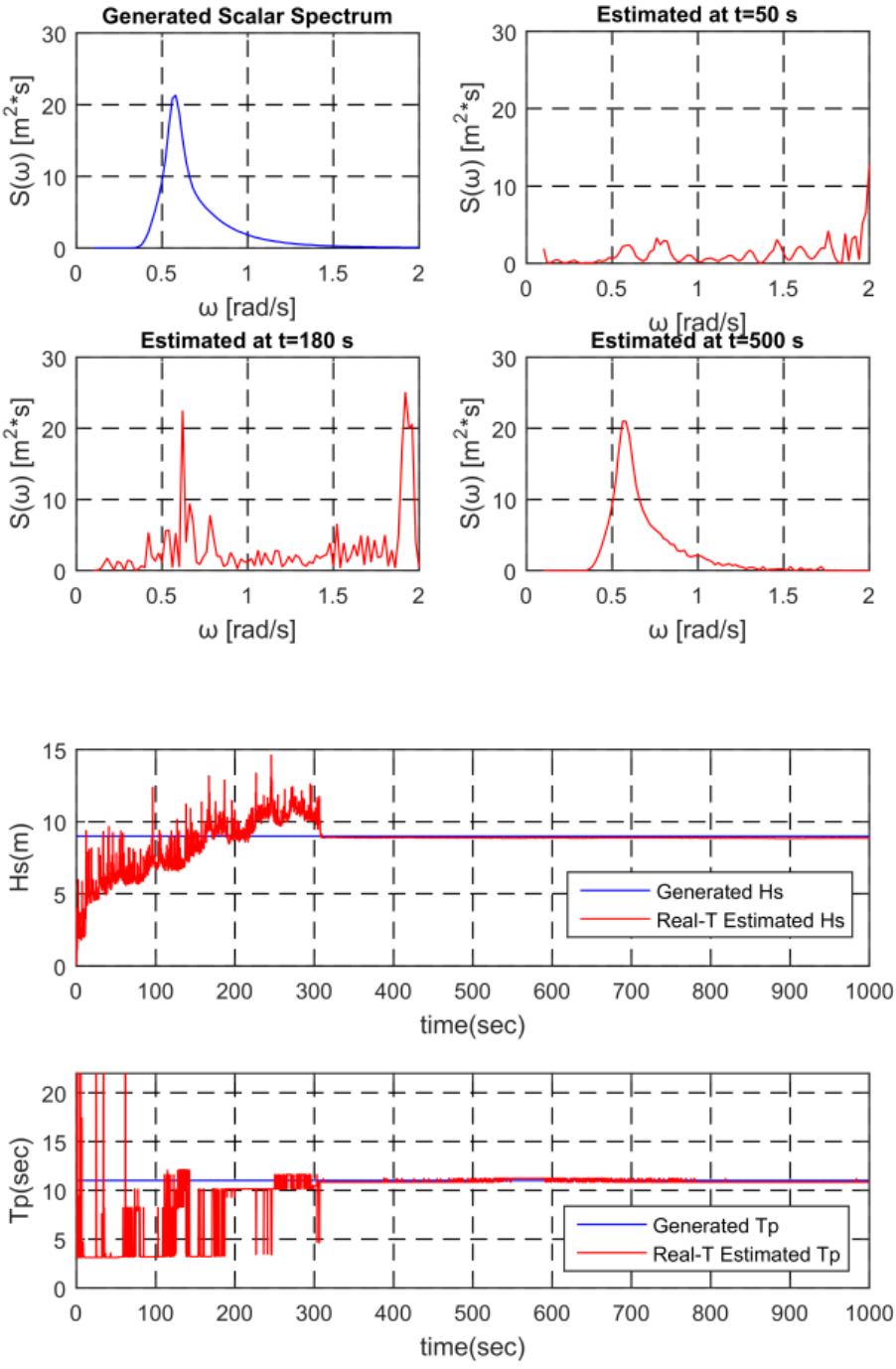

Figure 31 Generated and Estimated Spectrum / Evolution of Parameters (Sea State 3, Hs = 9 m, Tp = 11 s).

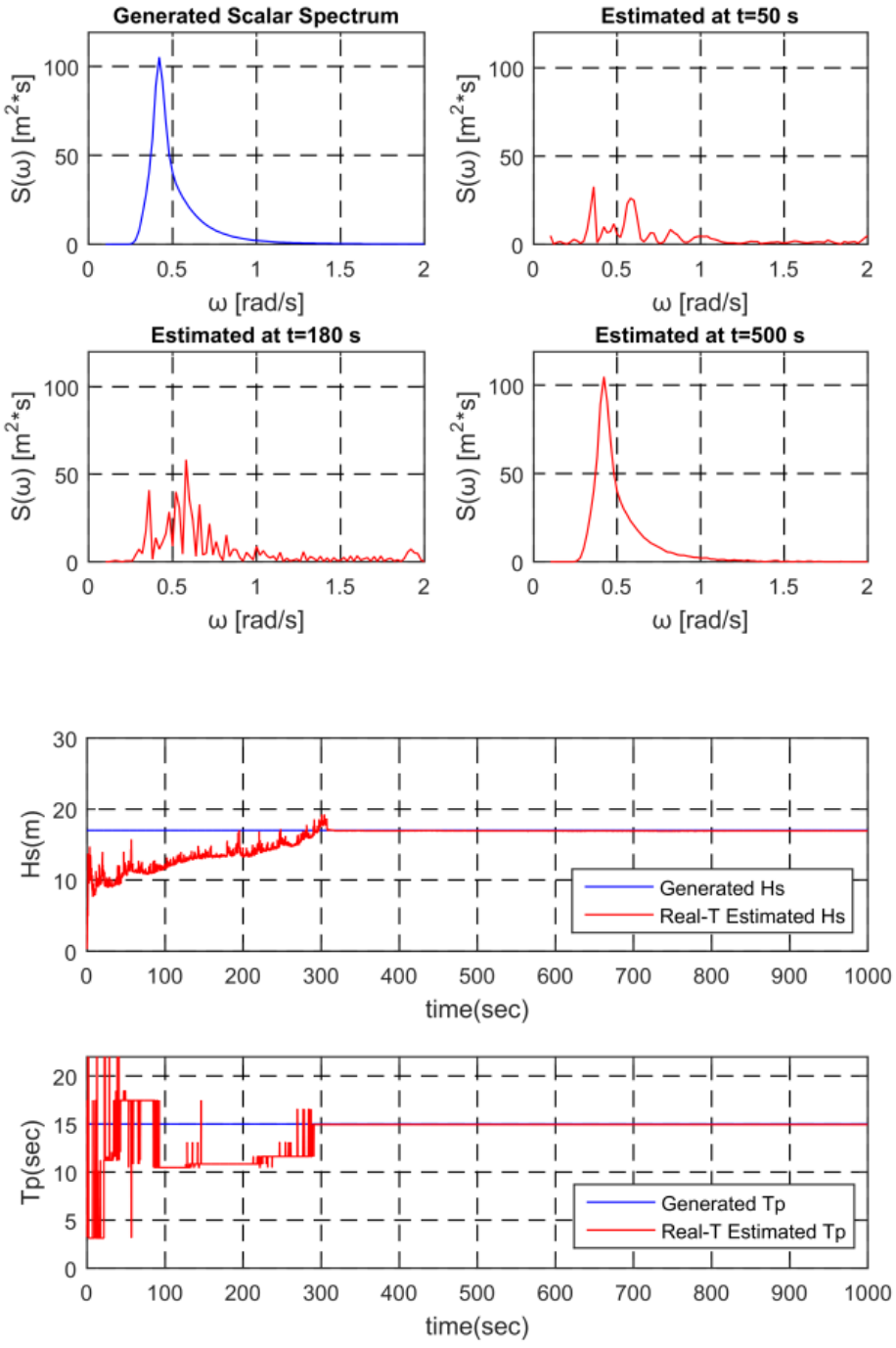

Figure 32 Generated and Estimated Spectrum / Evolution of Parameters (Sea State 5, Hs = 17 m, Tp = 15 s).

Up to this point, the developed Kalman-filter algorithm has been applied to the stationary sea state. However, sea states continue to change in actual sea, so, it is of interest to inversely estimate waves for non-stationary seas. The sea state sequence is set as shown in Table 3. It is assumed that the sea state is changing accordingly. The sensor error's standard deviation was set as 2.3 cm and the modified TF was applied to the FPSO. Simulation was performed assuming that the vessel's motion continuously varies due to the changes in sea state. The superposed motion time series for each sea state were then connected in order (Figure 33).

Table 3 Simulated Sea State Sequence Along the Route.

Sequence	No. 1	No. 2	No. 3	No. 4	No. 5
Hs (m)	3	2	4	8	13
Tp (s)	9	8	10	11	11

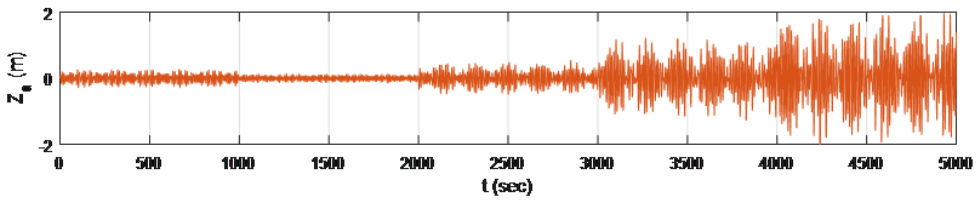

Figure 33 Time Series of Heave Motion During Sea State Change.

The algorithm was tested while using both modified TF and adaptive R. As a result (Figure 34), the real-time wave spectra are well estimated, even with drastic changes in sea states. Figure 34(b) shows the change in R and Q (fixed) during the estimation and Figure 35 is the RMSE of P, which is converging with more measurements.

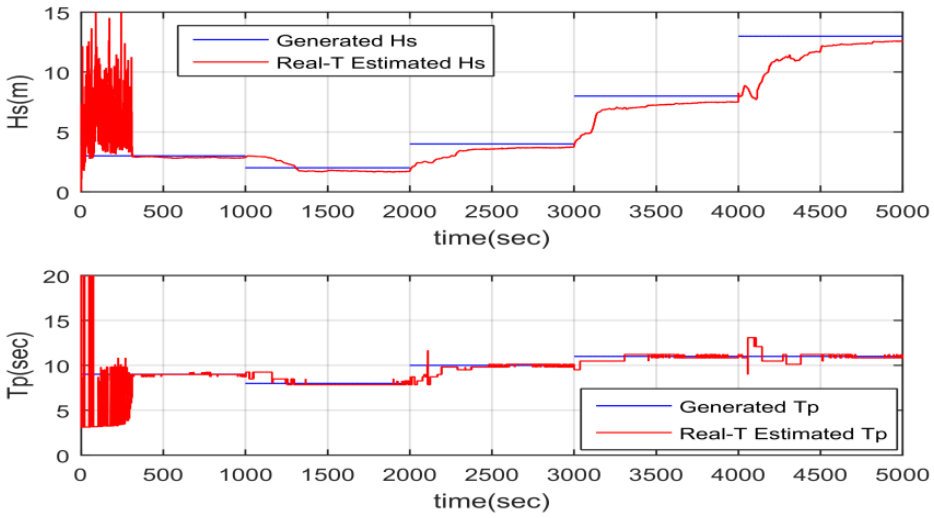

(a) Hs & Tp

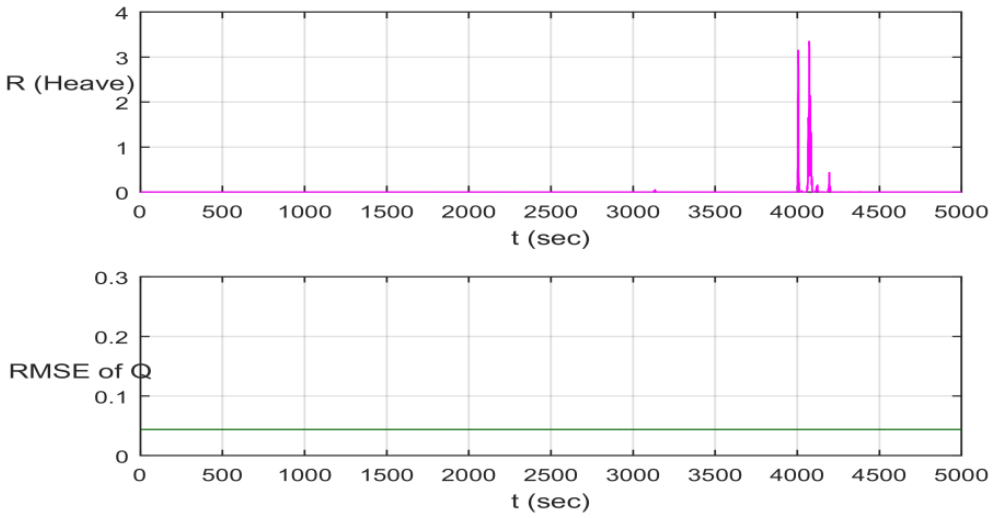

(b) R & Q

Figure 34 Evolution of Parameters, R (Adaptive) and Q (Fixed) During Sea State Change.

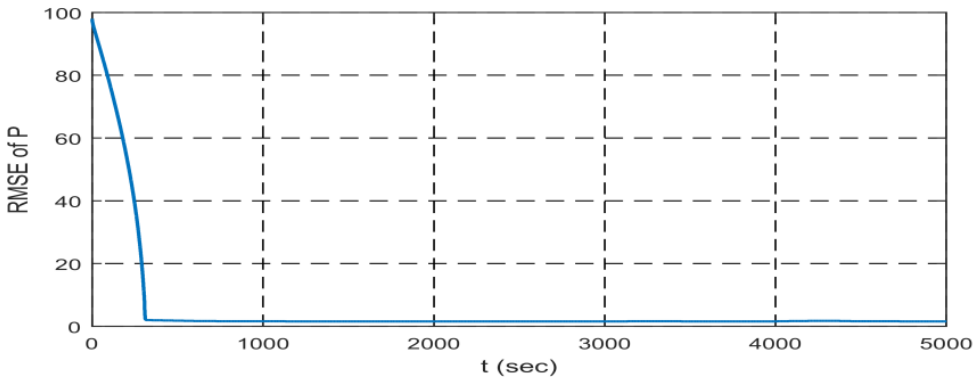

Figure 35 Evolution of P During Sea State Change Using Modified TF and Adaptive R.

Directional Spectrum and Forward Speed Inclusion

Directional Spectrum

Previous content has covered the 1d scalar spectrum which assumes that the wave energy is condensed in dominant heading. However, in actual seas, the wave components do not travel in the same direction. The wave energy is distributed along the direction and is incident on the structure. So, here the directional wave spectrum is covered taking into account the spreading factor. When considering the spreading factor s of wave energy, generally ‘cosine 2S spreading function’ as Equation (31) is used. In this case, the directional spectrum is obtained by multiplying the directional spreading function to the 1d scalar spectrum as Equation (32). Since the energy before and after spreading is the same, the integral of the directional spreading function for all directions should be 1 as Equation (33) (Pascoal et al., 2007).

$$D_{\varsigma}(\mu) = \frac{2^{(2s-1)}\, s!(s-1)!}{\pi(2s-1)!}\cos^{2s}(\mu - \bar{\mu}) \qquad \text{with} \qquad |\mu - \bar{\mu}| < \frac{\pi}{2} \tag{31}$$

$$S_{\varsigma}(\omega, \mu) = D_{\varsigma}(\mu) \cdot S_{\varsigma}(\omega) \tag{32}$$

$$\int_{-\pi}^{\pi} D_{\varsigma}(\mu)\, \mathrm{d}\mu = 1 \tag{33}$$

where

$D_{\varsigma}(\mu)$: directional spreading function

s : spreading factor

$\bar{\mu}$: mean direction of wave propagation

$S_{\varsigma}(\omega, \mu)$: wave directional spectrum

$S_{\varsigma}(\omega)$: wave 1d scalar spectrum

The figure below shows a directional spectrum when $\bar{\mu}$ is 180 degrees and s is 2. The larger s is, the narrower the spreading is.

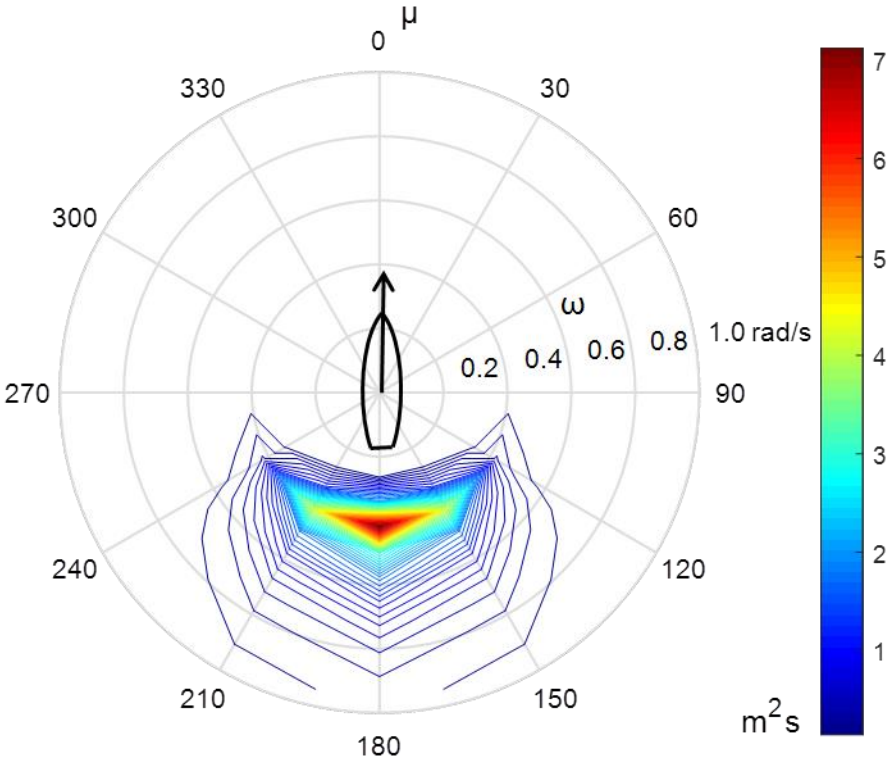

Figure 36 Cosine 2S Spreading.

The mathematical formula of generated directional wave and ship's motion spectrum as follows.

$$\varsigma_m(t) = \sum_{j=1}^{n_f} \tilde{\varsigma}_{jm} \cos(\omega_j t + \varepsilon_j) \tag{34}$$

$$S_{z,jm} = RAO_{jm}{}^2 \cdot S_{\varsigma,jm} \tag{35}$$

where

ς : wave elevation

j : j th frequency

m: m th direction

n_f : number of harmonics to estimate

$\tilde{\varsigma}$: wave amplitude

ε : random phase

S_z : ship' motion spectrum

S_ς : directional wave spectrum

Using the following equations, 6 DOF motion $Z(t)$ was made from the ship's motion spectrum, $S_{z,jm}$.

$$Z(t) = \sum_{m=1}^{n_\theta} \sum_{j=1}^{n_f} \tilde{Z}_{jm} \cdot \cos(\omega_j t + \varepsilon_j + \varphi_{jm})$$
$$Z(t) = \sum_{m=1}^{n_\theta} \sum_{j=1}^{n_f} \sqrt{2S_z(\omega_j, \theta_m) \triangle\omega \triangle\theta} \cdot \cos(\omega_j t + \varepsilon_j + \varphi_{jm}) \quad (36)$$

where

z: ship's motion

n_θ : number of direction in the discretization

$\tilde{Z}$: ship's motion amplitude

φ_n : phase of TF

$\triangle\omega$: frequency interval

$\triangle\theta$: direction interval

Here, the Kalman filter estimates the magnitude of the wave spectrum not only in the dominant direction but in all directions. So, the number of state x is also multiplied by the number of directions. To use more data set as input, we increased the number of motion to 6 DOF. Now because the direction and more motions are added, Equation (10) and (11) become Equation (37) and (38) respectively.

$$z(t) \cong \mathrm{Re}\Big(\sum_{m=1}^{n_\theta} \sum_{j=1}^{n_f} TF_{j,m} \times (x_{2j-1,m} + i x_{2j,m}) \ (\cos(\omega_j t) + i \sin(\omega_j t)) \ \Big) \tag{37}$$

where

z: vessel motion

n_f : number of harmonics to estimate

n_θ : number of direction in the discretization

TF_j : complex-valued transfer function for frequency j, direction m

The matrix type of H becomes

$$H_{jklm} = \begin{bmatrix} \mathrm{Re}(TF_{jlm})\cos(\omega_j k \triangle t) - \mathrm{Im}(TF_{jlm})\sin(\omega_j k \triangle t) \\ -\mathrm{Im}(TF_{jlm})\cos(\omega_j k \triangle t) - \mathrm{Re}(TF_{jlm})\sin(\omega_j k \triangle t) \end{bmatrix}' \tag{38}$$

where

j : j th frequency

k : k th time instant

l : l th response

m: m th direction

H_{jklm} : output matrix

$\triangle t$: time step interval

If the number of x and z changes, the size of the rest of the matrix is also determined as shown in Table 4 below.

Table 4 Dimension of Variables for Directional Wave.

Variable	Description	No. of Row	No. of Column
x	State Vector	(2*j)*m	1
z	Measurement Vector	l	1
ϕ	State Transition Matrix	(2*j)*m	(2*j)*m
H	Output Matrix	l	(2*j)*m
P	Error Covariance Matrix	(2*j)*m	(2*j)*m
K	Kalman Gain	(2*j)*m	l
R	Measurement Error Covariance Matrix	l	l
Q	Model Error Covariance Matrix	(2*j)*m	(2*j)*m

Using the formula and variable given above, the Kalman filter estimate x. The equation for calculating the directional spectrum from the x is different from that of the scalar spectrum. For scalar spectrum, the wave spectrum was calculated from the estimated x by Equation (16). On the other hand, in case of the directional spectrum, $\triangle\theta$ is included as in the Equation (36). It is because the equation between the magnitude of the directional spectrum and the amplitude includes not only the frequency but also the directional component. Therefore, the direction spectrum is calculated from x by Equation (39):

$$S_{\varsigma}(\omega_j, \theta_m) = 0.5 \times \frac{1}{\Delta\omega_j} \times \frac{1}{\Delta\theta_m} \times (\hat{x}_{2j-1}^2 + \hat{x}_{2j}^2) \tag{39}$$

Regarding the error of 6 DOF motion, the standard deviations of translational motions (surge, sway and heave) are set 0.023m as the same. For rotational motions (roll, pitch and yaw), those are set 0.028°, 0.032° and 0.028°, respectively. This error is referring to the test result of a commercial product (SBG Systems, 2018). This sensor error is calculated in the Kalman filter in the form of covariance, as shown in equation (20).

Forward Speed Inclusion

Another challenge in wave spectrum estimation is when the vessel has a forward speed. The frequency of the wave spectrum is based on a fixed point in the ocean. However, when the vessel is sailing at a certain speed, it needs to transform into the reference frame of the moving vessel. Figure 37 shows the relative direction of the incident wave as the ship is sailing at forward speed U. And Equation (40) represents the relationship between typical wave frequency ω and the encounter frequency ω_e (Reid and Parent, 1982).

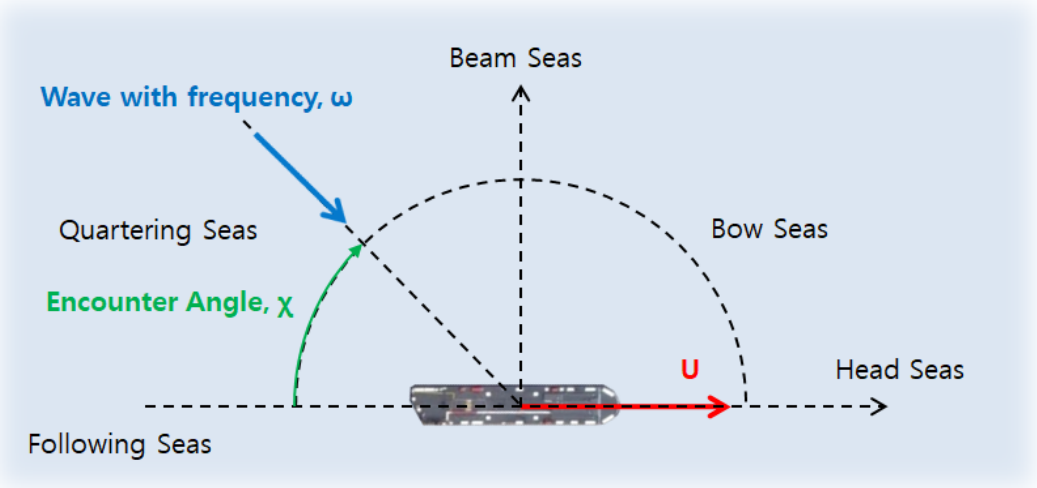

Figure 37 Encounter Angle.

$$\omega_e = \omega - \frac{\omega^2 U \cos\chi}{g} \tag{40}$$

Figure 38 shows the relationship between ω and ω_e when Equation (40) is applied to different wave directions.

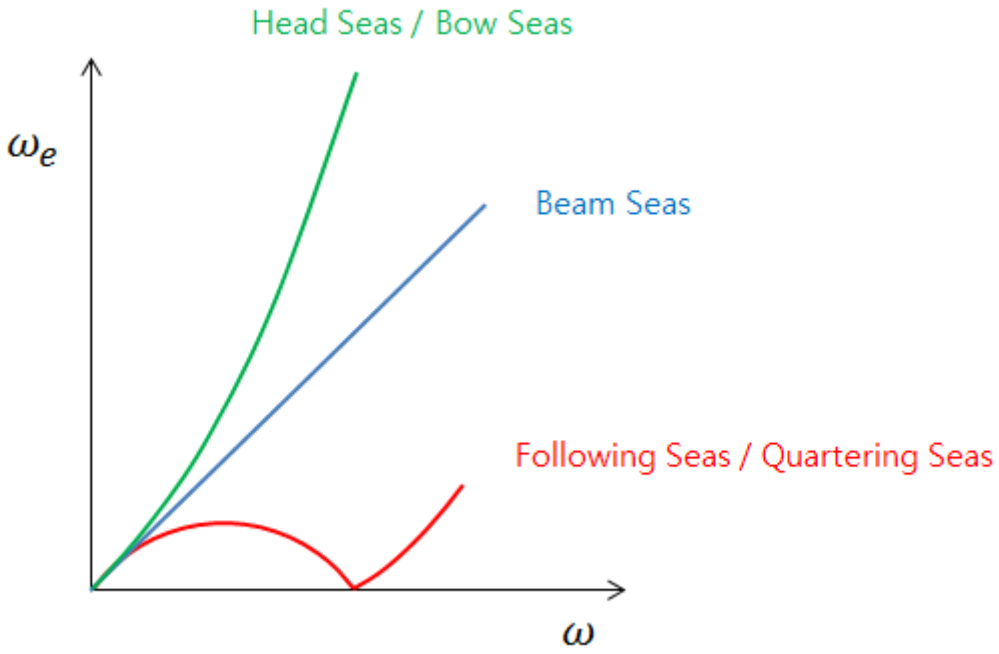

Figure 38 Typical Wave Frequency and Encounter Frequency.

The encounter frequency (ω_e) is greater than the wave frequency in a head sea. But it is generally less than the wave frequency in following seas. It is a Doppler effect (Reid and Parent, 1982). Thus, the wave spectrum will be shifted to different frequency ranges along the frequency axis. For example, a typical ocean wave spectrum looks like top graph of Figure 39. Assuming a ship is sailing in head seas for this wave spectrum, the spectrum on the encounter frequency domain would be as shown in bottom graph of Figure 39.

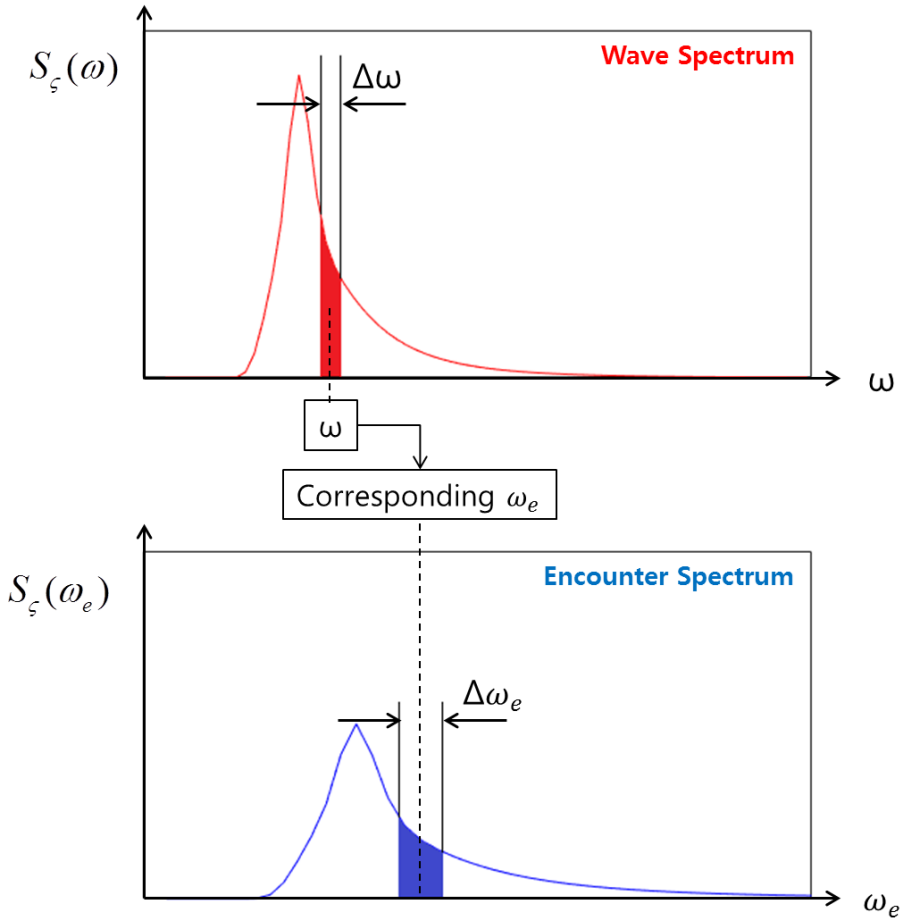

Figure 39 Area Under Typical Wave Spectrum and Encounter Spectrum.

When the original wave frequency range is shifted to equivalent encounter frequency, the shaded region of the two graphs in Figure 39 must the same. This is because the energy in a given range of wave frequency must match the energy in the shifted one of the encounter frequencies. The area of the section is;

$$S_\varsigma(\omega_e)\Delta\omega_e = S_\varsigma(\omega)\Delta\omega \tag{41}$$

The observed data from the motion sensors installed on the sailing vessel is the motion in the reference frame of the moving body. The excitation that it measures in moving vessels would be at the encounter period. For the test of wave estimation, first of all, ship motion at a forward speed is necessary, which is the input to the Kalman filter.

To generate the motion time series at a forward seed, the motion spectra for every discretized direction on the encounter frequency domain was calculated by using the Equation (42). And the corresponding irregular-motion time series were generated from the obtained motion spectra by Equation (43). Since the vessel's TF set in the Kalman filter is also on the encounter domain, the wave spectrum estimated from the filter also becomes on the encounter domain. If we converted it back to the original frequency satisfying the two Equations (40) and (41), the original wave spectrum is finally acquired. Figure 40 below shows this whole process.

$$S_{z,jm}(\omega_e) = RAO_{jm}(\omega_e)^2 \cdot S_{\varsigma,jm}(\omega_e) \tag{42}$$

$$Z_e(t) = \sum_{m=1}^{n_\theta} \sum_{j=1}^{n_f} \sqrt{2S_z(\omega_{e,j}, \theta_m) \triangle\omega_e \triangle\theta} \cdot \cos(\omega_{e,j} t + \varepsilon_j + \varphi_{jm}) \tag{43}$$

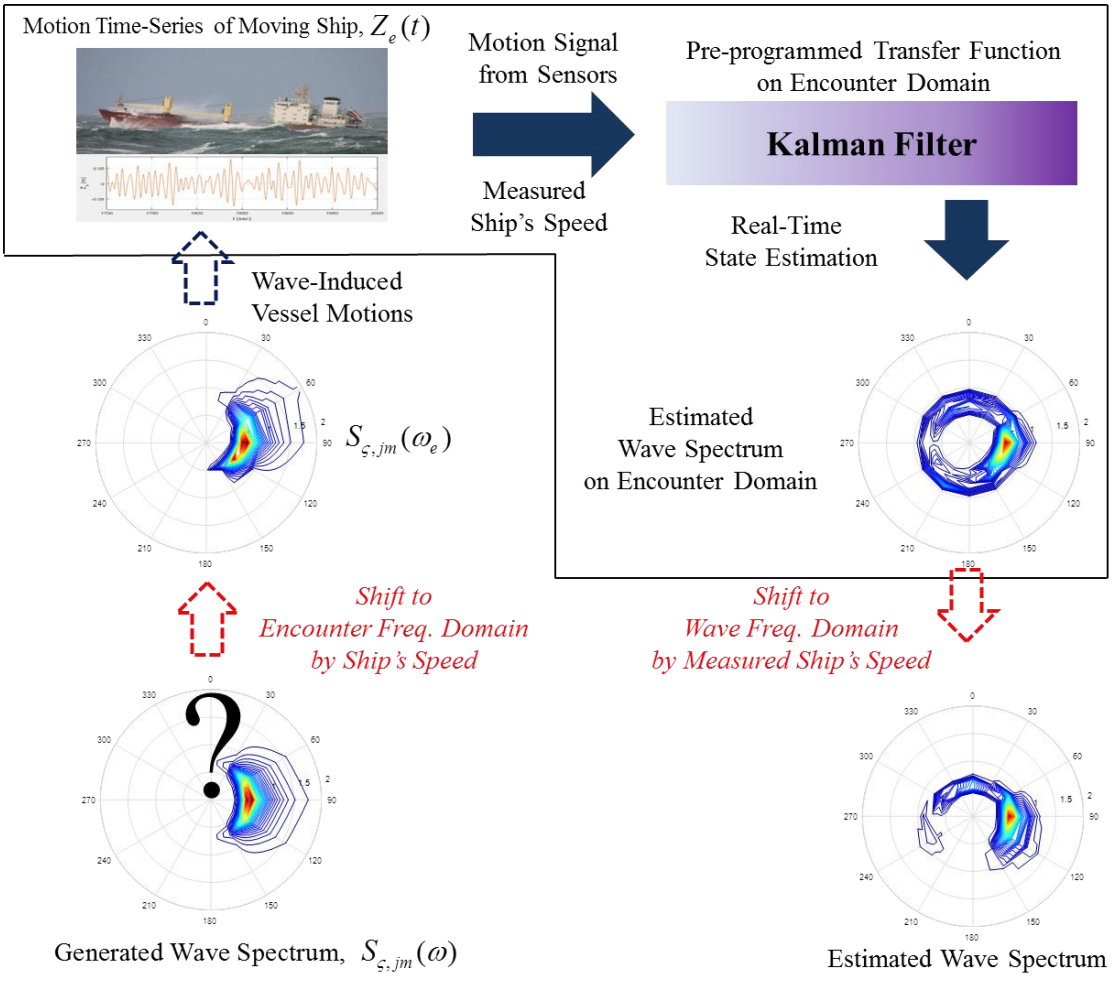

Figure 40 Directional Wave Spectrum Estimation Process Using Kalman Filter for Forward Speed Inclusion.

Results and Discussion

Directional wave spectra were estimated with Kalman filter applying principle of Wiener filter for various sea states and wave mean directions at ship's speed, 10 knots as Table 5. The $\bar{\mu}$ on the table is the mean direction of wave propagation. And the direction reference follows Figure 36. In other words, if $\bar{\mu}$ is 0 degrees, it corresponds to head seas, 90 degrees is beam seas, and 180 degrees is following seas. The last Case No. 7 is

assumed to test the multi-directional wave spectrum. This is the case when Hs sea, 2m and Hs swell, 5m are incident together. The spreading factor, s is set as 2.0. The frequency interval $\Delta\omega$ was 0.08 rad/s.

Table 5 Simulated Sea States and Their Parameters for Directional Spectrum (Ship's Speed: 10 Knots).

Case No.	Sea			Swell		
	Hs (m)	Tp (s)	$\bar{\mu}$ (deg.)	Hs (m)	Tp (s)	$\bar{\mu}$ (deg.)
1	5	9	30	-	-	-
2	5	9	90	-	-	-
3	5	9	135	-	-	-
4	8	15	0	-	-	-
5	8	15	60	-	-	-
6	8	15	180	-	-	-
7	2	7	135	5	15	0

Figure 41–Figure 47 present the simulation results of the inversely estimated real-time directional spectra for all the cases in Table 5. It is seen that the developed Kalman filter technique works well for various ocean environments even when the ship is moving at forward speed.

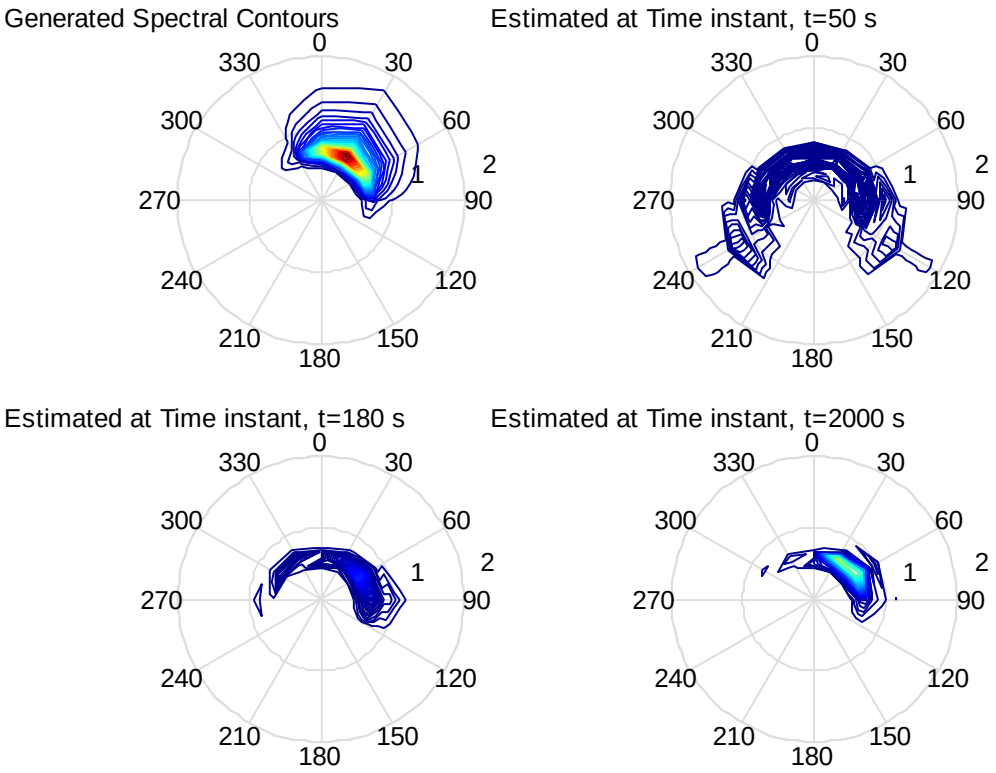

Figure 41 Generated and Estimated Spectrum (Case #1, Hs = 5 m, Tp = 9 s, $\bar{\mu}$ =30°).

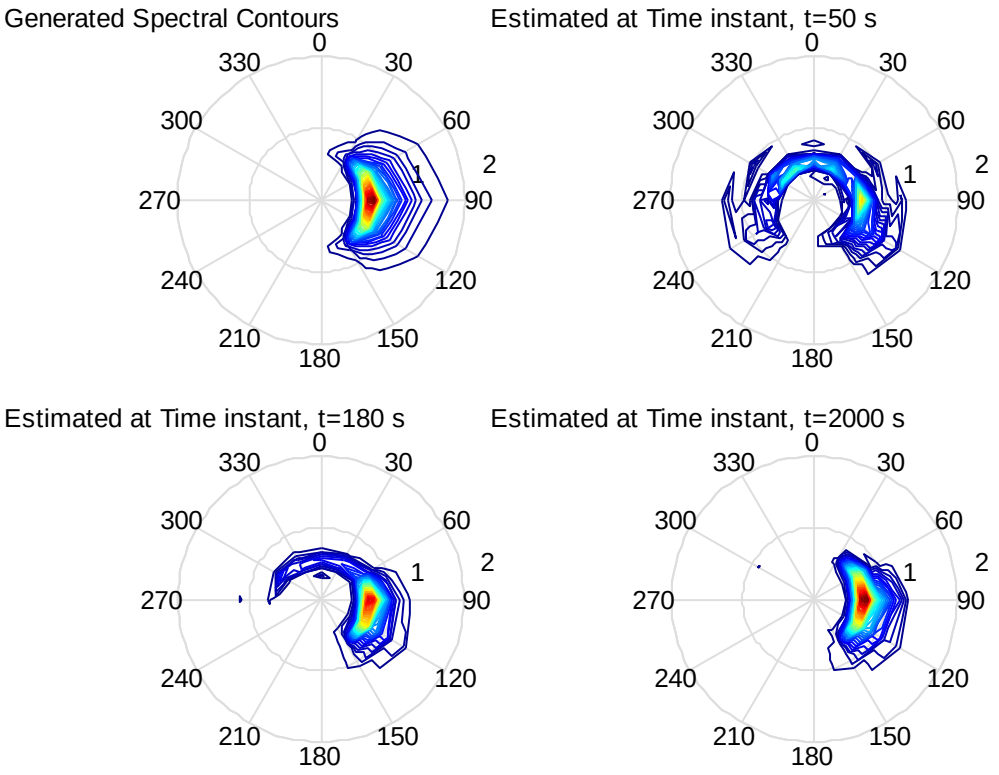

Figure 42 Generated and Estimated Spectrum (Case #2, Hs = 5 m, Tp = 9 s, $\bar{\mu}$ =90°).

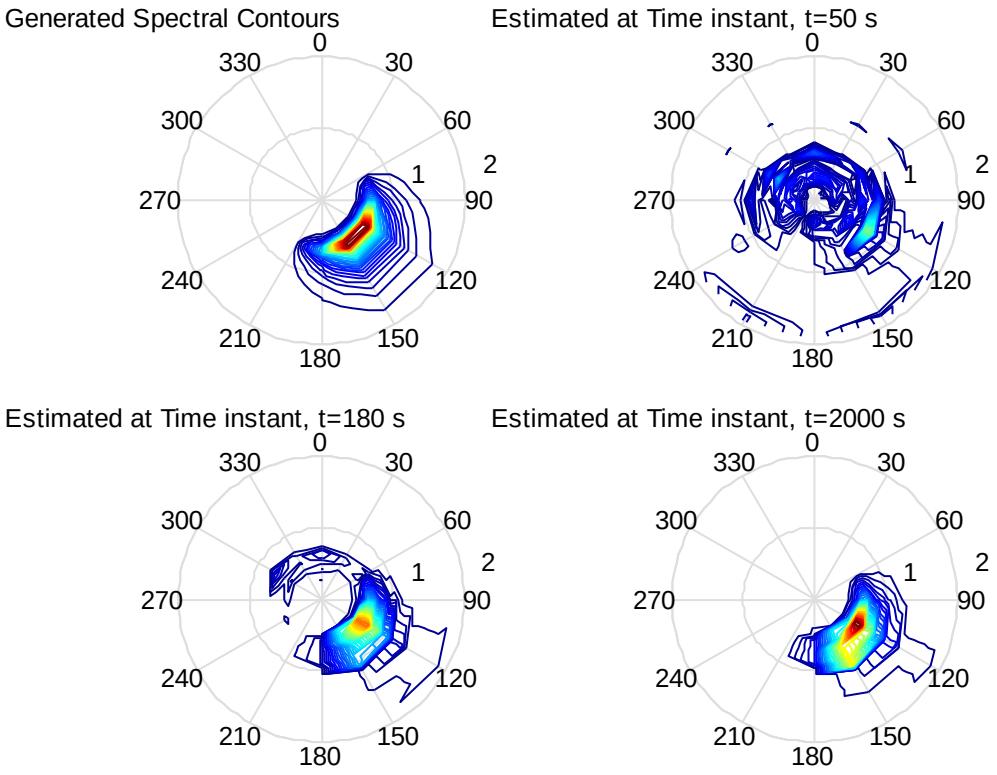

Figure 43 Generated and Estimated Spectrum (Case #3, Hs = 5 m, Tp = 9 s, $\bar{\mu}$ =135°).

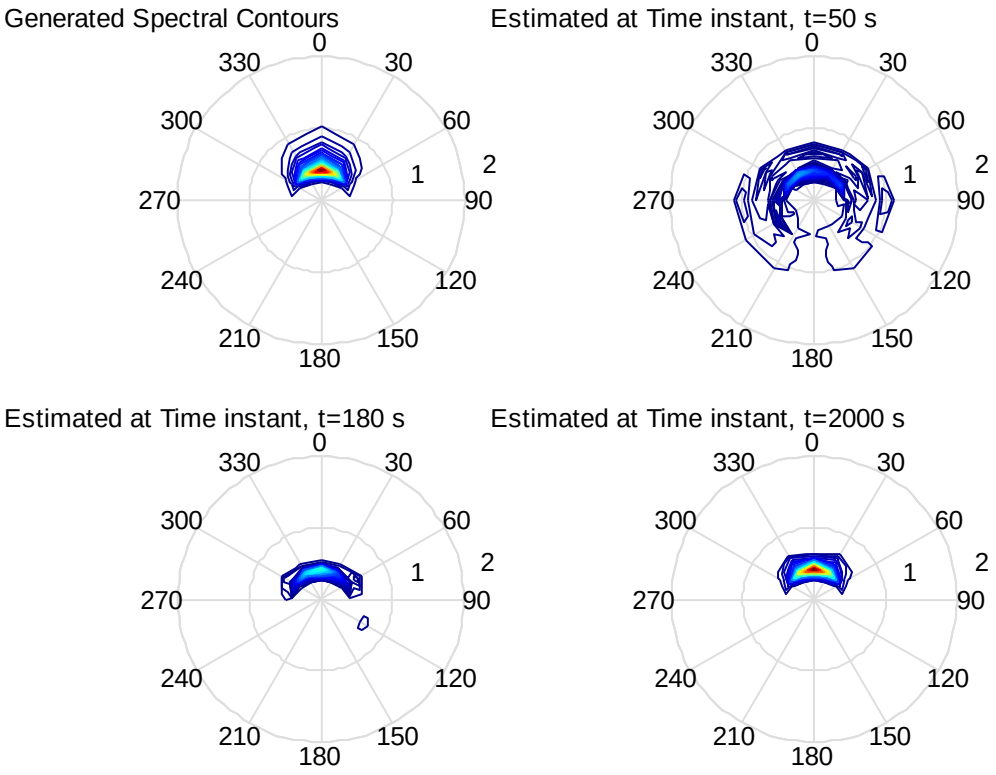

Figure 44 Generated and Estimated Spectrum (Case #4, Hs = 8 m, Tp = 15 s, $\bar{\mu}$=0°).

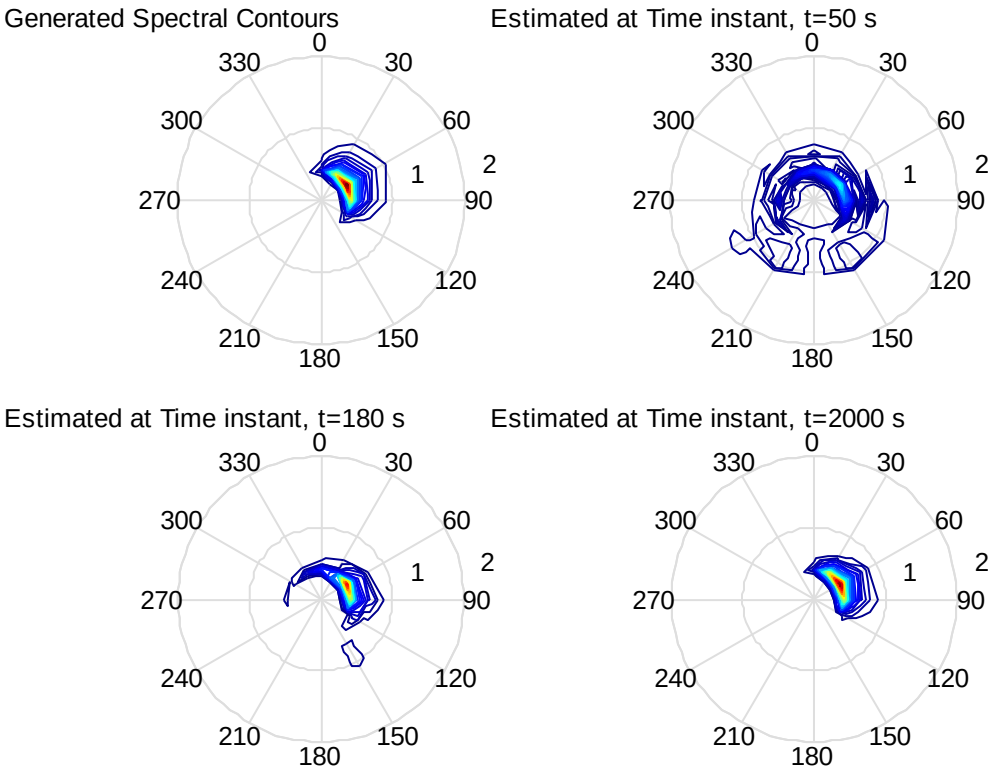

Figure 45 Generated and Estimated Spectrum (Case #5, Hs = 8 m, Tp = 15 s, $\bar{\mu}$ =60°).

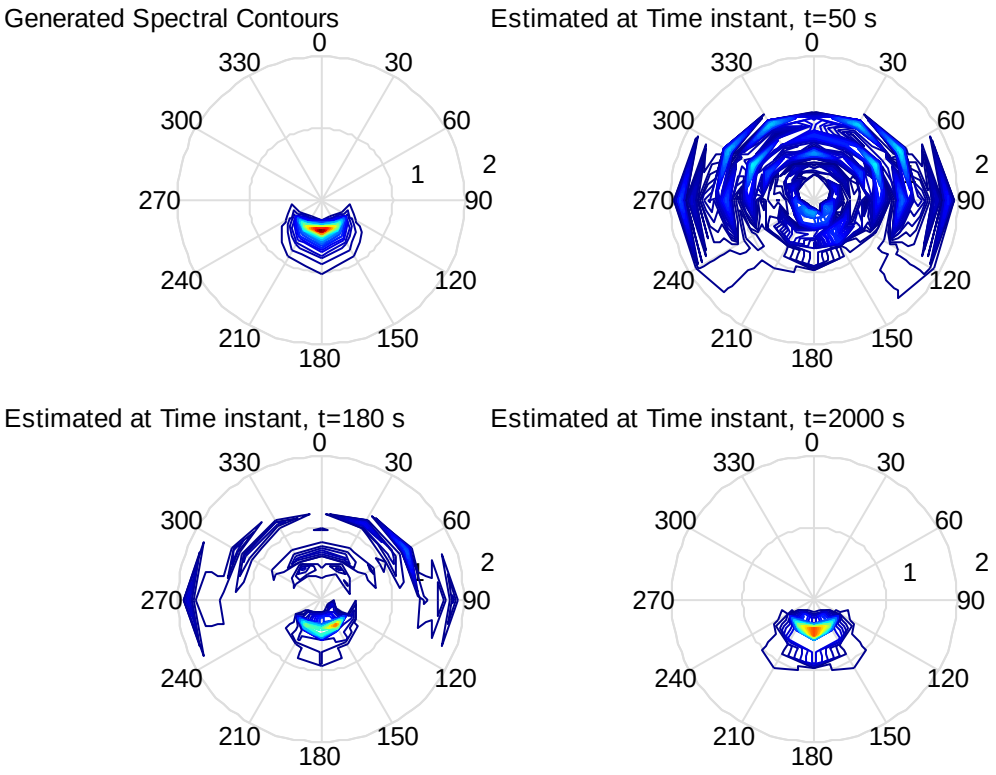

Figure 46 Generated and Estimated Spectrum (Case #6, Hs = 8 m, Tp = 15 s, $\bar{\mu}$ =180°).

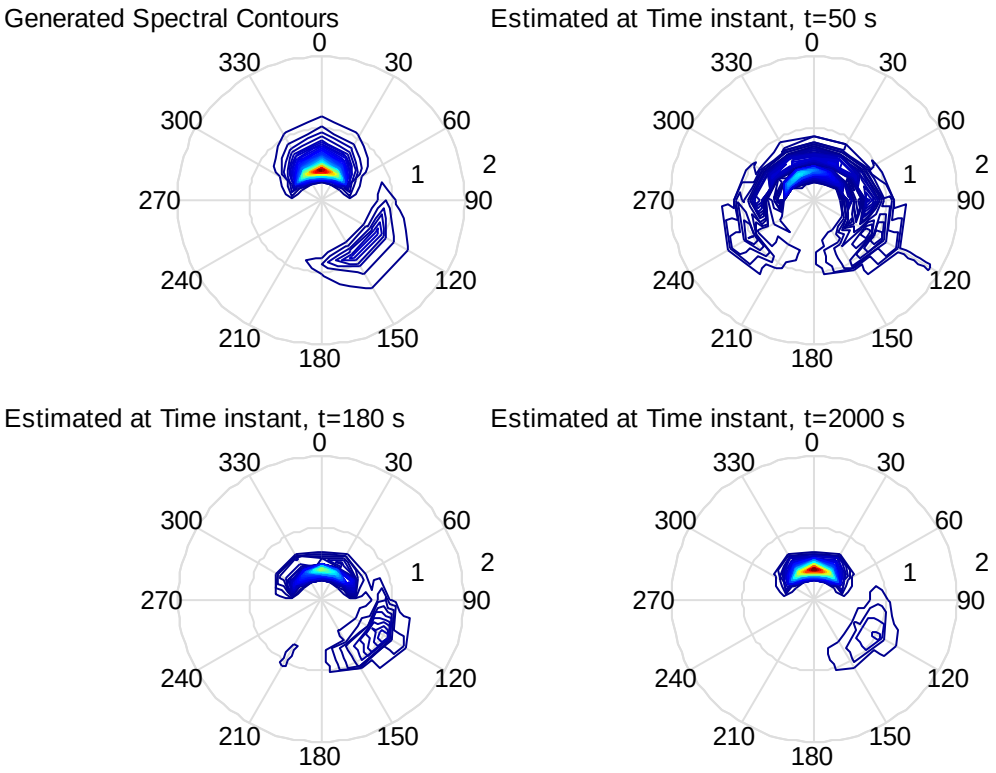

Figure 47 Generated and Estimated Spectrum (Case #7, Hs sea = 2 m, Tp sea = 7 s, $\bar{\mu}$ sea=135°, Hs swell = 5 m, Tp swell = 15 s, $\bar{\mu}$ swell=0°).

It is interesting to analyze the estimated spectra for all directions and evolution of estimated Hs, Tp for directional wave. Figure 48 is estimated spectra for all directions, which corresponds to simulation of Case #7, multi-directional wave spectrum case. In the figure, 300, 330, 0, 30 and 60 degrees are discretized spectra of swell. The 90, 120, 150 and 180 degrees are discretized spectra of sea. Not only the mean direction, it is shown that the estimations for the spreading directions are also in good agreement with generated spectrum.

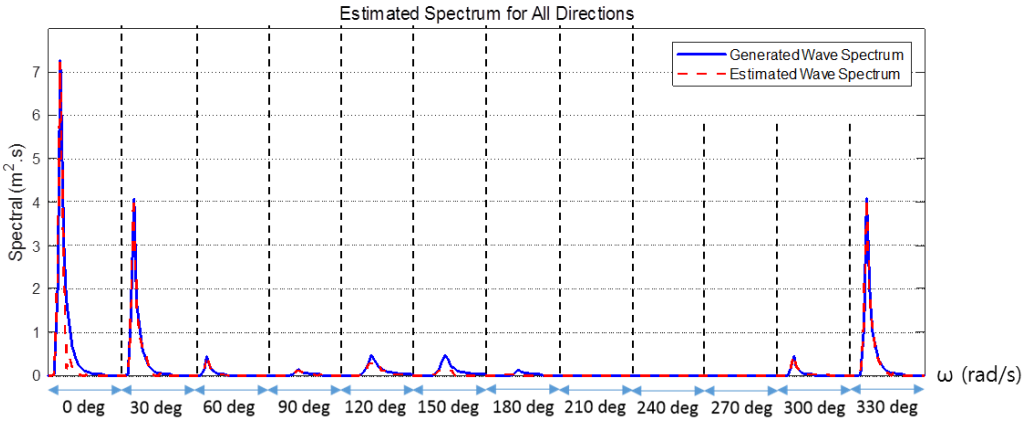

Figure 48 Generated and Estimated Spectra for All Direction.

Figure 49 presents the Hs and Tp with time for swell of Case #7. As simulation time goes, estimated Hs and Tp converged to generated value. In Figure 50, the original and inversely estimated mean direction ($\bar{\mu}=0°$) wave profiles of swell also agree very well.

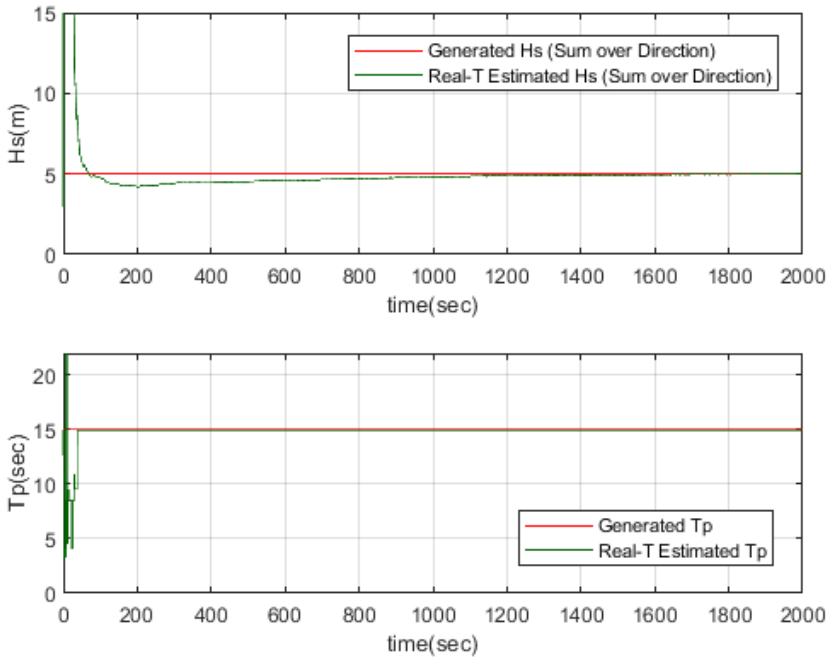

Figure 49 Evolution of Parameters (Case #7, Hs swell = 5 m, Tp swell = 15 s,).

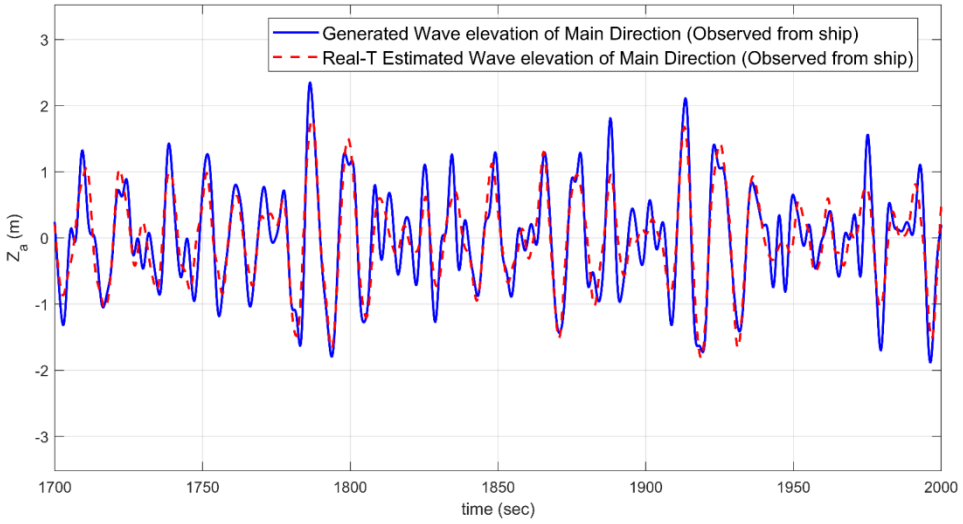

Figure 50 Mean Direction-Wave Elevation of Swell (Case #7, Hs swell = 5 m, Tp swell = 15 s,).

CHAPTER III

REAL-TIME ESTIMATION OF RISER'S DEFORMED SHAPE USING INCLINOMETERS AND EXTENDED KALMAN FILTER

Riser Monitoring System

Current technology for riser monitoring is summarized in this section. Various types of sensors are used for riser monitoring, such as accelerometer, strain gauge, inclinometer, angular velocity sensors, and curvature sensors (Cook et al., 2006; Karayaka, 2009; Karayaka et al., 2009; Peng and Zhi, 2012; Podskarbi and Walters, 2006; Podskarbi et al., 2007; Thethi et al., 2005). Signals measured by various sensors are used for riser integrity analysis with different analysis methods, as summarized in Table 6 (Mercan et al., 2016). Each method has unique advantages and disadvantages. While the wave-frequency responses of a riser are mainly induced by wave excitations, current can induce high-frequency VIV responses. Based on the riser type, behavior, and situation, the target analysis method should be determined. For instance, transfer function and mode matching methods need finite element (FE) analysis to acquire the transfer function and modal amplitude, and prediction accuracy is diminished for the location far from the sensor location. The Timoshenko-beam-based analytical method is also applicable for response estimation under wave and VIV excitations. However, the measured acceleration data from sensors are converted into curvature with an analytical transfer function. It is not easy to reflect actual structural properties, such as structural damping and added mass, and the fatigue calculation is only available at the sensor

location. Also, the g-contamination contained in the measured acceleration must be eliminated for more accurate monitoring (Ge et al., 2014). Additionally, this method is vulnerable to the sensor error. On the other hand, the proposed EKF-based monitoring system can generically overcome the sensor error inside of the algorithm.

Table 6 Comparison of Riser Fatigue Analysis Methods.

Parameters	Analytical Method	Transfer Function Method	Mode Matching Method
Riser Response	Wave & VIV	Wave & VIV	VIV
FEM required	No	Yes	Yes
Accuracy	High (Application Limited)	Moderate	Low

Method and Formulation

The objective of this study is to real-time estimate the riser's deformed shape from measured sensor signals. Sensors include multiple inclinometers along the riser and GPS for tracing top connection to the platform. Then, real-time estimation of riser's deformed shape from the sensor signals is necessary and the EKF is selected. The detailed methodology and formulations are explained in the following sections.

Sensor Data

Figure 51 shows the configuration of the riser monitoring system. For a typical riser system, one end of the riser is anchored to the seabed, and the other end is connected to the floating platform. Above the sea surface, the Global Navigation

Satellite System (GNSS) or platform position monitoring system can be used to monitor the riser-top positions.

However, underwater, only contract type sensors, such as IMUs, accelerometers, inclinometers, strain gauges, can be placed on the riser. Among them, we selected inclinometers, which measure bi-axial (inclination and heading) riser angles. The top and bottom points of the riser are known at each time, as explained in the above. As shown in Figure 51, the riser can be divided into n nodes, and n-1 inclinometers are installed at the center of each segment. In the present example, identical sensor intervals were selected for simplicity, although variable sensor intervals can also be used. Table 7 summarizes the sensors needed for the EKS system. Sensor signals are assumed to be measured and transmitted to the platform, which allows real-time monitoring through computer embedded algorithms.

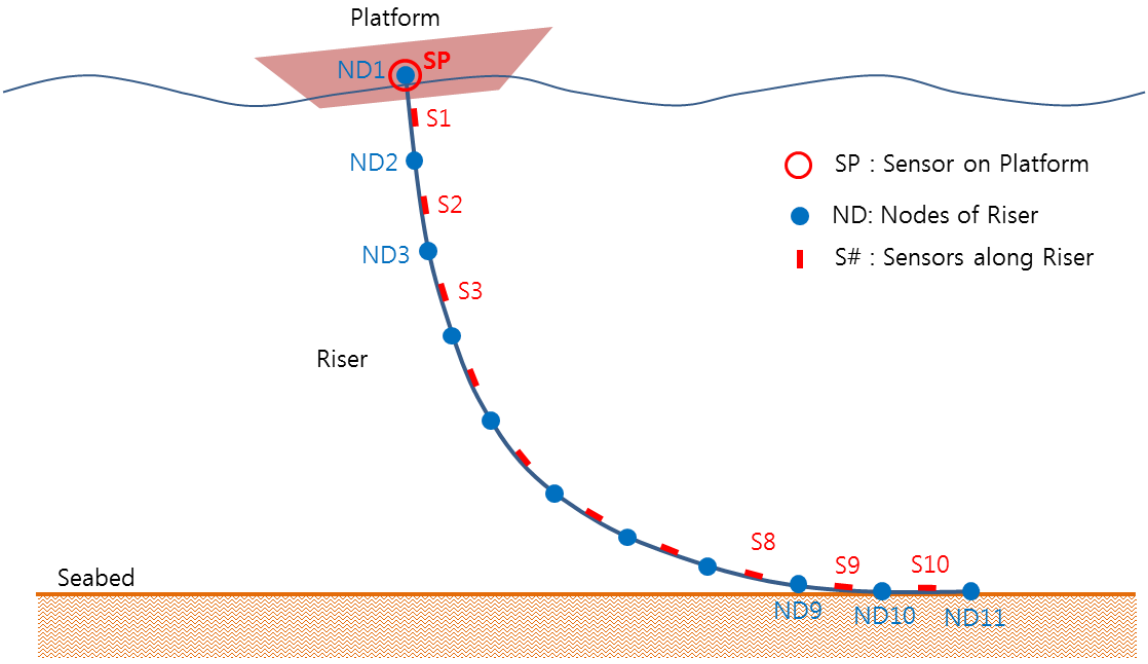

Figure 51 Configuration of Riser Monitoring System.

Table 7 Required Sensors and Their Locations.

Sensor Location	Measured Data	Number of Sensors
At platform (Above water surface)	Top Position (x, y, z)	1
At the midpoint between nodes along riser (Underwater)	Inclination	*n-1*
	Heading	*n-1*

Extended Kalman Filter

The EKF was selected to define the relationship between input signals and riser's deformed shape. The Kalman filter is an algorithm that estimates the state based on the statistical properties with the measurement. It is a very practical algorithm, commonly applied to guidance-navigation-control of vehicles and inverse wave spectrum estimation

(Kim et al., 2019). The EKF is the nonlinear version of the Kalman filter through the linearization of the non-linear function. Kalman filtering is applied to the system model of Equations (44) and (45) in the state space as:

$$X_{k+1} = f\left(X_k\right) + w_k \tag{44}$$

$$z_k = h\left(X_k\right) + v_k \tag{45}$$

where

X_k = process state vector
f = nonlinear eqation for state vector
w_k = model error vector
z_k = measurement vector
h = nonlinear eqation for measument vector
v_k = sensor error vector

It assumes that there exists a model error w in the state X and a sensor error v in the measurement z during the transition to the next time step. Note that in the riser monitoring system, the process state vector X consists of the x and y coordinates of the nodes. The covariances for the two errors are given by:

$$Q = E[w_k w_k^T] \tag{46}$$

$$R = E[v_k v_k^T] \tag{47}$$

The Kalman filter keeps reducing the prediction error of the state X through the recursively-calculating process. The process is made up of four steps, as described in Figure 52. The superscript, '-' means the predicted value for the next time step. Otherwise, it means the calculated (or estimated) value from measurement at the current time step.

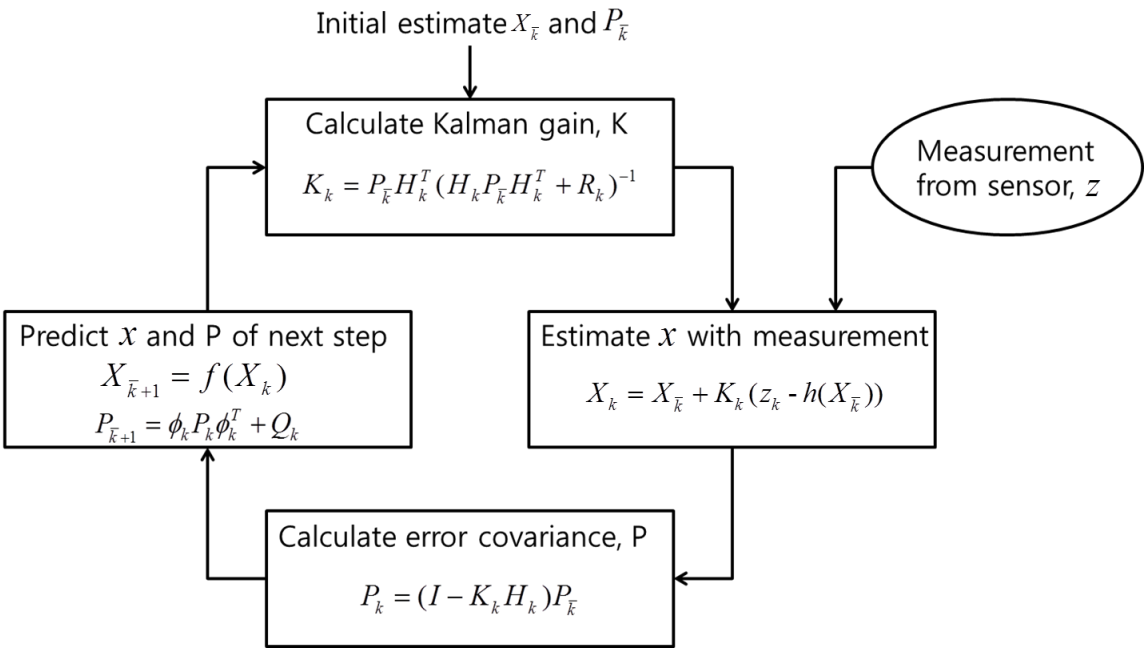

Figure 52 Extended Kalman Filter Loop.

where

$X_{\bar{k}}$ = predicted state vector

X_k = estimated state vector

$P_{\bar{k}}$ = predicted error covariance matrix

P_k = estimated error covariance matrix

ϕ_k = state transition matrix

K_k = Kalman gain

H_k = output matrix

Q_k = model error covariance matrix

R_k = measurement (sensor) error covariance matrix

As presented in Figure 52, Kalman gain, process state, and error covariance can be calculated as:

$$K_k = P_{\bar{k}} H_k^T (H_k P_{\bar{k}} H_k^T + R_k)^{-1} \tag{48}$$

$$X_k = X_{\bar{k}} + K_k (z_k - h(X_{\bar{k}})) \tag{49}$$

$$P_k = (I - K_k H_k) P_{\bar{k}} \tag{50}$$

$$X_{\bar{k}+1} = f(X_k) \tag{51}$$

$$P_{\bar{k}+1} = \phi_k P_k \phi_k^T + Q_k \tag{52}$$

The initial state $X_{\bar{1}}$ is to be estimated, and the initial error covariance $P_{\bar{1}}$ should be determined by the designer. The determination of the initial sate $X_{\bar{1}}$ is discussed in

the next section. If initial P ($P_{\bar{1}}$) is too small, it will result in small Kalman gain K , as given in Equation (48), at the beginning of the calculation.

Small K means giving more weight to sensor measurement than prediction. Subsequently, at the beginning of the filtering, the measurement is relatively neglected, and the prediction is overly counted. In other words, the $P_{\bar{1}}$ determines the initial convergence rate of the state X . Small P delays the initial convergence rate. Therefore, when the designer does not have prior knowledge of X , reasonably large initial error covariance $P_{\bar{1}}$ should be set (Simon, 2006). In this study, therefore, sufficiently large $P_{\bar{1}}$ was set, as given in Equation (53). The 'diag' means taking the diagonal from a matrix into a vector form and vice-versa.

$$P_{\bar{1}} = diag\begin{pmatrix} 100_1 \\ 100_2 \\ \vdots \\ 100_{i-1} \\ 100_i \end{pmatrix} \tag{53}$$

where

i = length of X

R is measurement error covariance, which is generally determined from the error performance of the given sensor. An adaptive R may be applied when the sensor

error is not statistically constant in the actual filtering process. In the estimation step, optimum X is calculated by using the weight factor K, as given in Equation (49).

In Equations (48) and (50), H matrix is used instead of the nonlinear function h of input X and output z. This H is used to approximate the system by linearizing the h function of $z = h(X)$. If the output for a particular input x_1 is z_1, the approximated z_2 for input x_2 can be calculated by using the derivative of the h at a point x_1. This feature is called Jacobian, and the matrix of the first-order derivatives of the function h for all inputs is referred to as the Jacobian matrix J_h. If h is differentiable at a point x, its differential is represented by J_h. Then, the linear transformation represented by H is the best linear approximation of h near the point x. In summary, as the function h is defined as $z = h(X)$, the J_h (here defined as H), i.e., Jacobian matrix of h, consists of the first derivatives of h and can linearize the model as $z \approx J_h \cdot X = H \cdot X$. More details about H are discussed in the next section. Likewise, in Eq. 9, the Jacobian matrix ϕ_k is used to linearize the f. In the riser monitoring system, ϕ_k is an identity matrix. The extended Kalman filter is characterized by using h and f in Equations (49) and (51), respectively.

In the prediction step, P is increased by model error covariance Q. Q is a design parameter that can be adjusted by the designer. This process is repeated.

The conventional Kalman filter is not directly suitable for practical applications. Therefore, the research related to using Kalman filter focuses mainly on the design of an

adaptive type to fit a specific model including the optimization of the design factors, R and Q. The optimized R and Q lead to the improvement of the estimation performance of the filter. However, the option chosen here is to use fixed R and Q because the main purpose of this study is implementing shape estimation of the entire riser with the extended Kalman filter. From a number of tests, the appropriate Q value was set as Equation (54), which shows good estimation and no divergence of P.

$$Q = diag\begin{pmatrix} 5\times10^{-4}{}_1 \\ 5\times10^{-4}{}_2 \\ \vdots \\ 5\times10^{-4}{}_{i-1} \\ 5\times10^{-4}{}_i \end{pmatrix} \tag{54}$$

where

i : length of X

R was calculated by Equation (55). The standard deviation of inclination and heading sensor errors are set to be 0.05° and 0.08°, respectively, referring to the test result of a commercial product (Safran, 2020; Vectory Sensor Systems, 2020).

$$R = diag\begin{pmatrix} \beta_1^{\,2} \\ \gamma_1^{\,2} \\ \beta_2^{\,2} \\ \gamma_2^{\,2} \\ \vdots \\ \beta_{l-2}^{\,2} \\ \gamma_{l-2}^{\,2} \\ \beta_{l-1}^{\,2} \\ \gamma_{l-1}^{\,2} \end{pmatrix} \tag{55}$$

where

β : inclination sensor noise (error) standard deviation
γ : heading sensor noise (error) standard deviation
l : half the length of X

Profile-Estimation Process

In this section, how the EKF algorithm can be utilized for the real-time inverse estimation of riser's deformed shape from sensor signals is explained in detail. Figure 53 shows the lumped-mass-based riser model. A continuous riser was divided into a certain number of nodes and segments. Inclinometers were positioned in the middle of the segments. As inclination and heading are measured by the installed sensors along the riser, the developed Kalman filter can estimate the displacements of each node by the given sensor signals at each time step. Connecting the estimated nodes provides an estimated deformed shape of the riser.

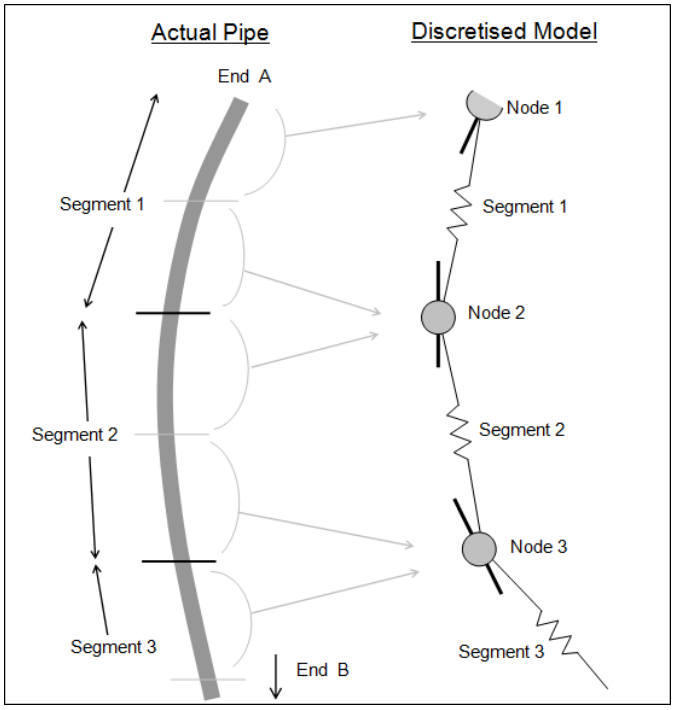

(a) Node and Segment

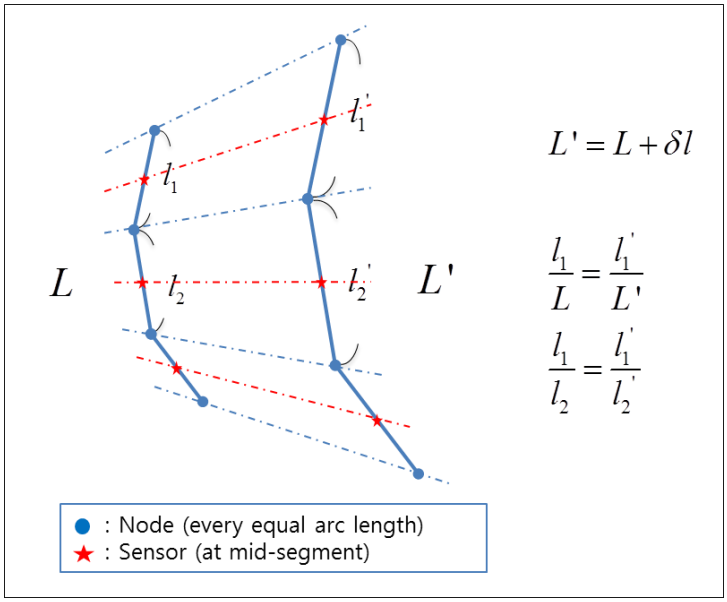

(b) Uniform elongation

Figure 53 Riser Model. Adapted from Orcina Ltd (2018).

Figure 54 explains the estimation process at each time step. As mentioned before, the 3D problem with time-varying angles is actually solved at each time step. However, in Figure 54, the 2D problem (inclination considered, heading not considered) is explained for simplicity. Besides, for the demonstration purpose, only three nodes of N1 - N3 are considered with one unknown point of N2 (x_2, z_2), which needs to be solved. It is assumed that the two inclination angles at the two ends, N1 and N3, are 28 and 62 degrees, and the vertical distance between the two points is given by 10 m. At each time step, the position of node N2 (x_2, z_2) is estimated while satisfying the given inclinations of riser segments and mid-length requirement. The blue dot is the actual position of the center node N2. As for the mid-point, the lengths of the upper and lower segments should be the same.

The detailed calculation process is as follows. (1) At time step k=1: Before starting the prediction, the initial position of node N2 (x_2, z_2) should be determined. Since the positions of nodes at both ends are already known, the central point (orange circle in the orange dashed line) of the straight line connecting the two nodes is set to be the initial position of point N2 and the initial values of dz are then determined to be 5 m each. Next, the Kalman filter predicts the x coordinate of N2 on the horizontal line (red dashed line) corresponding to dz_2 =5 m satisfying the slopes θ_1 and θ_2 from the sensors, which is corresponding to the red circle (-8.0 m, 5.0 m). However, this position violates the condition of mid-point. As a result, N2 is updated along the already estimated riser profile (red line) so that both segment lengths can be identical, which is corresponding to

the red box (-6.7 m, 4.5 m). Next, update the vertical location of the node N2, i.e., dz_2 =4.5 m for the next time step.

(2) At time step k=2: The x coordinate is predicted on the horizontal line (green dashed line) corresponding to dz_2 =4.5 m, which also satisfies the slopes θ_1 and θ_2 from the sensors. The estimated position is corresponding to the green circle (-7.0 m, 4.5 m). The length of each segment is again calculated based on this estimated position. Next, the center position of the total length is recalculated along the green line so that both lengths can be identical, which is corresponding to the green box (-6.6 m, 4.0 m). Update the vertical location of node N2 again, i.e., dz_2 =4 m. Repeat this process for every time step until satisfactory convergence is achieved, i.e. the predicted position of N2 converges to the blue circle after several time steps, which is the actual position.

In summary, the position of N2 is estimated at each time step while satisfying the two given angles and length requirement. The same process runs simultaneously for the whole segments inside a combined matrix until all the requirements are simultaneously satisfied. As shown in Figure 55, the 2D problem can logically be expanded to the 3D one with additional heading angles and y coordinates of the nodes.

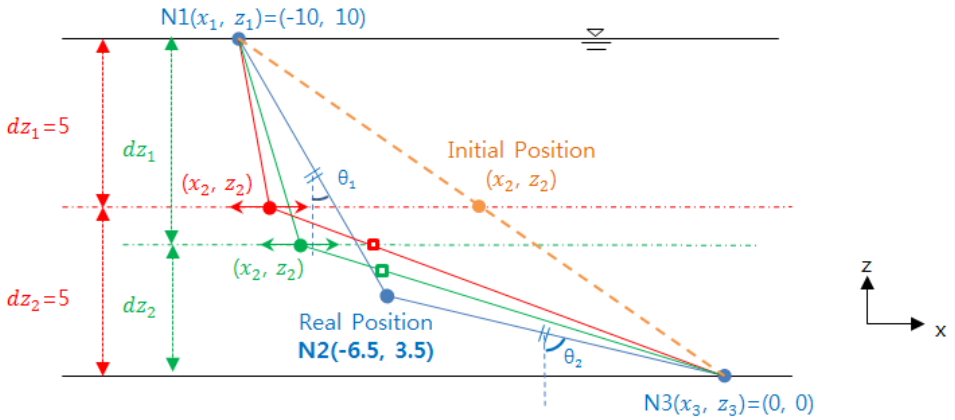

Time step (k)	k=1	k=2	k=3	...
Reference Vertical Coordinate (Estimated vertical position of node)	dz_2=5.0 (initial)	dz_2=4.5	dz_2=4.0	
Measured Segment Inclination	θ_1=28° θ_2=62°	θ_1=28° θ_2=62°	...	
Estimated Position of N2 by E.K.F. (x_2, z_2)	● (x_2, z_2)=(-8, 5)	● (x_2, z_2)=(-7, 4.5)	...	● (x_2, z_2)=(-6.5, 3.5)
Calculate Midpoint of Line Length	□ (-6.7, 4.5)	□ (-6.6, 4.0)	...	
Update Reference Vertical Coordinate	dz_2=4.5	dz_2=4.0	...	

Figure 54 Estimation Process in 2D with 3 Nodes.

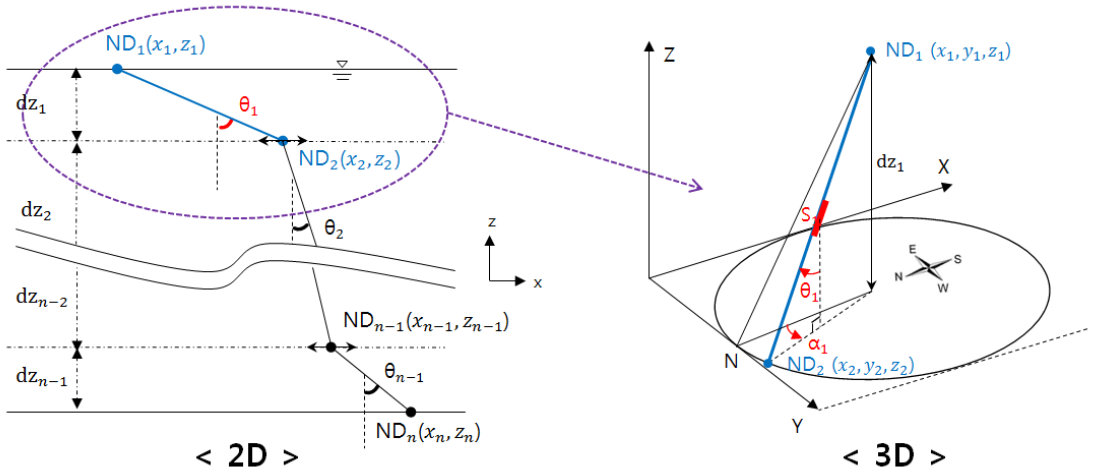

Figure 55 Estimation Process in 2D and 3D with n Nodes.

where

θ = mid-segment inclination

α = mid-segment heading

n = the number of nodes

x = estimated x coordinate of node

y = estimated y coordinate of node

dz = estimated vertical component of segment length

One of the important issues to the Kalman filter is to establish the observation equation, also referred to as the output equation. The relationship between measurement and estimated state is defined in the observation equation. In this study, measurement is the inclination and heading at each segment, while the state is x and y coordinates of each node. The vertical coordinate is determined by dz updated at every time step.

Based on the configuration shown in Figure 55, the observation equation can be expressed as:

$$\theta_n = h_1(x_n, x_{n+1}, y_n, y_{n+1}) = \arctan\left(\frac{\sqrt{(x_{n+1}-x_n)^2+(y_{n+1}-y_n)^2}}{dz_n}\right) \tag{56}$$

$$\alpha_n = h_2(x_n, x_{n+1}, y_n, y_{n+1}) = \arctan\left(\frac{y_{n+1}-y_n}{x_{n+1}-x_n}\right) \tag{57}$$

In above Equations, h_1 and h_2 are functions for inclination and heading, respectively. Figure 56 shows the observation equation for the entire riser with n nodes.

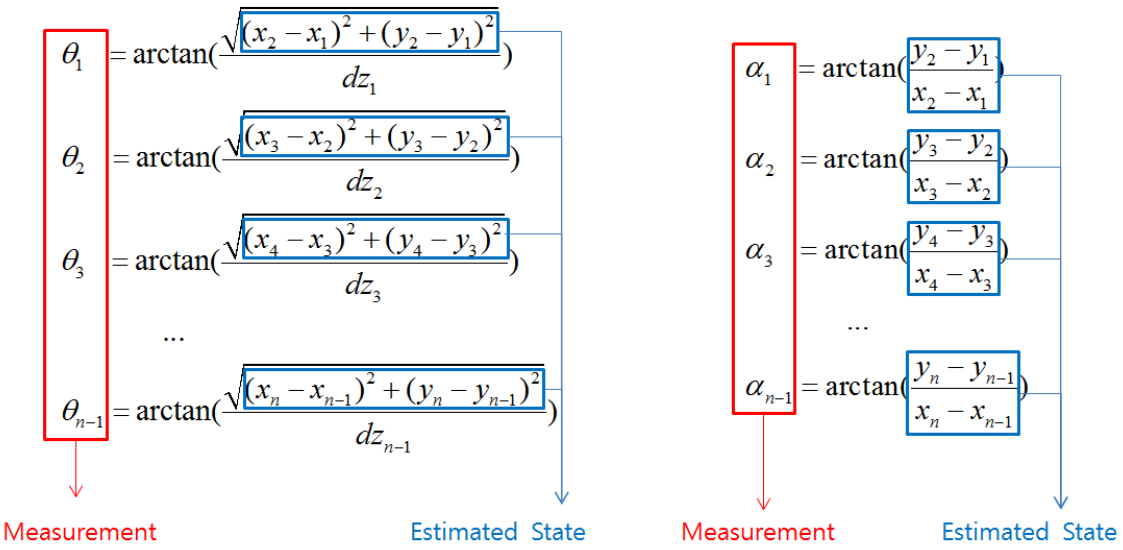

Figure 56 Observation Equation.

As mentioned before, the above nonlinear observation equation cannot be directly applied to the Kalman filter. In this regard, the EKF with the corresponding

Jacobian matrix is needed to linearize the nonlinear system model. Equation (58) is the original nonlinear equation, i.e., $z = h(X)$ while Equation (59) is the corresponding linearized equation by means of the Jacobian matrix, i.e., $z = J_h \cdot X = H \cdot X$. The $2(n-1)$ by $2n$ Jacobian matrix was constructed by considering not only the $2(n-1)$ measurement and $2n$ state but also the respective observation equation.

$$\begin{bmatrix} \theta_1 \\ \alpha_1 \\ \theta_2 \\ \alpha_2 \\ \vdots \\ \theta_{n-2} \\ \alpha_{n-2} \\ \theta_{n-1} \\ \alpha_{n-1} \end{bmatrix} = \begin{bmatrix} h_1(x_1, x_2, y_1, y_2) \\ h_2(x_1, x_2, y_1, y_2) \\ h_1(x_2, x_3, y_2, y_3) \\ h_2(x_2, x_3, y_2, y_3) \\ \vdots \\ h_1(x_{n-2}, x_{n-1}, y_{n-2}, y_{n-1}) \\ h_2(x_{n-2}, x_{n-1}, y_{n-2}, y_{n-1}) \\ h_1(x_{n-1}, x_n, y_{n-1}, y_n) \\ h_2(x_{n-1}, x_n, y_{n-1}, y_n) \end{bmatrix} \tag{58}$$

$$\begin{bmatrix} \theta_1 \\ \alpha_1 \\ \theta_2 \\ \alpha_2 \\ \vdots \\ \theta_{n-2} \\ \alpha_{n-2} \\ \theta_{n-1} \\ \alpha_{n-1} \end{bmatrix} = \begin{bmatrix} \frac{\partial\theta_1}{\partial x_1} & \frac{\partial\theta_1}{\partial x_2} & 0 & 0 \ldots & & \frac{\partial\theta_1}{\partial y_1} & \frac{\partial\theta_1}{\partial y_2} & 0 & 0 \ldots \\ \frac{\partial\alpha_1}{\partial x_1} & \frac{\partial\alpha_1}{\partial x_2} & 0 & 0 \ldots & & \frac{\partial\alpha_1}{\partial y_1} & \frac{\partial\alpha_1}{\partial y_2} & 0 & 0 \ldots \\ 0 & \frac{\partial\theta_2}{\partial x_2} & \frac{\partial\theta_2}{\partial x_3} & 0 \ldots & & 0 & \frac{\partial\theta_2}{\partial y_2} & \frac{\partial\theta_2}{\partial y_3} & 0 \ldots \\ 0 & \frac{\partial\alpha_2}{\partial x_2} & \frac{\partial\alpha_2}{\partial x_3} & 0 \ldots & & 0 & \frac{\partial\alpha_2}{\partial y_2} & \frac{\partial\alpha_2}{\partial y_3} & 0 \ldots \\ & & & & \ddots & & & & \\ \ldots & 0 & \frac{\partial\theta_{n-2}}{\partial x_{n-2}} & \frac{\partial\theta_{n-2}}{\partial x_{n-1}} & 0 & \ldots & 0 & \frac{\partial\theta_{n-2}}{\partial y_{n-2}} & \frac{\partial\theta_{n-2}}{\partial y_{n-1}} & 0 \\ \ldots & 0 & \frac{\partial\alpha_{n-2}}{\partial x_{n-2}} & \frac{\partial\alpha_{n-2}}{\partial x_{n-1}} & 0 & \ldots & 0 & \frac{\partial\alpha_{n-2}}{\partial y_{n-2}} & \frac{\partial\alpha_{n-2}}{\partial y_{n-1}} & 0 \\ \ldots & 0 & 0 & \frac{\partial\theta_{n-1}}{\partial x_{n-1}} & \frac{\partial\theta_{n-1}}{\partial x_n} & \ldots & 0 & 0 & \frac{\partial\theta_{n-1}}{\partial y_{n-1}} & \frac{\partial\theta_{n-1}}{\partial y_n} \\ \ldots & 0 & 0 & \frac{\partial\alpha_{n-1}}{\partial x_{n-1}} & \frac{\partial\alpha_{n-1}}{\partial x_n} & \ldots & 0 & 0 & \frac{\partial\alpha_{n-1}}{\partial y_{n-1}} & \frac{\partial\alpha_{n-1}}{\partial y_n} \end{bmatrix} \cdot \begin{bmatrix} x_1 \\ x_2 \\ \vdots \\ x_{n-1} \\ x_n \\ y_1 \\ y_2 \\ \vdots \\ y_{n-1} \\ y_n \end{bmatrix} \quad (59)$$

Equation (60) can be derived after conducting partial derivatives.

$$\begin{bmatrix} \theta_1 \\ \alpha_1 \\ \theta_2 \\ \alpha_2 \\ \vdots \\ \theta_{n-2} \\ \alpha_{n-2} \\ \theta_{n-1} \\ \alpha_{n-1} \end{bmatrix} = \begin{bmatrix} -\frac{x_2-x_1}{dz_1\sqrt{(x_2-x_1)^2+(y_2-y_1)^2}\left(\frac{(x_2-x_1)^2+(y_2-y_1)^2}{dz_1^2}+1\right)} & \frac{x_2-x_1}{dz_1\sqrt{(x_2-x_1)^2+(y_2-y_1)^2}\left(\frac{(x_2-x_1)^2+(y_2-y_1)^2}{dz_1^2}+1\right)} & 0 & 0 & \ldots \\ \frac{y_2-y_1}{\left(\frac{(y_2-y_1)^2}{(x_2-x_1)^2}+1\right)(x_2-x_1)^2} & -\frac{y_2-y_1}{\left(\frac{(y_2-y_1)^2}{(x_2-x_1)^2}+1\right)(x_2-x_1)^2} & 0 & 0 & \ldots \\ & & \ddots & & \\ \ldots & 0 & 0 & -\frac{y_n-y_{n-1}}{dz_{n-1}\sqrt{(x_n-x_{n-1})^2+(y_n-y_{n-1})^2}\left(\frac{(x_n-x_{n-1})^2+(y_n-y_{n-1})^2}{dz_{n-1}^2}+1\right)} & \frac{y_n-y_{n-1}}{dz_{n-1}\sqrt{(x_n-x_{n-1})^2+(y_n-y_{n-1})^2}\left(\frac{(x_n-x_{n-1})^2+(y_n-y_{n-1})^2}{dz_{n-1}^2}+1\right)} \\ \ldots & 0 & 0 & -\frac{1}{(x_n-x_{n-1})\left(\frac{(y_n-y_{n-1})^2}{(x_n-x_{n-1})^2}+1\right)} & \frac{1}{(x_n-x_{n-1})\left(\frac{(y_n-y_{n-1})^2}{(x_n-x_{n-1})^2}+1\right)} \end{bmatrix} \cdot \begin{bmatrix} x_1 \\ x_2 \\ \vdots \\ x_{n-1} \\ x_n \\ y_1 \\ y_2 \\ \vdots \\ y_{n-1} \\ y_n \end{bmatrix}$$

(60)

Case Study

Numerical Model

To validate the proposed EKF-based monitoring system, the floater-mooring-riser coupled time-domain simulation was performed. A FPSO (Floating Production Storage and Offloading) was selected as a floating structure. The principal dimensions of the vessel are presented in Table 8(Kim and Kim, 2015a). A 3D diffraction/radiation panel program (Lee et al., 1991) was used to estimate hydrodynamic coefficients and wave loads in the frequency domain. The panel model of the FPSO is shown in Figure 57. The total number of 2,448 panels was finally chosen after the convergence test.

Table 8 Principal Dimensions and Particulars of FPSO Model. Adapted from Kim and Kim (2015b).

Designation	Unit	Value
Vessel size	kDWT	200
Length between perpendicular	m	310
Breadth	m	47.17
Depth	m	28.04
Draft	m	18.90
Displacement	MT	240,869
Block coefficient	Dimensionless	0.85
Center of gravity above Base	m	13.30
Water plane area	m^2	13,400
Roll radius of gyration at CG	m	14.77
Pitch radius of gyration at CG	m	77.47
Yaw radius of gyration CG	m	79.30

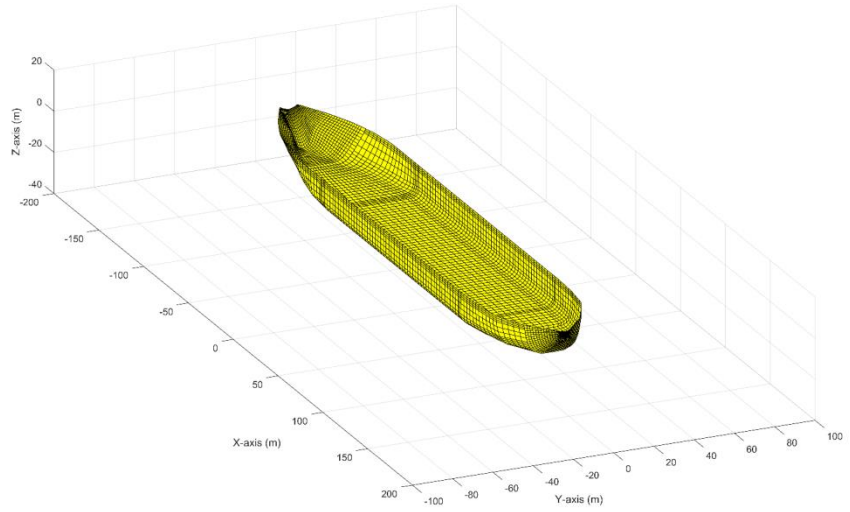

Figure 57 FPSO-Hull Panel Model.

After the frequency-domain calculation, time-domain simulations were performed with mooring lines and a Steel Catenary Risers (SCR). The Morison equation estimated the wave loading on the slender mooring lines and risers. Turret mooring system with eight mooring lines was considered, and the riser was also connected to the turret. Riser properties are given in Table 9. Commercial program OrcaFlex was used for the time-domain simulation of the coupled system. During the time-domain simulation, we placed multiple numerical inclinometers for providing the supposedly measured inclination and heading angle signals at the target points. To make it more realistic and practical, we added artificial white noise within the noise range provided by the sensor manufacturer. They were used as measurement data for the ensuing EKF algorithm. Figure 58 shows the designed numerical model in OrcaFlex.

Table 9 Steel Catenary Riser Parameters.

Parameters	Unit	Value
Outer diameter	mm	461
Wall thickness	mm	21
Coating thickness	mm	75
Young's modulus	GPa	207
Yield stress	MPa	448
Steel density	kg/m^3	7850
Coating density	kg/m^3	800

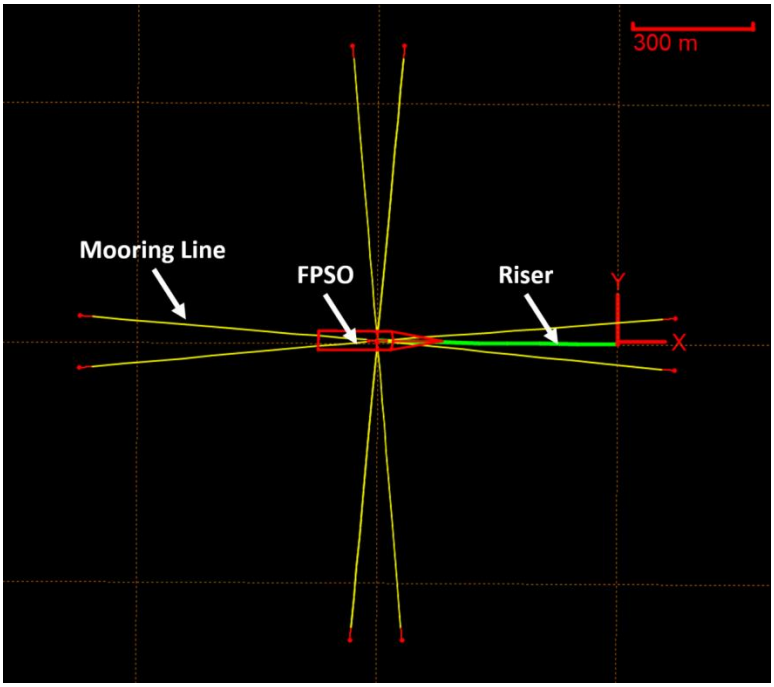

Figure 58 Designed Numerical Model for the Turret-Moored FPSO System with the Selected Riser.

Environmental conditions are summarized in Table 10. Gulf of Mexico's (GOM) 1-year and 100-year wave conditions were considered with corresponding current velocities. As presented in Table 11, four different environmental conditions were

considered. The JONSWAP wave spectrum was adopted with appropriate enhancement parameters, and 200 regular wave components were superposed to generate irregular waves. The simulation time for each case was 4000 sec. Water depth was fixed to be 700 m. Signal repetition was prevented by using the equal energy discretization method in which each wave component has an equal amount of spectral energy. For convenience, random waves and steady shear currents are considered, but wind is not included since it does not directly affect riser dynamics.

Table 10 Environmental Conditions in the Simulation.

Environment	Item	GOM 1-year wave	GOM 100-year wave
Wave	Significant wave height (H_S)	4.30 m	12.19 m
	Perk period (T_P)	9.0 sec	14.0 sec
	Enhancement parameter (γ)	2.0	2.5
Current	Velocity	0.33 m/s	1.07 m/s

Table 11 Simulated Cases Under Different Sea States and Directions.

Case No.	H_S (m)	T_P (sec)	Wave direction (deg)	Current (m/s)	Current direction (deg)
1 (GOM 1-year waves / Collinear)	4.30	9.0	180	0.33	180
2 (GOM 1-year waves / Non-collinear)	4.30	9.0	190	0.33	120
3 (GOM 100-year waves / Collinear)	12.19	14.0	180	1.07	180
4 (GOM 100-year waves / Non-collinear)	12.19	14.0	190	1.07	120

Measurement-Data Acquisition

Figure 59 shows the sensor arrangement along the riser, and the red boxes indicate the locations of inclinometers. As mentioned before, a SCR attached to the FPSO was tested to verify the developed EKF-based monitoring method. Along the riser, there are 10 inclinometers that can measure inclination and heading, and the distance between the sensors was assumed to be identical. Then, the position of the riser-top point and bi-axial angles at the sensor locations were produced by the time-domain simulation, and they were inputted to the EKF algorithm at each data-sampling time step. Figure 60 presents the obtained surge, sway, and heave motions of the FPSO from the time-domain simulation under the non-collinear environmental condition of Case #4. The generated time series show typical surge-sway-heave characteristics of FPSO in the given environment (Kim et al., 2005). The data sampling frequency was 5 Hz.

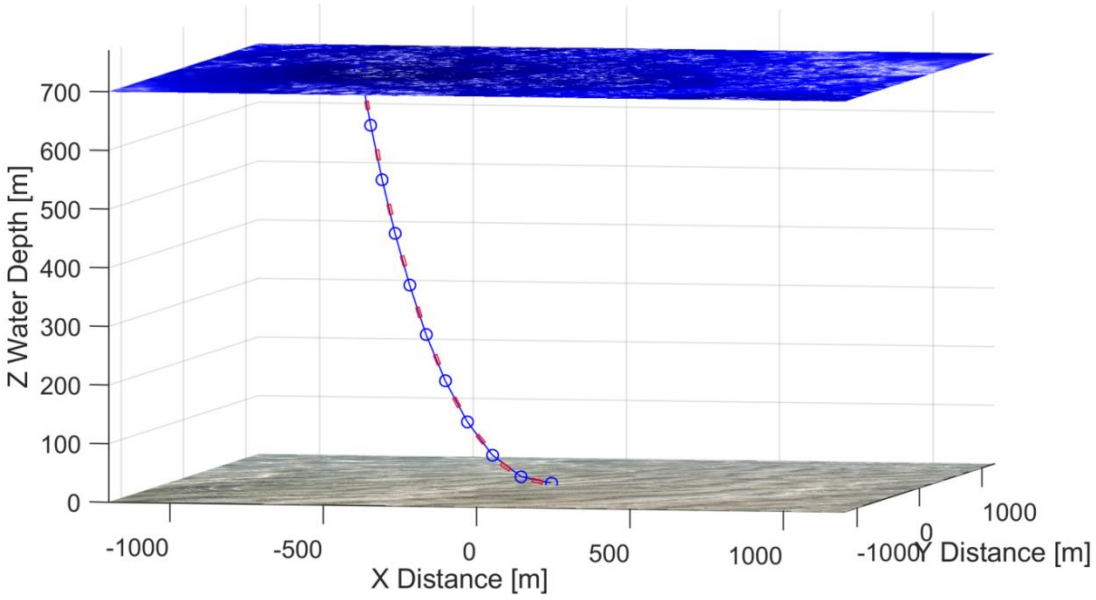

Figure 59 Initial Arrangement of Sensors Along the Riser.

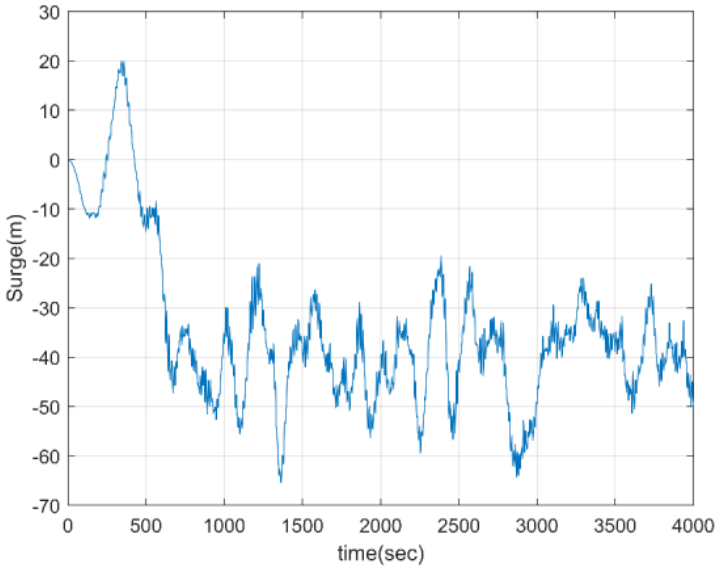

(a) Surge

Figure 60 FPSO Motions from Numerical Simulation.

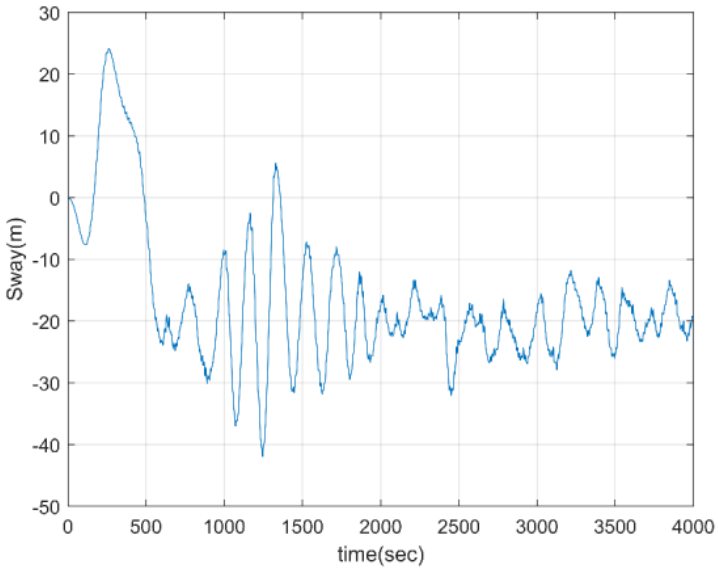

(b) Sway

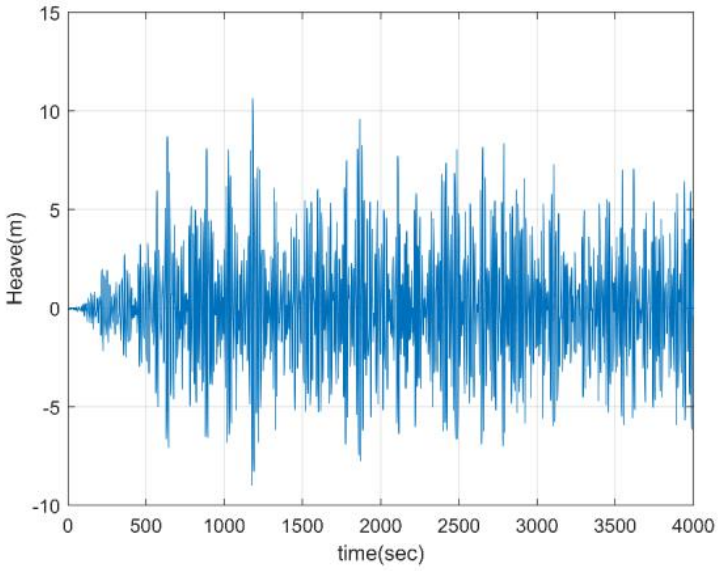

(C) Heave

Figure 60 Continued.

Figure 61 shows the time histories of the inclination and heading of the riser at all sensor locations under the environmental condition of Case #4. A white noise equivalent to the standard deviation of sensor error was artificially added, and thus high-frequency fluctuations can be observed in the signals. If the figure is zoomed in, the error (or sensor noise) is more visible as illustrated.

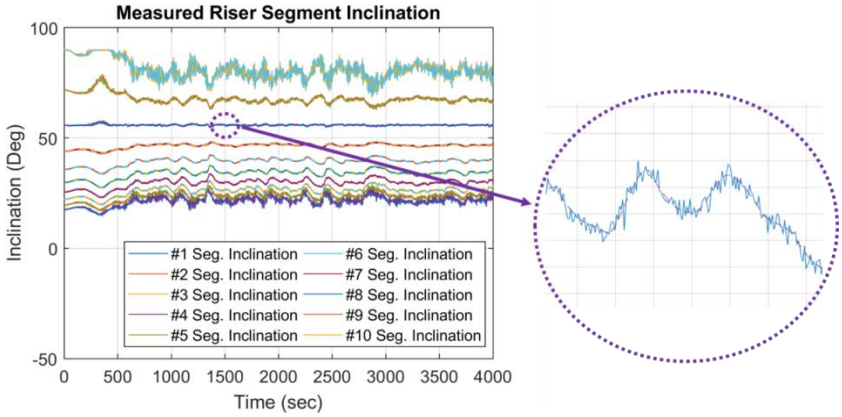

(a) Inclination signals from 10 numerical inclinometers with artificial noise

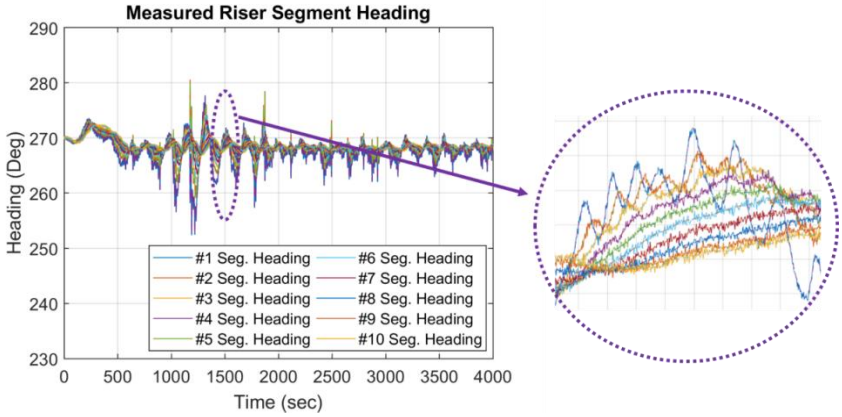

(b) Heading signals from 10 numerical inclinometers with artificial noise

Figure 61 Input Time-Histories of Angle Sensors for Case #4.

Results and Discussion

Riser Shape Estimation

The EKF-based monitoring system is validated by comparing the estimated shape of the riser with the numerical-sensor input data at each time step. Figure 62 shows the estimated deformed shape of the riser at 335 and 902 seconds under the environmental condition of Case #4. In the figure, the green dotted line denotes the initial riser shape and blue dashed and red solid lines represent actual and estimated deformed shapes, respectively. The line connecting the estimated nodes in real-time is the estimated deformed shape. The estimated deformed shape is well matched with the actual one. The results show that the proposed method is robust and feasible to monitor the global behavior of the riser in real time.

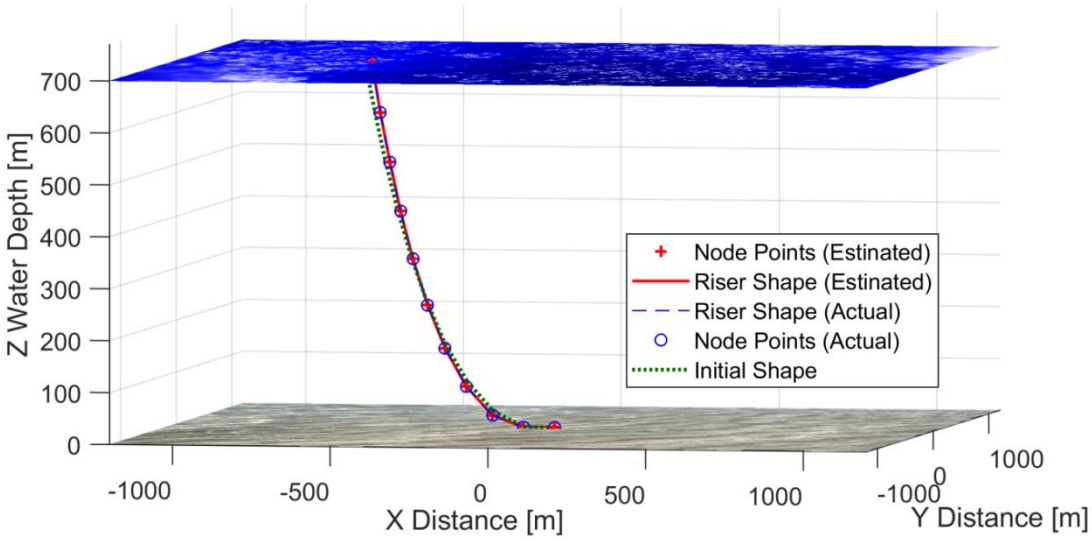

(a) 335 sec

Figure 62 Riser Shape Estimation for Case #4.

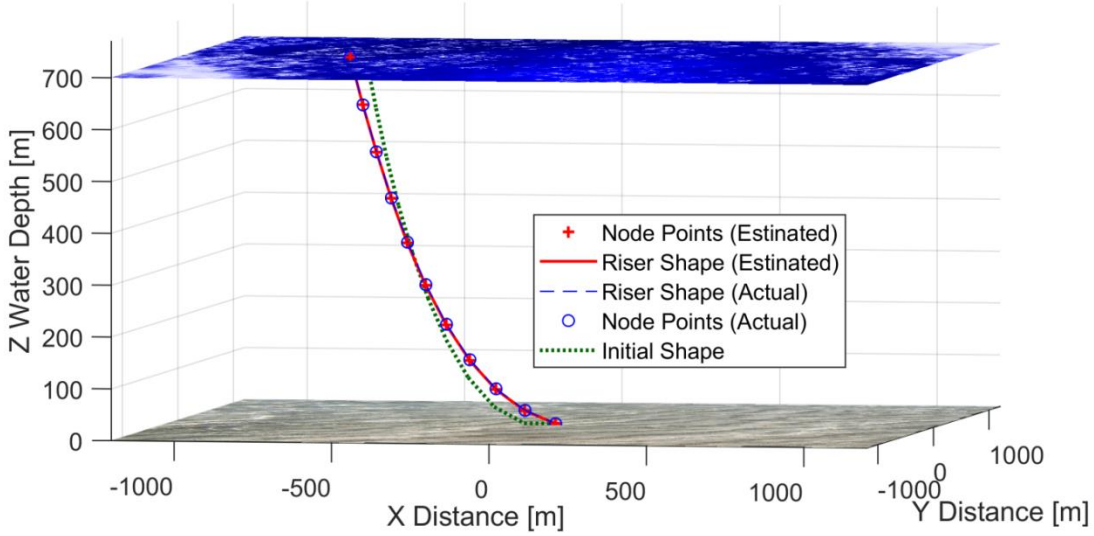

(b) 902 sec

Figure 62 Continued.

Figure 63 - Figure 66 show the time histories of the actual and estimated riser responses under four different environmental conditions of Case #1 - #4. Case #1 and #3 are for collinear wave-current condition and Case #2 and #4 are for noncollinear condition, as indicated in Table 11. The noncollinear cases were introduced to observe more pronounced heading angle movement of the riser to prove 3D extension. Nodes # 4, #6 and #8 are selected for comparison because those are far from the known two ends, Nodes #1 and #11. In all cases, the estimated riser displacements are in good agreement with the actual values. The proposed method can capture both slow-varying and wave-frequency responses of the riser. Both responses are caused by the corresponding FPSO surge motions in random waves. On the other hand, as well known, heave motions have only wave-frequency oscillations. It is much more difficult to recover this kind of

detailed riser response using the conventional accelerometer (Choi and Kim, 2018). Also, the accelerometer-based monitoring method can be problematic due to dual-time integration and sensor noises (Choi and Kim, 2018). However, by using the present method, high-frequency sensor errors do not cause any problem.

Other conventional methods for riser monitoring require additional analysis models in addition to sensor measurement data, but the present system only requires riser top and angle data. Using stress estimations calculated from the monitored riser geometry in real-time, it is expected that the real-time cumulative fatigue damage can also be calculated. This means that more accurate fatigue life predictions can be made based on actual riser-response records.

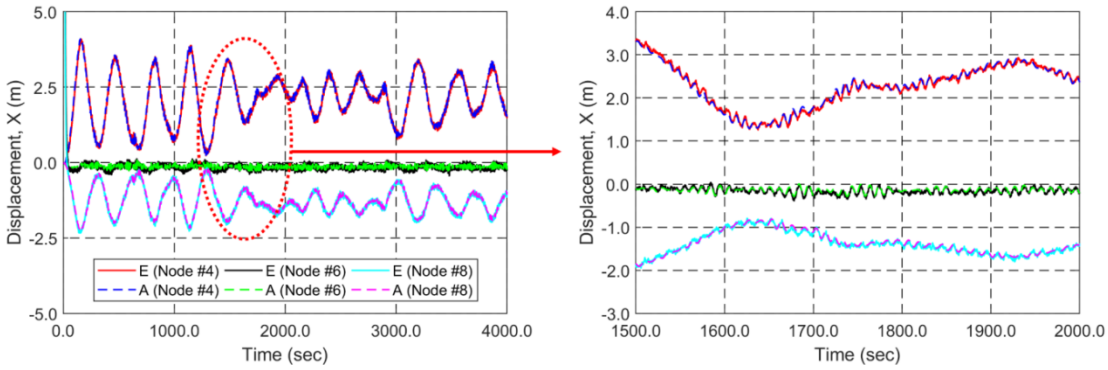

(a) Surge (x) direction

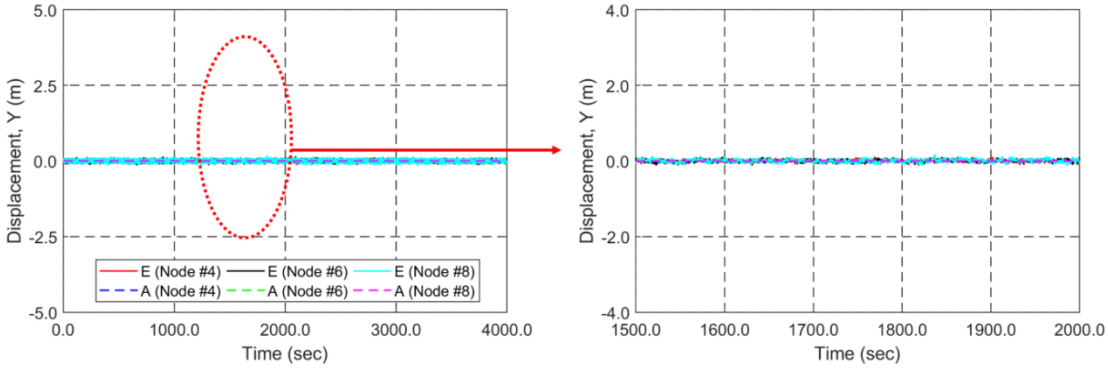

(b) Sway (y) direction

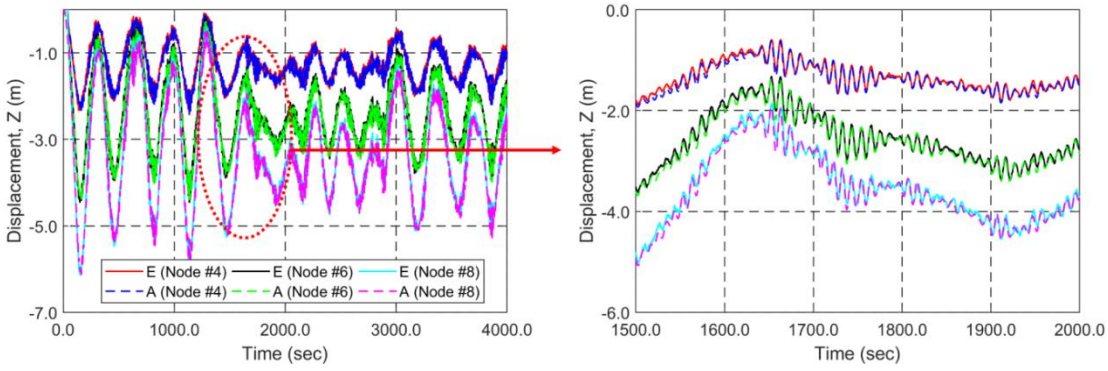

(c) Heave (z) direction

Figure 63 Estimated Displacements of Nodes for Case #1 (E: Estimated Displacements, A: Actual Displacement).

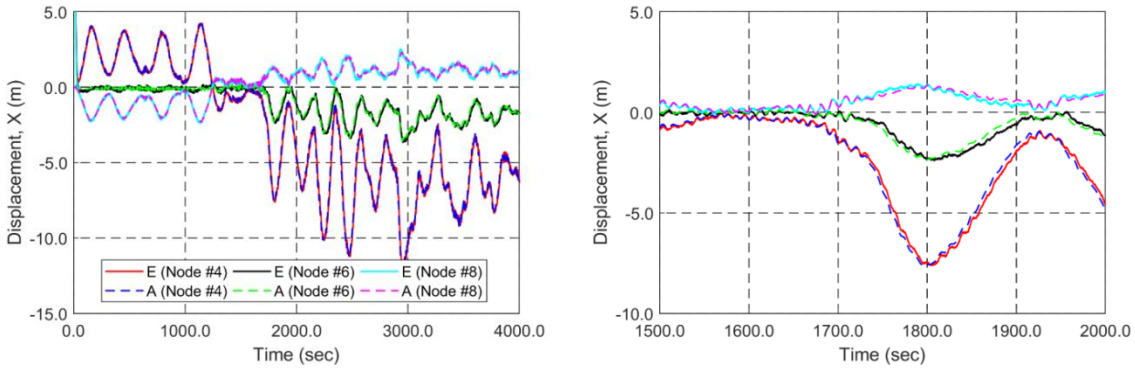

(a) Surge direction

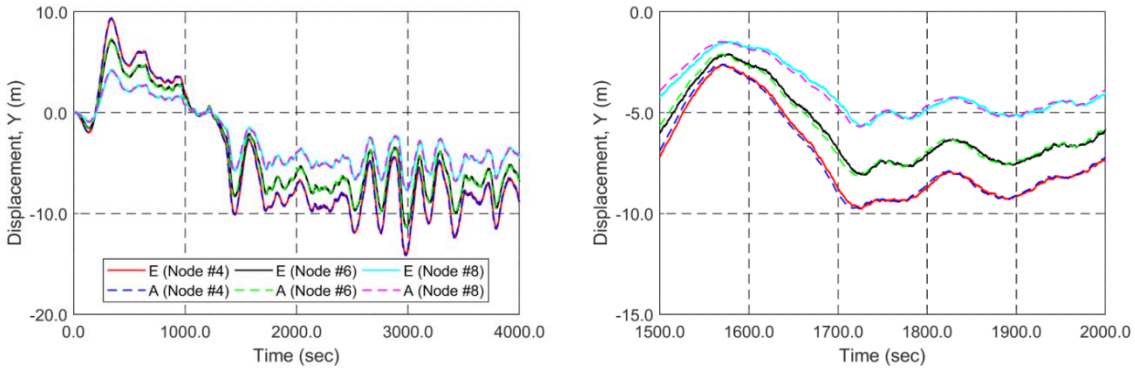

(b) Sway direction

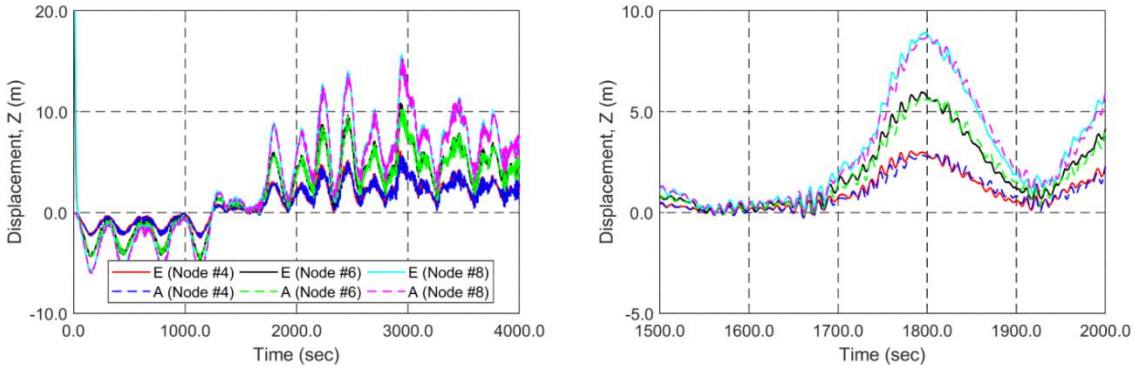

(c) Heave direction

Figure 64 Estimated Displacements of Nodes for Case #2.

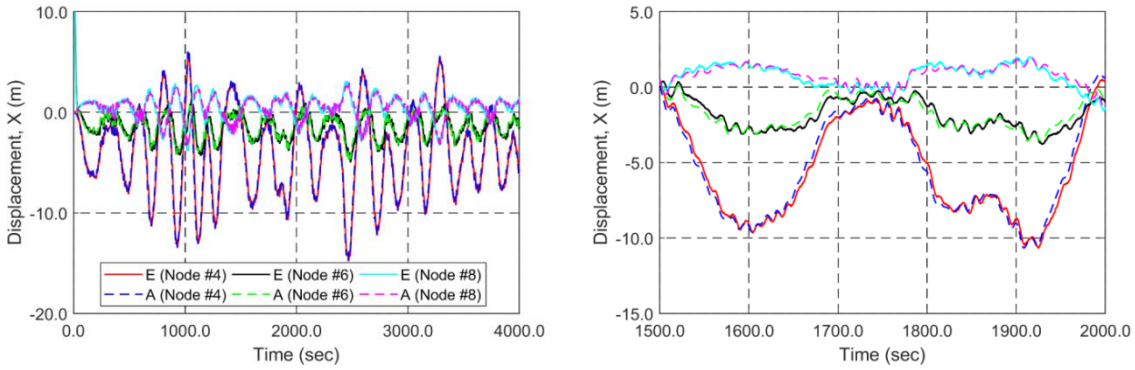

(a) Surge direction

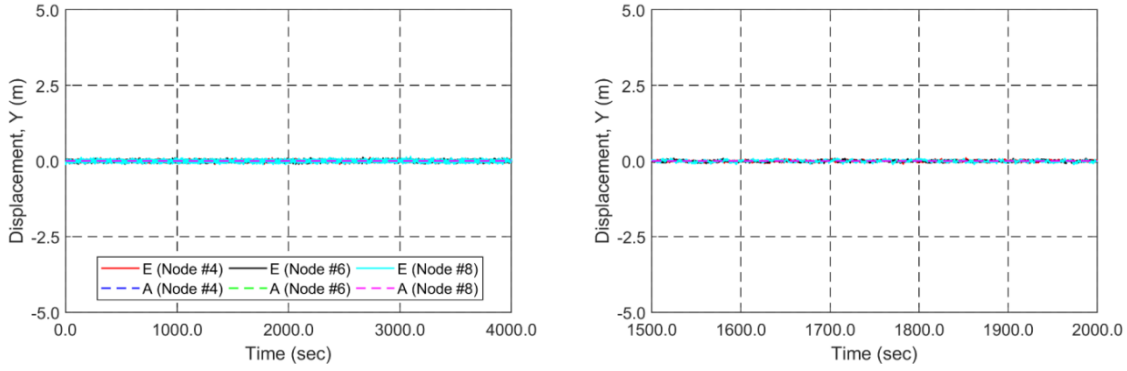

(b) Sway direction

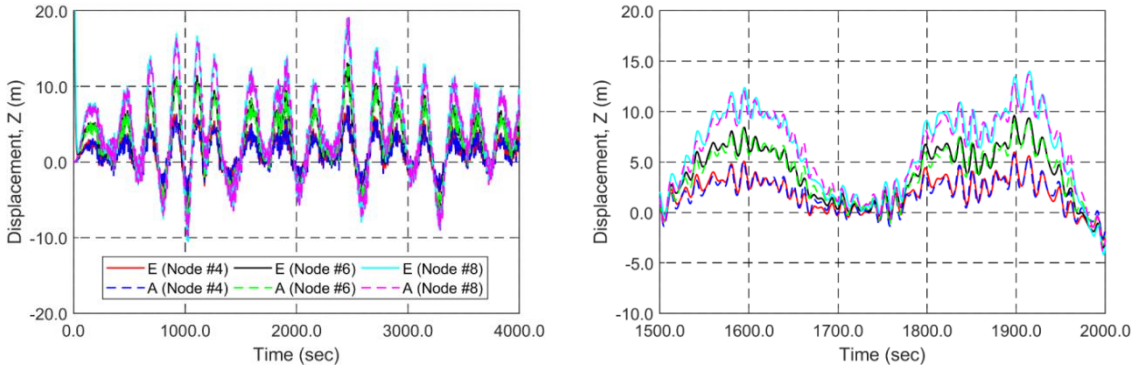

(c) Heave direction

Figure 65 Estimated Displacements of Nodes for Case #3.

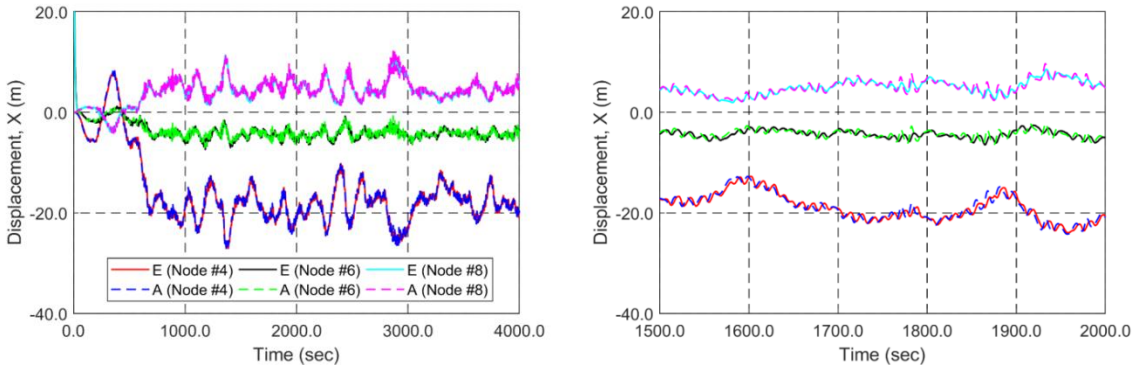

(a) Surge direction

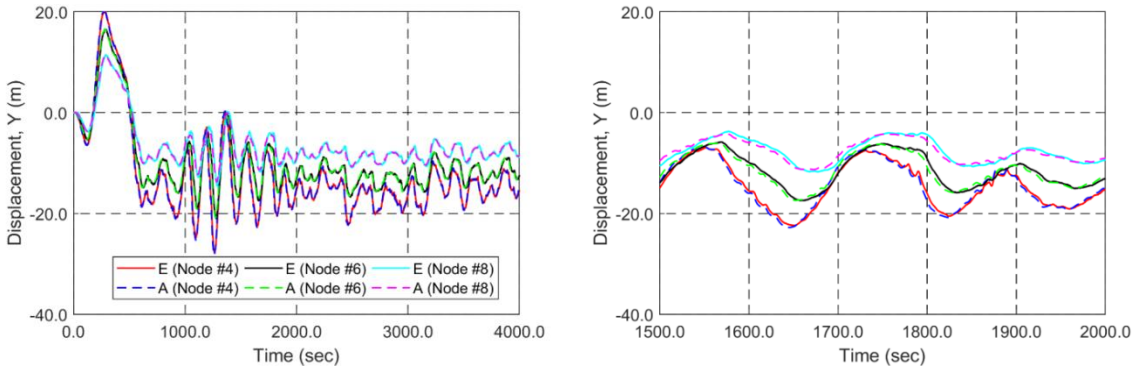

(b) Sway direction

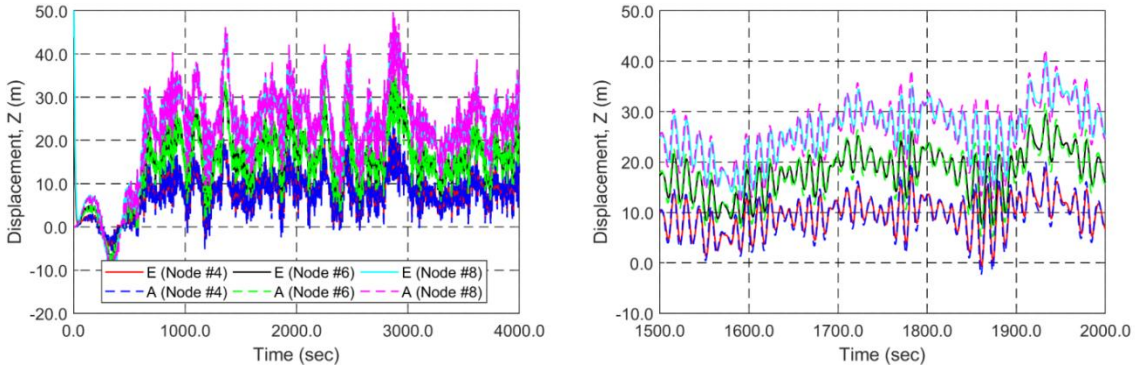

(c) Heave direction

Figure 66 Estimated Displacements of Nodes for Case #4.

Real-Time Stress Evaluation

Real-time internal stress estimation of the riser is important in view of structural safety, accumulated fatigue-damage prediction, and life extension. Axial and bending stresses are estimated after the riser's deformed shape at each time step is obtained. Either forces/moments at each element or angles/curvatures in 3D should be known to estimate these stresses. The former is almost impossible since it is challenging to measure forces and moments underwater. However, the latter is possible by calculating angles and curvatures from the monitored profile through spatial derivatives. Direct use of inclination and heading signals from sensors can have limitations since they have high-frequency sensor errors. Signal processing can remove the sensor error; however, it can cause the phase change and distortion of time-history signals. Note that stress estimation is based on a single global coordinate system with the generalized coordinate system (see Figure 67), which always has the longitudinal axis parallel to the riser's direction. The effective tension and bending moments for the riser can be calculated as (Ran et al., 1999):

$$\begin{aligned} T_e &= T_w + \left(P_o A_o - P_i A_i\right) \\ T_w &= \frac{E(A_o - A_i)}{L}\Delta L - 2\nu\left(P_o A_o - P_i A_i\right) \\ M_{opb} &= EIr_Z'' \\ M_{ipb} &= EIr_Y'' \end{aligned} \tag{61}$$

where T_e and T_w are the effective and wall tensions, P and A are pressure and cross-sectional area, L is an element length, ΔL means an extension of the element, ν is Poisson's ratio, M is bending moment, E is Young's modulus, I is the area moment of inertia, and $r''\left(=r_X''\,\vec{\mathrm{i}}+r_Y''\,\vec{\mathrm{j}}+r_Z''\,\vec{\mathrm{k}}\right)$ is the principal normal vector, which can be obtained by the spatial derivative of position vector r twice. Subscripts, o, i, opb, and ipb denote outer, inner, direction for out of plane bending, and in-plane bending, respectively.

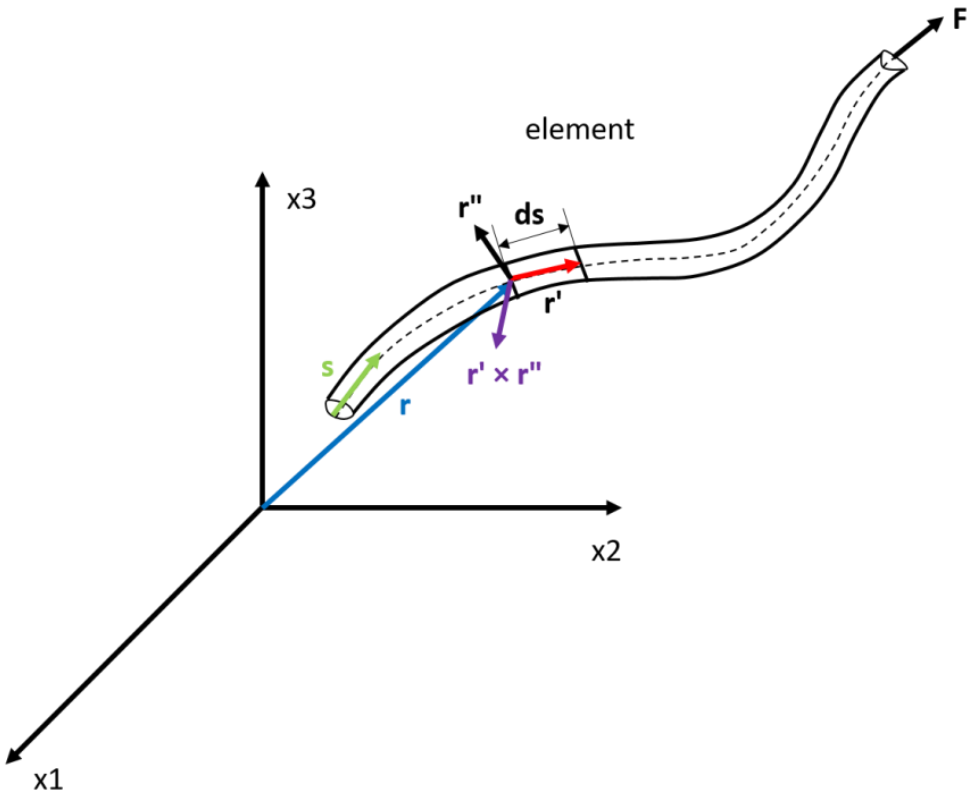

Figure 67 Coordinate System for Stress Estimation. Adapted from Jin and Kim (2020).

According to Equation (61), the tension estimation requires an actual extension of a riser pipe. Since small extension can change the tension significantly, the direct calculation from strain variation is infeasible. Therefore, another equation is introduced to calculate the riser effective tension as follows:

$$T_{e,i+1} = T_{e,i} + \left(W_{water,i} - W_{riser,i} - W_{fluid,i}\right)\left|\gamma_i\right|$$
$$\gamma_i = \frac{r_{z,i}}{\sqrt{r_{x,i}^2 + r_{y,i}^2 + r_{z,i}^2}} \tag{62}$$

where i is an element number, W_{water}, W_{riser}, and W_{fluid} are weights of water, riser, and fluid, γ is a directional cosine in the z-direction. i starts from the element close to the fairlead location. According to Equation (62), as the effective tension at the fairlead position is measured, the effective tension at each element can be successively calculated.

As presented in Equation (61), out of plane and in-plane bending moments are a function of the corresponding principal normal vector, which is correlated to the curvature. After solving tensions and bending moments, the governing cyclic nominal stress component can be obtained as follows:

$$\sigma_{total}(t) = \sigma_T(t) + \sigma_{BM}(\theta, t)$$
$$\sigma_T(t) = \frac{T_e(t)}{\pi(D - t_a)t_a} \tag{63}$$
$$\sigma_{BM}(\theta, t) = \left(M_{opb}(t)\cos(\theta) + M_{ipb}(t)\sin(\theta)\right)\left(\frac{D - t_a}{2I}\right)$$

where $\sigma_T(t)$ and $\sigma_{BM}(t)$ are axial and bending stresses, $t_a = t_p - 0.5t_{corr}$ with pipe wall thickness t_p and the corrosion allowance t_{corr}, and D is the outer diameter. Corrosion allowance is not considered in the current estimation.

Figure 68 - Figure 75 show time-history comparisons of riser's effective tension as well as out of plane and in-plane bending moments at an arc length of 550 m for the Case #1 - #4. It is shown that the estimated tension and moments agree well with the actual values. The proposed tension-estimation method works well under the condition that the top tension is measured by tension-gage. Also, based on the estimated shape, the predicted bending moments in two directions compare well with the actual input values after the initial adjusting stage of Kalman filter.

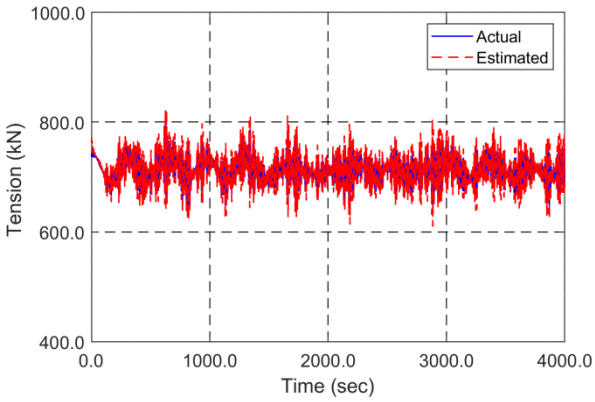

Figure 68 Riser's Effective Tension at the Arc Length of 550 m for Case #1.

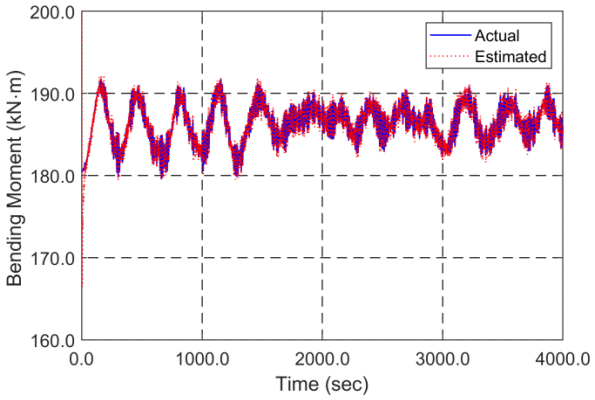

(a)

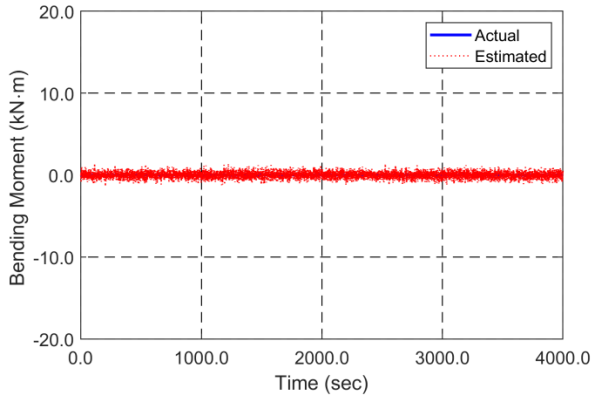

(b)

Figure 69 Out-Of-Plane (a) and In-Plane (b) Bending Moments at the Arc Length of 550 m for Case #1.

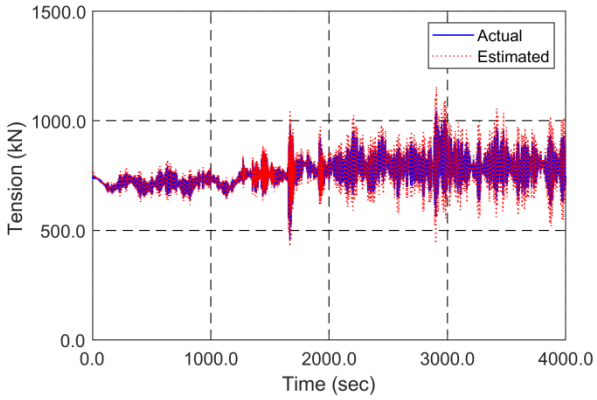

Figure 70 Riser's Effective Tension at the Arc Length of 550 m for Case #2.

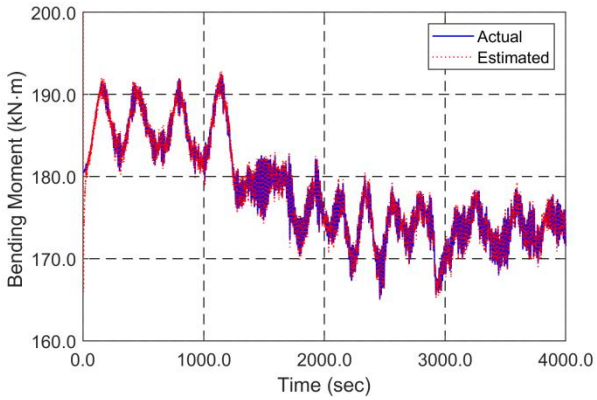

(a)

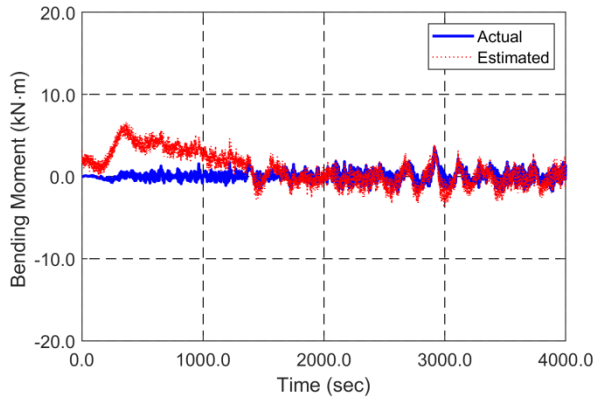

(b)

Figure 71 Out-Of-Plane (a) and In-Plane (b) Bending Moments at the Arc Length of 550 m for Case #2.

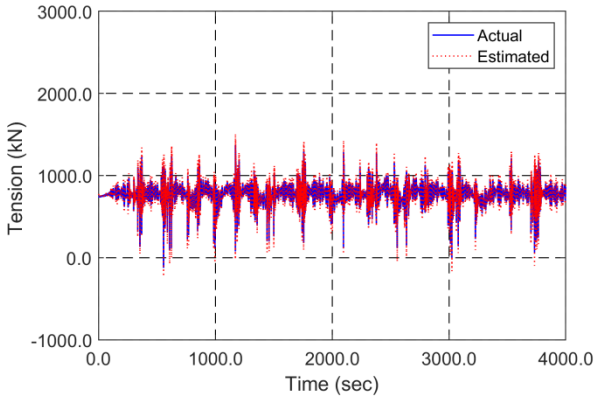

Figure 72 Riser's Effective Tension at the Arc Length of 550 m for Case #3.

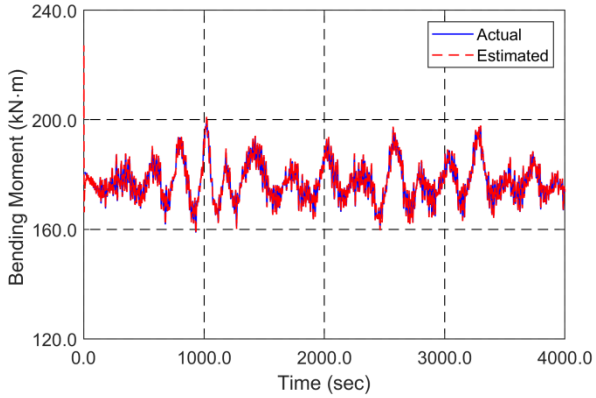

(a)

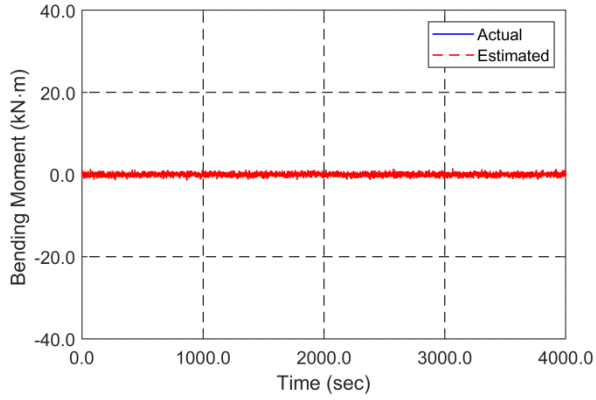

(b)

Figure 73 Out-Of-Plane (a) and In-Plane (b) Bending Moments at the Arc Length of 550 m for Case #3.

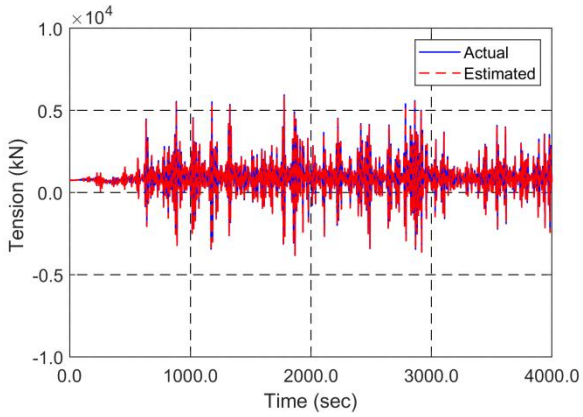

Figure 74 Riser's Effective Tension at the Arc Length of 550 m for Case #4.

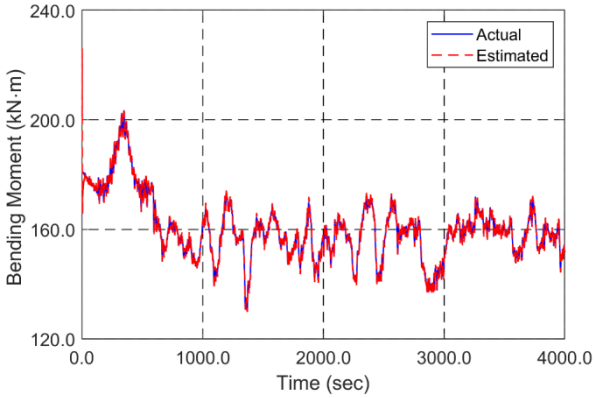

(a)

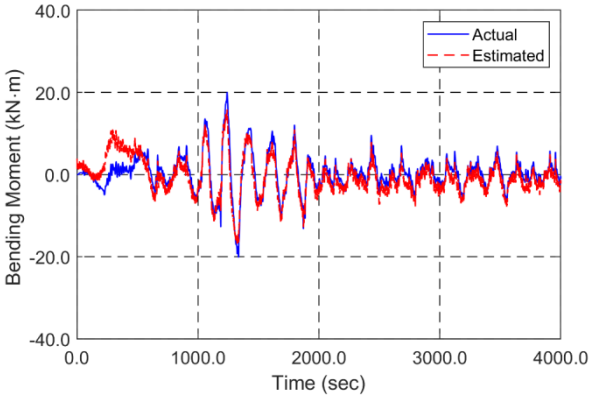

(b)

Figure 75 Out-Of-Plane (a) and In-Plane (b) Bending Moments at the Arc Length of 550 m for Case #4.

Figure 76 - Figure 79 show the combined nominal stress at an arc length of 550 m, and θ is set as 0° where the maximum normal stress occurs. The predicted stress matches well with the actual value from the time-domain simulation. The capability also proves that the stress monitoring from the riser's deformed shape in real time is feasible. Furthermore, the capability of real-time stress estimation near hotspots also allows the real-time estimation of the accumulated fatigue damage (Kim and Kim, 2015a; Kim and Kim, 2018) so that it can be used for the assessment of life extension.

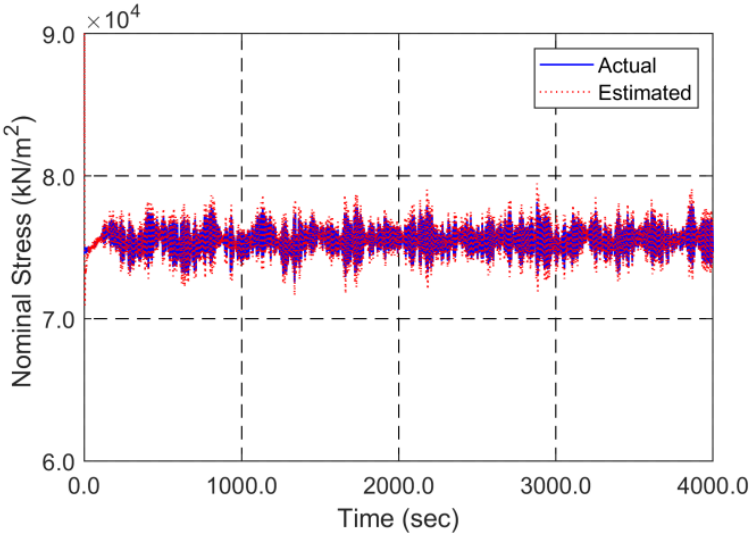

Figure 76 Maximum Nominal Stress at the Arc Length of 550 m for Case #1.

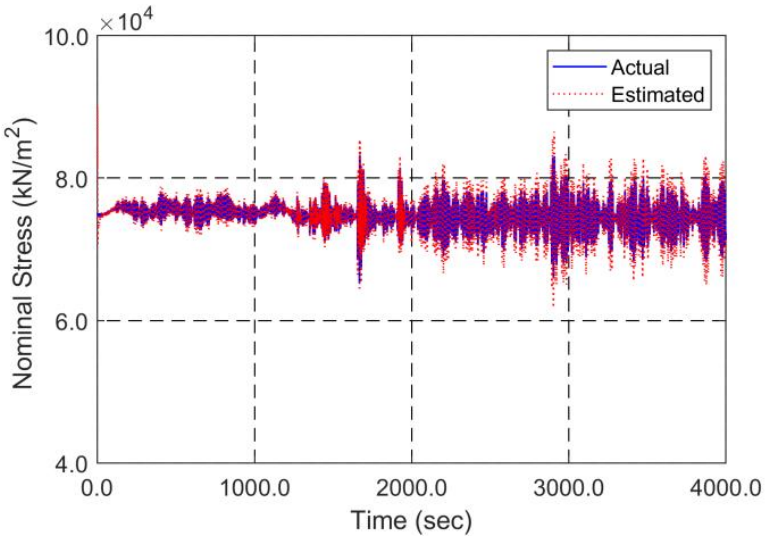

Figure 77 Maximum Nominal Stress at the Arc Length of 550 m for Case #2.

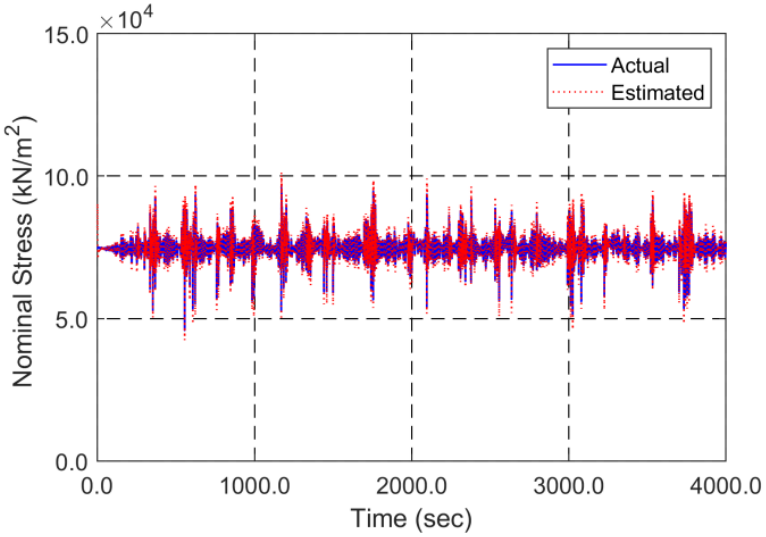

Figure 78 Maximum Nominal Stress at the Arc Length of 550 m for Case #3.

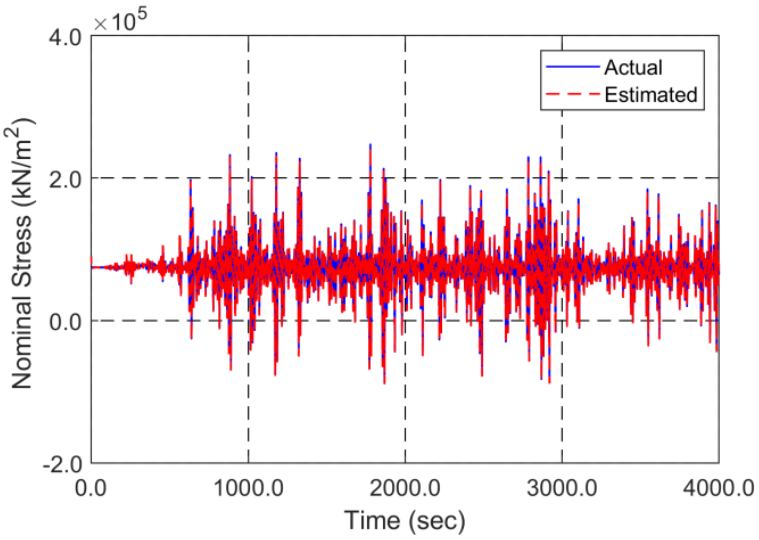

Figure 79 Maximum Nominal Stress at the Arc Length of 550 m for Case #4.

CHAPTER IV

CONCLUSIONS

Conclusions for Chapter II

Despite the inherent advantages of the Kalman filter, it has rarely been used for the inverse estimation of incident waves from motion sensors in the open literature. In the present paper, both real-time wave spectrum and elevation were obtained through the adaptive Kalman-filter algorithms.

A problem of amplified noise occurs in the zone associated with the Kalman filter when vessel's motion RAO is small in the high frequency region and there is sensor error. A new solution to the problem is presented, so that the small gain in the RAO increases by a certain amount by using the Winer filter. If the proposed modified TF is applied, the overestimation of real-time wave spectra in the high-frequency region can be suppressed. The real-time incident wave profile can also be inversely estimated.

The vessel's motion transfer functions and numerically generated motion-sensor signals were used to the present Kalman-filter processes. The Kalman filter has been tested for various sea states and different vessel types while using the modified TF through Wiener filter. The test results were promising. In addition, the proposed Kalman filter performed well estimation even in the case of more realistic conditions, which multi-directional wave and ship's speed inclusion.

For further research, the full-scale test with a real vessel in the real sea needs to assess the developed Kalman-filter algorithms.

Conclusions for Chapter III

In this study, a new real-time riser monitoring method based on the Extended Kalman Filter (EKF) was proposed. It estimated the overall shape of riser in real-time using the measured signals from multiple bi-axial (inclination and heading) inclinometers along the riser. Another data needed was the positions of two end points. Then, a novel Extended Kalman Filter (EKF) algorithm was developed to real-time estimate the instantaneous riser profile by using the sensor signals. The relationship between the riser position and measured angles for each segment was nonlinear, so equivalent-linearization was done by using Jacobian matrix. Then, the combined matrix for the whole elements was simultaneously processed through the developed EKF algorithm. As a result, the riser's deformed shape induced by environmental loadings and platform motions can be monitored in real-time. Subsequent algorithms were also developed so that the corresponding bending and axial stresses along the riser could also be estimated from the obtained riser shape, which can further result in the real-time estimation of fatigue-damage accumulation.

REFERENCES

Al-Habashneh, A.-A., Moloney, C., Gill, E.W., Huang, W., 2018. The effect of radar ocean surface sampling on wave spectrum estimation using X-band marine radar. IEEE Access 6, 17570-17585.

Bishop, G., Welch, G., 2001. An introduction to the Kalman filter. Proc of SIGGRAPH, Course 8 (27599-23175).

Bitner-Gregersen, E.M., Eide, L.I., Hørte, T., Skjong, R., 2013. Ship and offshore structure design in climate change perspective. Springer.

Brown, R.G., Hwang, P.Y., 1992. Introduction to random signals and applied Kalman filtering. Wiley New York.

Choi, J., Kim, J.M.-H., 2018. Development of a new methodology for riser deformed shape prediction/monitoring, ASME 2018 37th International Conference on Ocean, Offshore and Arctic Engineering. American Society of Mechanical Engineers Digital Collection.

Cook, H., Dopjera, D., Thethi, R., Williams, L., 2006. Riser integrity management for deepwater developments, Offshore Technology Conference. Offshore Technology Conference.

DNV, 2000. Environmental conditions and environmental loads, Classification Notes No. 30.5. Det Norske Veritas AS.

Ge, M.L., Kannala, J., Li, S., Maheshwari, H., Campbell, M., 2014. A new riser fatigue monitoring methodology based on measured accelerations, ASME 2014 33rd

International Conference on Ocean, Offshore and Arctic Engineering. American Society of Mechanical Engineers Digital Collection.

Gorman, R.M., 2018. Estimation of directional spectra from wave buoys for model validation. Procedia Iutam 26, 81-91.

Holzhuter, T., 1997. LQG approach for the high-precision track control of ships. IEE Proceedings-Control Theory and Applications 144 (2), 121-127.

International Maritime Organization, 2019. E-navigation, http://www.imo.org/en/ourwork/safety/navigation/pages/enavigation.aspx.

Jackson, F.C., Walton, W.T., Baker, P.L., 1985. Aircraft and satellite measurement of ocean wave directional spectra using scanning- beam microwave radars. Journal of Geophysical Research: Oceans 90 (C1), 987-1004.

Jin, C., Kim, M.-H., 2018. Time-domain hydro-elastic analysis of a SFT (submerged floating tunnel) with mooring lines under extreme wave and seismic excitations. Applied Sciences 8 (12), 2386.

Jin, C., Kim, M.-H., 2020. Tunnel-mooring-train coupled dynamic analysis for submerged floating tunnel under wave excitations. Applied Ocean Research 94, 102008.

Jokioinen, E., 2015. Roadmap for remote controlled ships, MUNIN workshop, http://www.unmanned-ship.org/munin/wp-content/uploads/2015/06/MUNIN-Workshop-1-1-RR-Rolls-Royce%E2%80%99s-roadmap-for-autonomous-ships.pdf

Karayaka, M., 2009. Tahiti online monitoring system for steel catenary risers and flowlines, Offshore Technology Conference, Houston, TX.

Karayaka, M., Ruf, W., Natarajan, S., 2009. Steel catenary riser response characterization with on-line monitoring devices, ASME 2009 28th International Conference on Ocean, Offshore and Arctic Engineering. American Society of Mechanical Engineers Digital Collection, pp. 687-698.

Keprate, A., Ratnayake, R., 2015. Fatigue and fracture degradation inspection of offshore structures and mechanical items: the state of the art, ASME 2015 34th International Conference on Ocean, Offshore and Arctic Engineering. American Society of Mechanical Engineers Digital Collection.

Kim, H., Kang, H., Kim, M.-H., 2019. Real-time inverse estimation of ocean wave spectra from vessel-motion sensors using adaptive Kalman filter. Applied Sciences 9 (14), 2797.

Kim, H., Kim, M., 2015a. Global performances of a semi-submersible 5 MW wind-turbine including second-order wave-diffraction effects. Ocean Syst. Eng 5 (3), 139-160.

Kim, H., Kim, M., 2016. Comparison of simulated platform dynamics in steady/dynamic winds and irregular waves for OC4 semi-submersible 5MW wind-turbine against DeepCwind model-test results. Ocean Syst. Eng 6 (1), 1-21.

Kim, M., Koo, B., Mercier, R., Ward, E., 2005. Vessel/mooring/riser coupled dynamic analysis of a turret-moored FPSO compared with OTRC experiment. Ocean Engineering 32 (14-15), 1780-1802.

Kim, S., Kim, M.-H., 2015b. Dynamic behaviors of conventional SCR and lazy-wave SCR for FPSOs in deepwater. Ocean Engineering 106, 396-414.

Kim, S., Kim, M.-H., 2018. Effects of geometric shape of LWSCR (lazy-wave steel catenary riser) on its global performance and structural behavior. Ocean Systems Engineering 8 (3), 247-279.

Ladetto, Q., 2000. On foot navigation: continuous step calibration using both complementary recursive prediction and adaptive Kalman filtering, Proceedings of ION GPS, pp. 1735-1740.

Lagendijk, R.L., Biemond, J., 2009. Basic methods for image restoration and identification, The essential guide to image processing. Elsevier, pp. 323-348.

Lee, C.H., Newman, J.N., Kim, M.H., Yue, D.K.P., 1991. The computation of second-order wave loads, Proceeding of OMAE Conference. American Society of Mechanical Engineers, Stavanger, Norway.

Liu, S., 1998. An adaptive Kalman filter for dynamic estimation of harmonic signals, 8th International Conference on Harmonics and Quality of Power. Proceedings (Cat. No. 98EX227). IEEE, pp. 636-640.

McAndrew, A., 2015. A computational introduction to digital image processing. Chapman and Hall/CRC.

Mercan, B., Chandra, Y., Maheshwari, H., Campbell, M., 2016. Comparison of riser fatigue methodologies based on measured motion data, Offshore Technology Conference. Offshore Technology Conference.

Minter, A., 2017. Autonomous ships will be great. Bloomberg, https://www.bloomberg.com/opinion/articles/2017-05-16/autonomous-ships-will-be-great.

Nielsen, U.D., Stredulinsky, D.C., 2011. Onboard sea state estimation based on measured ship motions, International Ship Stability Workshop.

Orcina Ltd, 2018. OrcaFlex user manual: OrcaFlex version 10.2 c, Daltongate, Ulverston, Cumbria, UK.

Pascoal, R., Perera, L.P., Soares, C.G., 2017. Estimation of directional sea spectra from ship motions in sea trials. Ocean Engineering 132, 126-137.

Pascoal, R., Soares, C.G., 2008. Non-parametric wave spectral estimation using vessel motions. Applied Ocean Research 30 (1), 46-53.

Pascoal, R., Soares, C.G., 2009. Kalman filtering of vessel motions for ocean wave directional spectrum estimation. Ocean Engineering 36 (6-7), 477-488.

Pascoal, R., Soares, C.G., Sørensen, A., 2007. Ocean wave spectral estimation using vessel wave frequency motions. Journal of Offshore Mechanics and Arctic Engineering 129 (2), 90-96.

Peng, R., Zhi, Z., 2012. A state-of-the-art review on structural health monitoring of deepwater floating platform. Pacific Science Review A: Natural Science and Engineering 14 (3), 253-263.

Podskarbi, M., Walters, D., 2006. Review and evaluation of riser integrity monitoring systems and data processing methods, Deep Offshore Technology Conference.

Podskarbi, M., Walters, D., Hatton, S., Karayaka, M., 2007. Design consideration of monitoring systems for deepwater steel catenary risers (SCRs), The Seventeenth International Offshore and Polar Engineering Conference. International Society of Offshore and Polar Engineers.

Ran, Z., Kim, M., Zheng, W., 1999. Coupled dynamic analysis of a moored spar in random waves and currents (time-domain versus frequency-domain analysis).

Reid, R.E., Parent, P.F., 1982. Comparison of optimal linear regulators applied to minimization of steering losses of a containership in a seaway using frequency domain representations. Journal of Dynamic Systems, Measurement, and Control 104 (3), 229-237.

Rhudy, M.B., Salguero, R.A., Holappa, K., 2017. A Kalman filtering tutorial for undergraduate students. International Journal of Computer Science and Engineering Survey 8 (1).

Safran, 2020. Bluenaute, https://www.safran-electronics-defense.com/file/download/bluenaute.pdf.

SBG Systems, 2018. Ekinox test results. SBG Systems, https://www.sbg-systems.com/wp-content/uploads/2018/07/Ekinox_Test_Marine.pdf.

Simon, D., 2006. Using nonlinear Kalman filtering to estimate signals. Embedded Systems Design 19 (7), 38.

Statistica, 2018. Number of ships in the world merchant fleet between January 1, 2008 and January 1, 2017, by type, https://www.statista.com/statistics/264024/number-of-merchant-ships-worldwide-by-type/

Sundararajan, D., 2017. Digital image processing: a signal processing and algorithmic approach. Springer.

Svašek Hydraulics, 2018. NOAA forecast animations. Svašek Hydraulics, http://www.worldwavedata.com/animations.html.

Thethi, R., Howells, H., Natarajan, S., Bridge, C., 2005. A fatigue monitoring strategy and implementation on a deepwater top tensioned riser, Offshore Technology Conference. Offshore Technology Conference.

Vectory Sensor Systems, 2020. Microrad rugged tilt sensor, https://www.vectory.com/products/subsea-tilt-sensors-inclinometers/microrad/.

Wikipedia, 2019. Wiener filter. Wikipedia, https://en.wikipedia.org/wiki/Wiener_filter.